NASA CR-54554
PWA FR-2112

SINGLE STAGE EXPERIMENTAL EVALUATION OF VARIABLE GEOMETRY GUIDE VANES AND STATORS

PART I - ANALYSIS AND DESIGN

BY

B. A. JONES AND D. L. WRIGHT

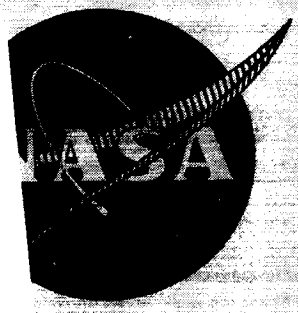

PREPARED FOR

NATIONAL AERONAUTICS AND SPACE ADMINISTRATION

CONTRACT NAS3-7604

Pratt & Whitney Aircraft DIVISION OF UNITED AIRCRAFT CORPORATION
FLORIDA RESEARCH AND DEVELOPMENT CENTER

NOTICE

This report was prepared as an account of Government sponsored work. Neither the United States, nor the National Aeronautics and Space Administration (NASA), nor any person acting on behalf of NASA:

A.) Makes any warranty or representation, expressed or implied, with respect to the accuracy, completeness, or usefulness of the information contained in this report, or that the use of any information, apparatus, method, or process disclosed in this report may not infringe privately owned rights; or

B.) Assumes any liabilities with respect to the use of, or for damages resulting from the use of any information, apparatus, method or process disclosed in this report.

As used above, "person acting on behalf of NASA" includes any employee or contractor of NASA, or employee of such contractor, to the extent that such employee or contractor of NASA, or employee of such contractor prepares, disseminates, or provides access to, any information pursuant to his employment or contract with NASA, or his employment with such contractor.

Requests for copies of this report should be referred to

National Aeronautics and Space Administration
Office of Scientific and Technical Information
Attention: AFSS-A
Washington, D.C. 20546

NASA CR-54554
PWA FR-2112

SINGLE STAGE EXPERIMENTAL EVALUATION OF VARIABLE GEOMETRY GUIDE VANES AND STATORS

PART I - ANALYSIS AND DESIGN

BY

B. A. JONES AND D. L. WRIGHT

PREPARED FOR

NATIONAL AERONAUTICS AND SPACE ADMINISTRATION

CONTRACT NAS3-7604

2 AUGUST 1968

TECHNICAL MANAGEMENT
NASA LEWIS RESEARCH CENTER
CLEVELAND, OHIO

NASA PROGRAM MANAGER: James J. Watt
Air Breathing Engines Division

NASA RESEARCH ADVISOR: L. Joseph Herrig
Fluid Systems Components Division

Pratt & Whitney Aircraft
DIVISION OF UNITED AIRCRAFT CORPORATION
FLORIDA RESEARCH AND DEVELOPMENT CENTER

ABSTRACT

An analysis was made to investigate variable geometry concepts for guide vanes and stators that can increase the stable operating range of low hub/tip ratio compressor stages. A variable geometry inlet guide vane, a rotor, and two variable geometry stator configurations were designed for test in a 0.5 hub/tip ratio single-stage compressor rig. Vector diagrams and the required blading geometries were defined for design point, axial-inlet operating conditions, and for off-design operation at 70% of design equivalent rotor speed. Compressor inlet screens to provide radial and circumferential distortion were also designed.

CONTENTS

CONTENTS (Continued)

SUMMARY

An analysis was made to investigate variable geometry concepts for guide vanes and stators that can increase the stable operating range of low hub/tip ratio compressor stages. A research stage with a variable geometry guide vane and two different variable geometry stator vane rows was designed for test in a 0.5 hub/tip ratio single-stage compressor.

Compressor stage types, characterized by mean radius rotor prewhirl, were studied to permit selection of a stage that would be best suited for variable geometry applications. A zero-prewhirl stage was selected because less rotor prewhirl change was required to meet the vector diagram requirements at off-design (high Mach number cruise) operating conditions. Design point vector diagrams were calculated for the selected stage. The design rotor tip velocity was approximately 1140 fps and the stage pressure ratio was 1.32. Vector diagrams were subsequently calculated for off-design operation, which was defined in the analysis at 70% of design equivalent rotor speed and 54% of design equivalent flow.

Variable geometry features that could provide the desired vector diagram adjustments were evaluated conceptually. A variable camber guide vane, derived from 63 series airfoil sections, was designed to provide zero-degree rotor prewhirl for design point operation and 35- to 20-degree (hub/tip) rotor prewhirl for the off-design conditions. The rotor, comprised of circular arc airfoil sections, was designed with a tip inlet relative Mach number of 1.15 and a tip diffusion factor equal to 0.382.

Two variable geometry stator configurations, derived from 65 series airfoil sections, were designed. One stator has a rear flap segment for trailing edge metal angle control and a fixed forward segment. The other stator has two adjustable segments for independent control of both leading and trailing edge metal angle.

INTRODUCTION

Advanced air-breathing propulsion systems require lightweight compact compressors capable of high performance. These compressors must have a wide range of operation and a large stall margin, and they should be

insensitive to inlet flow distortion. Advances in compressor technology have been evidenced by continual increases in rotor speed, stage loading in terms of D-factor, and reduction in stage length. Although further improvement is possible through optimizations and improved combinations of the above parameters, severe aerodynamic and mechanical limitations (such as increased losses and decreased stall margin) are imposed as a result of arbitrarily extending any one of the parameters beyond current design practice. It appears that significant advancements in compressor technology require (1) advanced rotor and stator concepts in terms of improved blading for high flow Mach numbers and loading levels, (2) high lift devices for stators and rotors, and (3) a more adjustable geometry to extend the stall-free flow range. Progress in any of these areas may result in a sizable reduction in the number of compressor stages required for any specific application and an improved compressor.

A program was initiated to investigate variable geometry concepts as applied to the guide vane and stator blade rows in a single-stage, 0.5 hub/tip ratio compressor. Variable geometry inlet guide vanes in the form of movable flaps and variable chord angle stators have been successfully applied to operational turbojet engines to improve range capability at high flight Mach numbers. The objective of the present program is to investigate the potential of variable geometry features such as variable camber and adjustable flaps to further increase the stable operating range of the compressor stages. In addition, the feasibility of combining variable geometry features with high lift devices such as slots was evaluated as part of the design effort. A secondary objective is to collect blade element data for design use. This report presents the results of an analysis conducted to evaluate the effectiveness of variable geometry features. One set of variable geometry guide vanes, a rotor blade row, and two variable geometry stator vane rows were designed for test. The design of the supporting single-stage test rig is also described.

A meanline analysis was conducted to determine the stage type that would be most suitable for the investigation of variable geometry concepts. Design vector diagrams were established for a rotor with a hub/tip ratio of 0.5, a tip diameter of approximately 43 in., and blade loading and Mach number values consistent with current design practice. An analysis

of the off-design vector diagram requirements for a hypothetical second stage was also made. Variable geometry features applicable to guide vanes and stators were then evaluated conceptually, and those that offered the potential for the required off-design vector diagram adjustment without severe mechanical limitations were selected for more detailed design evaluation.

Two candidate variable geometry guide vane designs were considered. The final selection of an inlet guide vane configuration was based on cascade tests from Reference 1. Slot geometry variables for a slotted stator, designed to improve turning at high incidence angles, were also evaluated in the annular cascade (Reference 1).

As part of the overall design effort, a detailed evaluation was made of blading and test rig stress and vibration characteristics. It was indicated from this study that part-span shrouds would be required for the flow generation rotor for vibration damping.

The investigation of variable geometry guide vanes and stators will be conducted in a single-stage compressor test rig that was designed and built by Pratt & Whitney Aircraft for the evaluation of advanced compressor concepts. This test rig meets the design hub/tip ratio and tip diameter requirements for the program. Screens for producing radial and circumferential distortions were also designed.

PRELIMINARY ANALYSIS

Statement of the Problem

Advanced compressors for supersonic cruise aircraft must provide efficient operation over a wide range of equivalent flow and rotor speed. As flight speed increases above M = 1.0, compressor inlet temperature rises and equivalent rotor speed decreases, which leads to increased difficulty in flow matching between the front and rear stages of the compressor. Figure 1 shows the movement of the operating point on a typical compressor map between sea level takeoff (SLTO) or design point and high Mach number cruise (cruise) or off-design operation. The operating point approaches the stall line as equivalent flow and speed are reduced.

The variation of operating points between SLTO and cruise conditions

is shown in figure 2 on typical pressure rise-flow coefficient characteristics for front, middle, and rear stages of a fixed-geometry compressor. The cruise operating point for the front stage is relatively close to the stall limit, whereas the middle stage operating point undergoes little change; the rear stage operating point tends to move toward the choke limit with equivalent speed and flow reduction. The front stages of the compressor thus present the greatest problem concerning stage matching at cruise conditions.

This problem is further illustrated by the rotor inlet velocity diagrams for one radial station in figure 3. This figure illustrates the velocity vector changes corresponding to first-stage operating conditions. The shaded area in the left side of the figure represents the stall-free range of inlet air angle, β_1', for the indicated rotor blade. (Symbols are defined in Appendix A.) When these limits are exceeded, flow separation occurs on the blade surfaces, resulting in loss of efficiency and possible stage stall, which may lead to compressor rotating stall or surge. The high Mach number cruise vector diagram for a fixed geometry guide vane is indicated by the dashed line. Because the reduction in equivalent flow (and axial velocity) from SLTO to cruise conditions is proportionally greater than the reduction in wheel speed, the rotor blade inlet relative air angle in the diagram exceeds the stall air angle limit. Thus, the operating range requirement from design to cruise conditions exceeds the range capability of this rotor element in the stall direction. Even if the range capability of the stage were not exceeded, loss in stall margin and efficiency would be highly probable.

To return the rotor blade inlet relative air angle to the stall-free region, it is necessary to change the absolute air angle, β_1, by the amount, $\Delta\beta_1$, as shown in the right side of figure 3. This can be accomplished by incorporating variable geometry features in the guide vane design to provide the desired guide vane turning at off-design operating conditions.

Figure 3 refers to one radial location of one blade row. Detailed analysis of this problem for advanced engine compressor design requires consideration of (1) spanwise variation of rotor prewhirl, (2) multistaging, (3) Mach number and loading limitations, and (4) mechanical feasibility. A preliminary analysis was performed to select a stage type, as characterized

by rotor prewhirl, that would be best suited for the evaluation of variable geometry guide vane and stator blade rows in a single-stage compressor. The rotor for the selected stage was specified to have a hub/tip ratio of approximately 0.5, blade loading and Mach number values consistent with current design practice, and a radially constant exit total pressure.

The computer programs used for stage type analysis and subsequent vector diagram and blade geometry analyses are described in Appendix B. A description of the stage flowpath geometry and location of axial and radial calculation stations is also included in Appendix B.

Stage Type Selection

Consideration was given to the type of stage (as characterized by SLTO design point inlet guide vane swirl angle) that would be best suited for the application of variable geometry concepts. Of primary concern in this preliminary analysis was the selection of a design point swirl distribution that (1) would be generally consistent with the aerodynamic design of a typical high cruise Mach number compressor front stage and (2) would provide the most effective adjustment of rotor inlet relative air angle for a specified change in inlet guide vane geometry.

A meanline analysis was performed using the flowpath geometry and SLTO performance of a high cruise Mach number production engine compressor front stage. The purpose of the analysis was to evaluate the influence of SLTO design point swirl angle on the change in rotor inlet relative air angle produced by a given change in inlet guide vane turning. A 25-degree change from the design point guide vane turning, an equivalent rotor speed of 70% of the design speed, and an equivalent flow corresponding to a flight Mach number of approximately 3.0 at 65,000 ft altitude were also specified. For this analysis, the SLTO design point swirl angle at the meanline diameter was varied from -30 to 30 degrees without regard to spanwise swirl distribution or the influence of swirl distribution on axial velocity distribution (i.e., the meanline axial velocity was maintained constant over the range of meanline swirl angles).

Data for the SLTO design point and cruise conditions of this pre-

liminary study were as follows:

SLTO Design Point		Cruise	
$N/\sqrt{\theta}$	= 6700 rpm	$N/\sqrt{\theta}$	= 4690 rpm
$W\sqrt{\theta}/\delta$	= 289.7 lb/sec	$W\sqrt{\theta}/\delta$	= 164.5 lb/sec
$\bar{P}_2/\bar{P}_1$	= 1.40		
$\bar{P}_1$	= 14.69 psia		
$\bar{T}_1$	= 518.6°R		
$\bar{\omega}'$	= 0.03		
d_i	= 20.9 in.		
d_o	= 43.1 in.		

$-30 \text{ degrees} \leq \beta_1 \leq 30 \text{ degrees}$

The meanline diameter was defined as

$$d_m = \left[\frac{d_o^2 + d_i^2}{2}\right]^{1/2}$$

Meanline velocity triangles were calculated for several values of β_1 between the limits indicated above. The resulting values of rotor inlet relative Mach number and air angle, and air turning angle were subsequently utilized to establish SLTO design point rotor blade leading edge metal angles from P&WA cascade loss data correlations for circular arc airfoils. The metal angles corresponded to approximately minimum loss incidence for each value of β_1. Rotor inlet relative air angle and Mach numbers were similarly calculated as a function of β_1 for the indicated cruise conditions. The values of cruise relative air angle and Mach number were combined with the SLTO rotor blade geometry to determine (from the cascade loss data correlation) the stable operating range of the rotor at cruise conditions. The resulting operating range, in terms of rotor inlet relative air angle, is shown as a function of SLTO swirl angle in the lower curves of figure 4. Stable operating range is defined in this analysis as the range of relative air angle (or incidence angle) within which the loss coefficient, $\bar{\omega}'$, does not exceed the minimum value by more than 0.04. (Note that this incidence angle range corresponds to stable operating limits but not necessarily to acceptably low loss and high efficiency.) The rotor inlet relative air angle obtained with SLTO design point swirl at cruise conditions (i.e., fixed-geometry stage) is outside the stable cruise operating

range as shown in figure 4a. When the SLTO design point swirl angle is increased 25 degrees (as with a variable geometry inlet guide vane), the resulting relative air angle moves closer to the stable cruise operating range, as indicated by the dashed curve in figure 4a. This curve is approximately tangent to the upper limit of stable operation at a SLTO swirl angle of zero degrees and diverges from the stable operating range as the SLTO design point swirl angle is increased or decreased from zero degrees.

Inlet relative Mach numbers for the SLTO and cruise conditions are shown as a function of SLTO swirl angle in figure 4b. For the SLTO conditions used in this analysis, the Mach number that corresponds to zero swirl is 1.12 and increases to 1.4 at -30 degree swirl. It was considered that negative swirl angles at SLTO conditions would result in prohibitively high rotor tip velocities, and stage types characterized by negative swirl were therefore considered unacceptable for this program. For positive SLTO swirl angles, the effectiveness of a change in swirl at cruise conditions is seen in figure 4a to diminish with respect to stable operation as swirl angle increases.

This preliminary analysis thus shows that (1) operation at rotor speed and flow typical of Mach 3.0 cruise conditions with a fixed-geometry front stage may be unstable (depending on the SLTO compressor match point),(2) an increase in swirl angle at cruise conditions tends to restore the rotor inlet relative air angle to the stable operating region, and (3) the most effective change in cruise relative air angle produced by a change in swirl angle is obtained when the SLTO design point swirl angle is zero. These observations are generally consistent with the results of a more detailed evaluation of the influence of swirl distribution on rotor inlet conditions presented in Reference 2. An axial-inlet type stage was therefore selected for detailed design study.

DESIGN POINT VECTOR DIAGRAM ANALYSIS

The following conditions were specified for the rotor at design equivalent rotor speed:

1. Zero prewhirl (based on meanline analysis)

2. Tip inlet relative Mach number of approximately 1.1

3. Tip D-factor loading in the range, 0.3 to 0.4

4. Pressure ratio, 1.35

5. Constant hub-to-tip rotor exit total pressure

Zero rotor prewhirl at design point operation was determined in the meanline analysis to provide the best improvement of rotor inlet relative air angle for a specified swirl change at off-design conditions with respect to an estimated stall limit. A tip inlet relative Mach number of approximately 1.1 was selected in conjunction with the intended use of circular arc airfoil sections. This Mach number is near the limit of reliable cascade design data for the circular arc series airfoil, and engine compressor experience at this Mach number level is well documented. The conservative D-factor loading level, 0.3 to 0.4, was considered for this program to ensure a wide, low-loss range of rotor operation to permit evaluation of the variable geometry concepts over as wide a range of flow and rotor speed as possible. A rotor pressure ratio of 1.35 was selected as representative of the state-of-the-art for a compressor front stage.

A parametric study was performed to determine the weight flow and rotor speed that would provide the specified inlet relative Mach number and D-factor loading. The Pratt & Whitney Aircraft computer programs described in Appendix B were used for this study, as well as for subsequent vector diagram and blade geometry analyses. Streamline curvature, entropy gradient, and enthalpy gradient effects were included in the design. A corrected rotor speed of 6050 rpm and a corrected weight flow of 265 lb/sec were selected. The resultant rotor speed tip Mach number was 1.15 and the rotor tip diffusion factor was 0.38 based on zero prewhirl conditions. This analysis defined the velocity triangles for various span locations for the leading and trailing edges of the rotor.

The design point exit air angle distribution for the stator was selected to satisfy the inlet requirements of a representative state-of-the-art second stage. Because an axial inlet air angle was found in the stage-type analysis to give the maximum rotor incidence adjustment per degree change in prewhirl angle, the stator exit angle was selected to return the first-stage flow to the near axial direction. Thus, the stator trailing edge

geometry change required to satisfy second-stage inlet requirements at off-design conditions would be minimized.

The resulting design point vector diagrams for the inlet guide vane, rotor, and stator, corresponding to radial location of 10, 50, and 90% of span from the tip, are presented in figure 5. Vector diagrams are presented for the trailing edge of the inlet guide vane, leading and trailing edge of the rotor, and leading and trailing edge of the stator. Radial distribution of stage inlet Mach number, and axial velocity distributions at the guide vane leading and trailing edge and rotor leading edge are presented in figure 6. Radial distribution of rotor inlet relative Mach number, inlet and exit relative air angle, and diffusion factor are presented in figure 7. Radial distribution of stator inlet and exit air angle, diffusion factor, and inlet and exit axial velocity are presented in figure 8. The stator exit air angle is within 5 degrees of the axial direction, and the stator loading is conservative. The stator tip exit axial velocity results in a second-stage rotor tip inlet relative Mach number of approximately 1.1.

Additional design point vector diagram data are tabulated in Tables C-1, C-2, and C-3 of Appendix C. Values are presented for the leading and trailing edge stations of each blade row.

DESIGN POINT BLADE GEOMETRY

Inlet Guide Vanes

The selection of inlet guide vane geometry for this stage is an iteration between the SLTO and cruise geometry required to provide the respective SLTO and cruise swirl distributions. For design point (SLTO) conditions the IGV turning was zero. The blade sections however were selected to produce about two-thirds of the turning required for cruise conditions. The design method of Reference 3 was used to establish the basic airfoil geometry. The resultant camber varied linearly from 44 degrees at the hub to 38.5 degrees at the tip. The design point and off-design geometries are obtained by actuating two articulated flaps to decrease or increase camber. This approach provided reasonably aerodynamically clean profile shapes for the design and off-design geometries. The axial flow geometry of the variable camber guide vane was

selected to provide nearly zero prewhirl with minimum profile blockage.

The method used to determine effective camber and trailing edge metal angle for the design point geometry is presented in a subsequent section of this report.

A conservative value of guide vane loss coefficient, 0.143, was used for stage performance calculations; this was the same value that was used for the high cambered off-design guide vane position. These loss assumptions were applied in the performance calculations prior to the loss coefficient results obtained in the preliminary annular cascade investigation of a variable camber guide vane (Reference 1).

The guide vane row was designed with 20 guide vanes, which provided a solidity distribution commensurate with current design practice for a compressor front stage. Solidity, thickness ratio, and chord length for the basic airfoil hub and tip sections are as follows:

	Hub	Tip
Solidity	1.47	0.67
Thickness Ratio	0.09	0.09
Chord Length, in.	4.52	4.52

Additional geometry details of the basic airfoil sections and the design point guide vane configuration are presented in table C-4 of Appendix C.

Rotor

Circular arc airfoil sections were utilized in the rotor blading design because of the transonic blade tip inlet relative Mach numbers that will be encountered at design rotor speed. Circular arc airfoil loss and deviation data correlations from P&WA cascade tests were available for the Mach number range of interest.

The rotor assembly comprises 34 blades. The selected blade row solidities and span/chord ratio (mean radius s/c = 2.829) are consistent with current design practice of a compressor front stage. Hub and tip values of solidity, thickness ratio, and chord length are tabulated below.

	Hub	Tip
Solidity	1.52	1.034
Thickness Ratio	0.085	0.030
Chord Length, in.	3.147	4.106

Rotor leading and trailing edge metal angles and incidence angle distributions for design point operation are presented in figure 9. Radial distribution of loss coefficient and deviation angle are presented in figure 10. Additional rotor blade geometry details are presented in table C-5 of Appendix C.

The vibration and stress analysis that was conducted for the rotor indicated that a part-span shroud would be required at a radial location of approximately 40% of span from the tip to avoid critical resonance frequencies within the operating speed range of the rotor. The streamline analysis computer program (Appendix B) was used to determine the streamline pitch angles at the rotor blade leading and trailing edges at the desired radial location. The pitch angle of the shroud was selected as the average of these two angles.

Figure 11 presents a schematic of the shroud and identifies the aerodynamic design parameters. The thickness of the shroud is determined from structural requirements. The shroud sweep angle and thickness ratio are determined as a function of the critical Mach number (M_{crit}) by means of an iterative procedure. A critical Mach number (above which the shroud profile loss increases rapidly) exists for each thickness ratio, and the sweep angle and thickness ratio were varied until a combination of the two resulted in a value of M_z/M_{crit} equal to or less than 0.8. The shroud geometry thus defined is tabulated below:

Span Location (LE), percent from tip	40
Thickness, t, in.	0.245
Chord, c, in.	0.930
Pitch Angle, deg	1.80
Sweep, deg	0

Stator

The stator configuration comprises 40 vanes. The design point vanes are basically 65 series airfoil sections. Solidity, thickness ratio, and chord length values tabulated below for the hub and tip section are commensurate with state-of-the-art stator design.

	Hub	Tip
Solidity	1.372	1.012
Thickness Ratio	0.080	0.080
Chord Length, in.	2.608	3.358

Equivalent circular arc leading edge metal angles were established for near minimum loss incidence, and trailing edge metal angles were defined on the basis of the required turning and NASA deviation. Radial distribution of leading and trailing edge equivalent circular arc metal angles and stator incidence angle are presented in figure 12. Predicted design point loss coefficient and deviation angle distributions are presented in figure 13. Additional geometry and performance details are presented in table C-6 of Appendix C. A more detailed description of the design point geometry with respect to variable geometry features is presented in a subsequent section.

OFF-DESIGN PERFORMANCE ANALYSIS FOR DESIGN POINT GEOMETRY

An analysis was performed to determine the rotor and stator blading performance for the design point geometry operating at off-design conditions. The off-design rotor speed was selected as 70% of design equivalent speed, with a corresponding rotor tip velocity, U_{tip}, of 797 fps. The corresponding weight flow of 143.3 lb/sec was selected to be typical of the requirements for supersonic flight.

An indication of off-design performance is obtained from examination of the match between the calculated incidence angle distribution at off-design operating conditions and the incidence angle range for which the loss coefficient does not exceed the value $\bar{\omega}_{min} + 0.02$. The blade element losses generally increase rapidly beyond this low-loss range, with an attendant loss in efficiency. Rotating stall may develop, which could lead to compressor surge, if the low-loss incidence angle range is exceeded in the positive direction over an appreciable part of the span.

The off-design incidence angle distributions for the design point geometry stage rotor and stator are each compared with the corresponding low-loss incidence angle distributions in figures 14 and 15, respectively. For both blade rows, the off-design incidence angles are greater than the upper limit of low-loss incidence over nearly the entire span. The relatively high off-design incidence angles in the rotor hub region result from the influence of the design flowpath wall curvature on the rotor inlet axial velocity distribution.

The calculated rotor and stage efficiencies for off-design operation of the design point geometry stage are 76% and 68%, respectively, compared with the design point rotor and stage efficiencies of approximately 92% and 85%, respectively.

Figure 16 shows a plot of the off-design incidence distribution calculated for a representative state-of-the-art second-stage rotor operating behind the fixed-geometry first stage at off-design conditions. Comparison of the off-design incidence distribution with the low-loss incidence range for this rotor indicates that the tip incidence angle falls within the low-loss range, whereas the hub incidence angle is above the upper limit of low-loss incidence. The calculated efficiency of the second-stage rotor at off-design conditions (with a fixed-geometry first stage) was 77% compared to the design point efficiency of 89%.

The results of this analysis thus show that stall of the first and second stages may be encountered when the stages are operated at a typical high Mach number cruise equivalent rotor speed and flow condition with a sea level static design point fixed geometry.

ANALYSIS AND SELECTION OF OFF-DESIGN IGV TURNING DISTRIBUTION

Three factors were considered in the selection of off-design guide vane turning distribution;

1. Rotor incidence angle
2. Rotor loading (in terms of static pressure rise coefficient, $\Delta p/q$)
3. Spanwise change in stator inlet angle from design to off-design operation.

The primary objective of this study was to determine the guide vane swirl distribution that would provide spanwise distribution of low-loss rotor incidence and acceptable rotor loading at the off-design operating conditions. A third criterion for the selection of guide vane turning concerned the relative values of stator hub and tip inlet air angle change from design point to off-design conditions. From the standpoint

of avoiding the mechanical complexity associated with a stator having a variable leading edge metal angle, it would be desirable to minimize the spanwise variation of this angle change, provided that the first two criteria are satisfied.

The following linear distributions of guide vane turning were evaluated:

β_1 Tip, deg	β_1 Hub, deg
0	0
20	15, 25, 35
30	15, 25, 35, 45

For this part of the analysis, the guide vane exit axial velocity for design point geometry ($\beta_1 = 0$) was assumed constant across the span (i.e., the local inner wall curvature effect on the velocity gradient near the ID was not accounted for pending final definition of the flowpath). The influence of this assumption on the results of the analysis is discussed in another part of this section. The off-design operating conditions were those specified in the previous section.

Rotor incidence and loading at the hub and tip sections (90 and 10% of span from the tip) are plotted in figures 17 and 18, respectively, as functions of $\beta_{1\ hub}$ for the two values of $\beta_{1\ tip}$ ($\beta_{1\ tip}$ = 20 deg and 30 deg). It is immediately apparent in figure 17 that the rotor hub section incidence is more controllable than the tip section incidence by changes in guide vane turning. This is partially attributed to the redistribution of axial velocity necessary to satisfy radial equilibrium when swirl is introduced. Figure 19 shows the radial distributions of axial velocity for three linear swirl distributions, including zero swirl. For both cases of positive swirl, it can be seen that the axial velocity is proportionally lower in the tip region than in the hub region; thus, more guide vane turning is required in the tip region to produce a given change in rotor incidence. The characteristic distribution of rotor inlet relative air angle for design point conditions (high at the tip and low at the hub) also contributes to the relative influence of swirl on the hub and tip section incidence angle change. It can be shown trigonometrically that there is less change for high inlet relative air angles than there is for low relative air angles per degree change in swirl angle. Similar results were obtained in the analysis presented in Reference 2.

The maximum swirl in this evaluation ($30°_{tip}$ - $45°_{hub}$) produced a rotor tip section incidence change of only -3.6 degrees compared to a change of about -7.5 degrees required to achieve minimum loss incidence (approximately in the middle of the low-loss incidence range indicated in figure 17). The corresponding hub section incidence for this swirl distribution is 6 degrees beyond the negative incidence limit of the hub section low-loss range indicated in the figure. Any further attempts to reduce tip incidence with increased swirl angle would only aggravate the situation at the hub section. Swirl distributions of either $20°_{tip}$ - $32°_{hub}$ or $30°_{tip}$ - $25°_{hub}$ would result in a near-minimum-loss incidence angle at the hub section and about 3 degrees above the low-loss range at the tip section.

The influence of guide vane swirl distribution on rotor loading is shown in figure 18. The hub section loading is more sensitive to guide vane tip swirl than the tip section. This result generally follows from the redistribution of axial velocity (or static pressure) with changes in swirl distribution when radial equilibrium is satisfied. Loading level in the tip region does not appear to be a problem for guide vane hub section exit air angles between 15 and 35 degrees. For hub section swirl angles above 35 degrees, the low values of loading level reflect an unacceptably low level of work. Loading levels in the hub region, although tending toward the upper limit of current design practice, are considered acceptable because the corresponding inlet relative Mach number is low (approximately 0.36).

A third consideration for guide vane selection concerns the change in stator inlet air angle from the design operating point to off-design conditions. If a variable leading edge stator is used to adjust stator incidence angle, it would be desirable to maintain the angle change at the tip, $\Delta\beta_{2\ tip}$, as close as possible to the angle change at the root, $\Delta\beta_{2\ hub}$, to avoid mechanical complexity. Figure 20 shows the effect of guide vane swirl distribution on the hub and tip section values of rotor exit air angle change from design point to off-design conditions. The points of intersection of the hub and tip section curves in figure 20 indicate swirl distributions of $30°_{tip}$ - $40°_{hub}$ and $20°_{tip}$ - $35°_{hub}$ that provide equal changes in the rotor exit absolute air angle at the hub and tip sections. The rotor incidence and loading values from figures 17 and

18 that correspond to these swirl distributions are as follows:

Swirl Distribution	i_m, deg		$\Delta p/q$	
	Hub	Tip	Hub	Tip
30°_{tip} - 40°_{hub}	-10	4.6	0.45	0.23
20°_{tip} - 35°_{hub}	-2.5	5.5	0.62	0.32

The 20°_{tip} - 35°_{hub} swirl distribution is very close to the 20°_{tip} - 32°_{hub} distribution in figure 17 that provided a hub section incidence near minimum loss and a corresponding tip incidence that was different from the best available choice of tip incidence (within the swirl range analyzed) by only a fraction of a degree. The hub loading value of $\Delta p/q = 0.62$ was of some concern, but it was expected that the correction of radial static pressure gradient to account for the design flowpath inner wall local curvature would reduce this value. The 20°_{tip} - 35°_{hub} swirl distribution was selected for further evaluation with wall curvature effects accounted for.

Figure 21 shows the radial distribution of guide vane exit axial velocity with and without inclusion of effects of local wall curvature. The reduction of axial velocity in the hub region produced by the curvature resulted in a slight reduction in the static pressure rise coefficient and a slight increase in the incidence angle in the rotor hub region as shown in figure 22. The static pressure rise coefficient at the hub section is seen to be decreased from 0.67 to 0.52. The incidence angle at the hub section is increased from approximately -9 degrees to -5 degrees.

On the basis of the foregoing analysis, the 20°_{tip} - 35°_{hub} guide vane swirl distribution was selected for the cruise condition. For this guide vane swirl distribution, the rotor tip still appears critical for the cruise operation. However, the decrease in loading should result in some increase in the stall-free range of incidence above those shown in figures 17 and 22. It is believed that the rotor will operate without stall at the cruise condition.

CALCULATION OF OFF-DESIGN STATOR FLOW ANGLES

Stator Inlet Air Angle

The off-design stator inlet air angle distribution for the selected guide vane swirl distribution was defined on the basis of the known

rotor exit metal angle, NASA deviation angle, and the specified off-design rotor inlet conditions. The resulting stator inlet air angle distribution is presented in figure 23. The design point air angle distribution is shown for comparison. The hub section air angle changed 9 degrees and the tip section air angle changed 15 degrees from design point to off-design operation. The changes in the air angle at 10 and 90% span locations are approximately 15 and 11 degrees, which is only slightly different from the constant 14-degree change for the same radial locations determined in the analysis of guide vane swirl in the preceding section. The difference is due to the influence of flowpath wall curvature (at the guide vane exit) on the radial distribution of axial velocities, as previously discussed.

The dashed line in figure 23 is the air angle distribution that corresponds to the upper incidence angle limit of the low-loss incidence range ($\bar{\omega} \leq \bar{\omega}_{min} + 0.02$). The difference between the off-design distribution and the dashed line indicates the degree of mismatch for a fixed-geometry leading edge stator.

Stator Exit Air Angle

The stator exit air angle for off-design operation was initially approximated by determining the range of stator exit air angles that provided suitable inlet conditions for the hypothetical state-of-the-art second-stage rotor. The second-stage rotor inlet conditions were evaluated in terms of incidence, loading (static pressure rise, coefficient $\Delta p/q$), and stator exit axial velocity. Calculated values of these parameters corresponding to radial locations near the hub and tip sections (90 and 10% span, respectively) are presented as functions of the stator exit air angle in figures 24, 25, and 26. Figure 24 indicates that the hub (90% span) section of the rotor is within the low-loss incidence range for stator exit air angles between 26 and 40 degrees. The tip (10% section) is within its low-loss range for stator exit air angles between -4 and 30 degrees. Stator exit air angles between 26 and 30 degrees satisfy the low-loss incidence range at both the hub and tip section. Because the stator exit air angles at design speed conditions are nearly radially uniform (within about 3 degrees), the 26- to 30-degree range of stator exit air angles represents approxi-

mately the range within which a radially uniform angle change from design to off-design conditions can be made that will satisfy the second-stage incidence requirement. The range of loading level, $\Delta p/q$, encompassed by this range of stator exit air angles (26 to 30 degrees) is shown in figure 25. The loading level range corresponding to these air angles has a maximum value of $\Delta p/q = 0.415$ near the hub and a minimum value of approximately 0.2 near the tip. Axial velocities out of the stator (figure 26) for the same exit air angle range are generally between 265 fps at the hub and 355 fps at the tip; these values are within current design practice. The final selection of the off-design stator exit air angle, within the range of 26 to 30 degrees, was coordinated with the evaluation of variable geometry stator design, which is discussed in the following section. The resulting stator exit air angle distribution is presented in figure 27. Figure 28 shows the corresponding off-design incidence angle distribution for the second-stage rotor.

VARIABLE GEOMETRY INLET GUIDE VANE AND STATOR BLADING

Variable Geometry Concepts

Inlet Guide Vanes

Five of the variable geometry guide vane configurations that were screened for general aerodynamic and mechanical feasibility are illustrated in figure 29. It was considered on the basis of the level of turning required to restore stable operation at the cruise condition ($\Delta\beta \geq 30$ degrees), as determined in the meanline evaluation of stage types that single-flap guide vane configurations (figure 29) would be inadequate. A single-flap guide vane would probably encounter high deviation angles and correspondingly high losses at the high flap angles that would be required. The addition of a slot in the flap section of this guide vane configuration was considered as an aid for flow turning at high flap angles. The offset flap appeared slightly more desirable from the standpoint of aerodynamic cleanliness at off-design by virtue of the flow energy addition at the suction surface between the fixed leading edge section and the flap section. Two alternatives to the single-flap type of variable geometry were considered jointly by NASA

and Pratt & Whitney Aircraft: (1) the variable camber and (2) the venetian blind guide vane concepts shown in figure 29. Although the mechanical complexity of these two concepts appeared to be greater than that of a single-flap guide vane, it was considered that they offered greater potential for the achievement of low-loss high turning. The variable camber guide vane was configured with a slot between the two articulated flap sections to aid turning during very high camber operations.

The variable camber and venetian blind inlet guide vane concepts were evaluated in an annular cascade tunnel to determine their design and off-design geometry loss as part of the overall design effort (Reference 1). The cascade inlet guide vanes were designed with 63 series airfoil sections in the cambered position.

The criterion for selection of one of these two candidate guide vane designs was midspan total pressure loss, or wake size obtained with the guide vanes in the axial flow position. Wake total pressure profiles for the two configurations are shown in figure 30. The wake profile for both configurations in the cruise high turning position is included for comparison. The variable camber guide vane configuration was selected because it had a significantly lower loss in the axial flow position than the venetian blind guide vane configuration.

Stators

Preliminary evaluation of stator inlet and exit air angle requirements for proper stator leading edge and second-stage rotor inlet matching at design and off-design operation indicated a possible need for independent control of both the leading and the trailing edge geometry. This consideration precluded the use of variable stagger stator configurations. Schemes that could accommodate a relatively wide variation of inlet air angle and provide the required range of exit air angle are shown in figure 31. The leading and trailing flap scheme was eliminated because of an undesirable aerodynamic shape in the low camber position, and the retractable leading edge slat-trailing edge flap scheme was eliminated because of the mechanical complexity of the retractable slat. The third scheme, shown in figure 31, involves a double-flap stator. Except for the requirement of a dual actuation system, the double-flap stator was not considered a complex mechanical design. The last two schemes, shown

in figure 31, incorporate a flap for control of the exit air angle. The fourth scheme uses a solid forward section, whereas the fifth scheme has a slot near the leading edge of the fixed forward section to aid flow turning at high incidence angles. The double-flap stator and single trailing edge flap stator (which could be designed with or without a slot pending the evaluation of off-design incidence angles) were selected for the test program.

The slotted stator configuration was investigated in an annular cascade rig, as part of the overall design effort, to determine the effectiveness of a slot near the leading edge at high incidence angles (Reference 1). Three slot configurations, located at approximately 20% chord from the leading edge, were evaluated. The test stators were 65 series airfoil sections with a chord length of 6.5 in. For these tests, an off-design incidence angle of approximately 15.5 degrees was selected, and the trailing edge metal angle of the stators corresponded to the design point mean radius value. (The stator was tested without a flap.) Only a slight reduction in loss coefficient resulted from the addition of a slot.

An exploratory cascade test was performed concurrently at the NASA Lewis Research Center with a similarly slotted stator having a flap. The results of these tests indicated that the slot produced a negligible influence on the wake size when the flap section was rotated to unload the airfoil. This suggested that the stator incidence range might be sufficiently increased to accommodate the higher off-design incidence condition without the aid of a slot. It was therefore decided to design and test the single-flap stator initially without a slot.

Variable Geometry Inlet Guide Vane Design

The 63 series airfoil sections were selected for the inlet guide vane because of the relatively high turning required at off-design operating conditions. The variable camber guide vane was required to provide axial inlet flow at design rotor speed and 35-degree hub and 20-degree tip turning at 70% of design rotor speed, with a low profile loss at both conditions. The 63 series airfoils have demonstrated low losses at moderately high values of turning.

A basic 63 series guide vane was designed with 44-degree hub and 38.5-degree tip camber distribution, which represented about two-thirds of the camber required for off-design turning. The design method of Reference 3 was used to establish the blade geometry. The basic guide vane design was slightly modified by extending the midspan camber lines of the fixed forward segment and the first flap to the hub and tip and slightly modifying the hub-to-tip camber distribution of the rear flap section. These modifications were made to alleviate hinge line problems that would be encountered with twist. Hub, midspan, and tip sections of the basic airfoil, as modified, are shown in figure 32. The axial flow and high turning (cruise) geometries are obtained by actuating the two articulated flaps to decrease or increase camber from the basic guide vane design values. This approach provided reasonably aerodynamically clean profile shapes for the design and off-design geometries. The slot that is formed between the two articulated flap sections is provided to aid flow turning at high camber angles. The slot width increases as camber angle increases, thus permitting a progressive increase of slot flow to energize the boundary layer on the suction surface of the rear flap section. The radial distribution of leading and trailing edge metal angle and the chord angle are presented in figure 33 for the unmodified and modified basic airfoil sections.

The axial flow (design point) position of the guide vane was selected on the basis of providing nearly zero radial swirl distribution and minimum profile blockage. The 63 series airfoil design data (Reference 3) were used as a guideline to establish the design point and off-design camber angle distribution. For the design point geometry, the basic guide vane is effectively uncambered 19.6 degrees (a change in trailing edge metal angle from the modified basic airfoil design position). The center segment of the guide vane was rotated (uncambered) 12.67 degrees. Because the metal geometry terms of the variable camber guide vane in the axial position are not related to the corresponding terms used for the basic airfoil design, it was necessary to redefine an effective chord angle, camber, and trailing edge metal angle. An effective chord angle was defined as the line connecting the same leading and trailing edge points as those of the modified basic airfoil. Figure 34 shows the hub, midspan, and tip sections of the guide vane in the axial position. The

midspan effective chord line was aligned with the compressor axis, resulting in hub and tip chord angles of 1.5 degrees and -1.5 degrees, respectively. From Reference 3, the corresponding values of camber angle are 5 degrees and -5 degrees; and the corresponding values of trailing edge metal angle are 1 degree and -1 degree. The deviation angle associated with this level of camber and metal angle is less than 1 degree. This resulted in a predicted hub-to-tip air angle distribution of approximately 0 degree to -2 degrees, which was considered acceptable in conjunction with the low-loss profile requirement.

The selected camber distribution that was expected to produce the required air angle turning (35 degree hub - 20 degree tip) at off-design operation was 57.2 degrees at the hub to 48.2 degrees at the tip. This reflects a camber (trailing edge metal angle) increase of 11 degrees over the modified basic airfoil camber. The center segment was rotated 7.33 degrees (to increase camber). Hub, midspan, and tip sections of the off-design guide vane geometry are shown in figure 35. The guide vane linkage was designed to accommodate higher camber angles (up to 15 degrees more than the cruise camber) to ensure adequate rotor prewhirl capabilities at off-design conditions.

A constant loss coefficient of 0.143 was used for both the design point and off-design guide vane configuration for the purpose of stage performance calculations. This high level of loss was intended to reflect profile irregularities of the design point geometry and the high turning loss of the off-design geometry. The losses subsequently measured in the annular cascade investigation (Reference 1) were substantially lower than the value assumed for design calculation purposes.

Chordal locations of the pivot points for the articulated flap sections were based on consideration of structural integrity, mechanical complexity, and aerodynamic cleanliness of the design and off-design geometries. The final vane design, showing the flap pivot sections, is presented schematically in figure 36. Sections V-V and D-D in figure 36 illustrate the extent of vane surface irregularity that results from the linkage design. These irregularities extend 1.7% of the span from the outer wall and 2.0% span from the inner wall. The contours at all other span locations are similar to section E-E. Section E-E shows the formation

of a nearly full-span slot between the two flap sections as the camber angle increases. This slot is intended to aid turning at the high camber angles. The trailing and leading edges, respectively, of the first and second flap were configured to produce a slot geometry consistent with the slot design technique defined in Reference 4. The slot is partially open in the design point geometry position to reduce circulation in the slot cavity on the pressure surface. Additional geometry details for the off-design guide vane configuration are presented in table C-4 of Appendix C.

Variable Geometry Stator Design

Design Point Geometry

The single trailing edge flap stator (Stator A) was designed with 65 series airfoil sections. Values of aspect ratio, solidity, and thickness ratio were selected according to current design practice for similar stages. Leading and trailing edge metal angles were determined for the specified inlet and exit air angles using P&WA 65 series airfoil cascade loss and deviation data correlations. The selected leading edge metal angle corresponded closely with the minimum loss incidence. Hub, midspan, and tip sections of the Stator A design point geometry are shown in figure 37.

The double-flap stator configuration (Stator B) design point geometry was also developed from 65 series airfoil sections; the vanes were designed to preserve as much as possible of the basic 65 series airfoil shape. Pursuant to this objective, the two flap segments were selected to have approximately the same chord length and an overlap of 15% of the basic 65-series chord length, as shown in figure 38. The leading edge of the forward flap is identical to the basic 65-series airfoil up to 30% of the forward flap chord. The geometry of the remainder of the forward flap was generated by combining the thickness distribution for a 65-series airfoil (having a chord length equal to the flap chord and thickness at 30% chord as defined by the basic airfoil) with the basic airfoil suction surface contour. For the rear flap, the uncovered section (55% to 100% of the basic airfoil chord) is identical to the basic 65-series airfoil geometry. A NACA-4-digit series airfoil shape was used for the covered leading edge section (40 to 55% basic chord) to permit low-loss

operation over a wide range of incidence angles. To obtain the leading edge contour, it was assumed that the thickness at the interface of the basic 65-series airfoil part of the rear flap and the leading edge section of the rear flap was the maximum thickness of a 4-digit airfoil, which would occur at 30% of the 4-digit airfoil chord. With the arbitrarily selected overlap of 15 percent it was then possible to determine the thickness distribution for the rear flap leading edge section. The camber of this section was selected to provide (1) slightly negative incidence on the rear flap in the cruise position and (2) a smooth blend with the 65-series part of the rear flap. A 4-digit airfoil camber angle of 35 degrees (NACA m4 meanline) satisfied these two criteria with a minimum of blending at the interface. Hub, midspan, and tip sections of the resulting Stator B design point geometry are shown in figure 39. A 0.015-in. slot was provided between the forward and rear flaps of Stator B in the design point configuration to reduce recirculation in the pressure surface cavity that is formed by the two flap sections.

Additional design point geometry details common to both Stators A and B are presented in table C-6 of Appendix C.

Off-Design Geometry

The low-loss incidence range for the off-design geometry stators was defined as the low-loss range of a conventional 65 series airfoil section having a camber distribution commensurate with the off-design flow turning requirement and NASA deviation. Figure 40 shows the low-loss incidence angle range thus defined and the incidence angle distribution of the design point geometry stators operating with off-design guide vane swirl conditions. Figure 40 indicates the incidence mismatch of the fixed-geometry leading edge Stator A configuration at off-design conditions.

The off-design angle setting of the forward flap of the Stator B configuration was selected to provide a suitable distribution of incidence angle within the low-loss incidence range shown in figure 40. The minimum and maximum change in leading edge metal angle possible within the low-loss range are governed by the hub and midspan sections. A maximum angle change of 10.5 degrees is the limit at the hub section, and an angle change of 7.8 degrees is the minimum limit at 60% span. A flap angle change of 9 degrees was selected, which provides hub and tip region incidence angles close to the minimum loss incidence.

The off-design trailing edge metal angle requirements for both variable geometry stator configurations were the same. The trailing edge metal angle was evaluated in terms of the corresponding stator exit air angle near the hub and tip (90 and 10% span sections) and in terms of the second-stage rotor total pressure ratio and efficiency, as functions of the stator trailing edge metal angle change. For this study, three values of chord taper ratio, c_{tip}/c_{root}, were included to provide sufficient data for the evaluation of possible problem areas, such as slanted hinge lines, severe camber distribution, and/or blade twist. The results of the study are summarized in figures 41 and 42. It can be seen in both figures that the chord taper ratio has little effect on the calculated results. (The chord taper ratio for design point geometry is 1.287.) In figure 41, it is seen that the desired range of exit air angles (26 to 30 degrees) determined in the section, "Calculation of Off-Design Stator Flow Angles," for off-design operation is provided by a very limited range of trailing edge metal angle changes (25.5 to 27 degrees).

A flap angle change of 26 degrees was selected to stay within the second-stage low-loss rotor incidence limit at the hub and tip section. The resulting second-stage rotor incidence distribution (figure 28) tends to unload the tip region, which should tend to improve the stall margin of the representative second stage. Hub, midspan, and tip section views of the off-design stator configurations are presented in figures 43 and 44.

In figure 42, the pressure ratio and efficiency of the second-stage rotor are seen to decrease with increasing flap angle change, or, as the rotor incidence becomes more negative. (If the calculations were continued in the direction toward zero flap angle change, the pressure rise would level off and subsequently decrease, and the efficiency would decrease.) The second-stage rotor pressure ratio and efficiency for the 26-degree stator flap angle change and chord taper ratio of 1.287 are 1.09 and 92.8%, respectively.

Off-design geometry and predicted performance data for the two stator configurations are presented in table C-6 of Appendix C.

DISTORTION SCREENS

The effects of radial and circumferential inlet flow distortion on overall stage performance will be evaluated under the program. The distortion requirements are as follows:

1. Radial: Outer two-fifths of the annulus area
2. Circumferential: 90 degrees of the annulus
3. Velocity Distortion: $(V_{max} - V_{min})/V_{max} = 0.237$.

The velocity distortion specified above was calculated on the basis of a total pressure distortion of 0.15 at an average Mach number of 0.60. An average total pressure that satisfies continuity was determined for the required radially distorted profile, and the maximum and minimum velocities were subsequently calculated assuming a constant radial static pressure.

The radial distortion flow conditions for the single-stage rig flowpath are illustrated in figure 45. The distortion screens are located at the forward flange of the inlet case for convenience of installation and modification. The required velocity distortion will be measured at instrumentation station 0. The distortion screen configuration was determined in the following three steps:

1. Calculation of the total pressure distortion at the station 0 Mach number condition (M = 0.426). This is the total pressure to be generated at the screen station assuming isentropic flow and no mixing across the two parts of the distorted profile between the screen location and station 0.
2. Calculation of the equivalent velocity distortion for the Mach number condition at the screen location (M = 0.426).
3. Calculation of the required screen area (height) on the basis of the predetermined flowrates in both parts of the distorted profile and the velocity distribution determined in step 2.

The average Mach number immediately downstream of the screen was determined in the above steps, and it was assumed that this average Mach

number existed immediately ahead of the screen. The calculated total pressure loss in step 1 was:

$$\frac{P_{max} - P_{min}}{P_{max}} = 0.067$$

For the average Mach number of 0.370 just ahead of the screen,

$$\frac{P_{max} - P_{min}}{1/2 \ \rho V^2} = 0.770$$

The screen porosity, according to data presented in NACA CB No. L5F28 for the above pressure loss and average Mach number conditions, was 32%. Screen pressure drop data correlations obtained at Pratt & Whitney Aircraft resulted in a porosity value of 34%. The screen framework design permits the use of either single or double screens. A total screen equivalent porosity of 35% will be used initially.

For the circumferential distortion screens, a similar analysis was conducted and an initial equivalent porosity of 35% will be used.

MECHANICAL DESIGN

Inlet Guide Vane

The variable geometry guide vane configuration, shown in figure 46, comprises a stationary leading edge section and two articulated flap sections. The leading edge section is brazed to the inner and outer cases and functions as a bearing support structure and as a conduit for bearing oil and instrumentation leads. The two variable-position flap sections are moved by a single actuation ring that is attached through a spherical bearing to a hinge pin common to both flaps. The hinge pin translates through an arc-shaped slot in the outer case wall (Section C-C in figure 46). The slot is sealed by the vane platform located at the tip section of the rear flap (Section A-A). Each vane assembly is radially spring loaded at the forward flap hinge axis to provide friction damping of both flaps and to hold the rear flap platform seal in position against the outer case wall. Motion of the rear flap relative to the forward flap is achieved by means of a fixed pivot point located at the end wall sections of the rear flap (Section D-D).

The maximum stress calculated for the fixed forward vane section due to static loads of the rotor, centerbody, and slip ring assembly was 7100 psi, with a negligible corresponding deflection. The maximum aerodynamic load calculated per vane assembly was less than 25 lb_f, which results in negligible stresses in the airfoil or hinge sections. The hinge pins, fabricated from high strength steel and coated with dry film lubricant, were designed as large as practicable to provide adequate bearing and wear surfaces. The actuation ring is fastened in position to the case by means of six bolts. Repositioning of the actuation ring is accomplished manually with no airflow through the rig.

First and second bending vibration frequencies were calculated for the three elements of the inlet guide vane. The leading edge section indicated a resonance frequency of 420 cps for first bending, requiring a rotational speed of over three and a half times the 110% design speed to excite the vane. Because all other calculated resonance frequencies were higher than those for the leading edge section, no vibration problems are anticipated for any portion of the inlet guide vane.

Rotor

Blade Attachment

The rotor disk/blade assembly is shown in figure 47. An existing rotor disk and dovetail blade attachment design was used. The blade hub section was designed with a platform that approximates the contour of the flowpath wall. Rotor blade attachment stresses, calculated for a rotative speed of 6655 rpm (110% of design speed), are summarized in table 1. The combined tensile and bending stress is sufficiently within the indicated 0.2% yield point stress of the AMS 5613 fabrication material.

Table 1. Rotor Blade Attachment Stresses

	Bearing	Shear	Tensile	Bending	Combined Tensile and Bending
Calculated stress, psi	53,500	25,800	20,700	55,900	76,600
0.2% yield point stress, psi (AMS 5613 stainless steel)	101,500	101,500	101,500	101,500	101,500

The calculated steady-state stresses for the rotor disk resulted in an average tangential stress of approximately 44,000 psi at 6655 rpm. The tangential stress represents a disk burst margin of 250% and a yield margin of 195% for the AMS 6304 fabrication material. Disk sections between the blade attachment cutouts were also analyzed for bending and torsion, resulting in calculated stresses of 57,800 psi and 35,500 psi, respectively.

Airfoil Stress and Vibration Characteristics

Steady-state stresses due to centrifugal forces and aerodynamic loading at 6655 rpm were calculated for blade element sections at 11 radial locations. Gas bending stresses were calculated at the leading and trailing edges and on the convex surface at the point of maximum thickness. The restoring effect of the centrifugal forces that tends to reduce the gas bending stresses was considered in the analysis. The net gas bending stress and the tensile stress were added to give the total blade stress. The results of these calculations are presented in table 2. The maximum combined stress of 57,900 psi is within the design limit of the blade material (AMS 5613).

Table 2. Rotor Blade Steady-State Airfoil Stresses

	Tensile	Gas Bending	Net Gas Bending	Combined Tensile and Bending
Calculated stress, psi	43,000	31,200	14,900	57,900
0.2% yield point stress, psi (AMS 5613 stainless steel)	101,500	101,500	101,500	101,500

The results of blade vibration calculations are presented in figure 48 in terms of vibration frequency as a function of rotor speed. The rotor disk and blades were treated as a combined unit for these calculations. Included in figure 48 are curves of rotor frequency factor, E = rpm/60. Initial values of blade vibration frequency, calculated for unshrouded rotor blades, indicated a first bending vibration mode that was very close to twice the rotor frequency (2E) over the rotor speed operating range. This condition is considered operationally unsafe because of possible 2E excitation sources. With the addition of a shroud at 40% span from the tip, the blade vibration frequency was increased to a level of approximately 350 to 400 cps, which corresponds to rotor frequency

factors of 3.5 to 7E at the maximum and minimum rotor operating speeds, respectively. Because the probability of encountering detrimental excitation frequencies is relatively low at rotor frequency factors of 3E and above, it was decided to incorporate 40% span shrouds in the rotor blade design. The calculated vibration frequencies for combined bending and torsion modes are at a high E-factor level and no problems are anticipated with these modes.

Values of reduced velocity parameter, $K \sim (V_1'/c\omega)$ and incidence correlation parameter, $f(\beta_1')$, were calculated for rotor speeds of 70 and 100% of design speed. These values are compared in figure 49 with flutter data acquired from engine and component testing of circular arc airfoils. The position of the two calculated points with respect to the experimentally established flutter region for similar blading indicates no apparent blade flutter problem.

Stator A

The stator having a fixed-position forward section and rear section flap is shown in figure 50. Machined platforms at the end of each vane forward section are mechanically fastened to the stator inner and outer shrouds. The inner wall platform contains a drilled hole for the flap section pivot pin. The outer shroud contains the hole for the flap outer wall pivot pin. This arrangement permits precise radial alignment of the pivot pins during the initial assembly. The flap section is spring loaded at the inner wall pivot pin. A Teflon washer is provided at the flap outer wall pivot pin joint to minimize air leakage and friction. The flap actuation ring is fastened to flap actuation levers through spherical ball joints. The spring and spherical joint are incorporated in the design to eliminate linkage backlash.

The actuation levers are attached to the flap outer wall pin by means of self-locking taper joints, which permit precise vane alignments.

The calculated airfoil bending and shear stresses were approximately 10,000 and 150 psi, respectively. The maximum calculated vane spindle attachment stress was 18,500 psi.

The calculated first bending and torsion vibration frequencies were 545 cps and approximately 2200 cps, respectively. These frequencies do not correspond to any significant sources of excitation.

Stator B

The double-flap stator is shown in figure 51. The flap outer wall pivot pins are supported in a single piece outer shroud and split inner shroud to facilitate assembly. Eccentric bushings are provided for both flap inner wall pins and for the forward flap outer wall pin to permit proper relative positioning of the two flap sections during initial assembly. The flap inner wall pins are spring loaded, and the flap outer wall pin shoulders rotate on Teflon washers. The outer wall pin ends are tapered for self-locking attachment to the flap actuation levers. The forward and rear flap sections have independent actuation mechanisms. The actuation ring and lever for the rear flap section are those used for the slotted, single-flap stator configuration.

Stress calculations for the double-flap stator configuration resulted in the same magnitudes of airfoil bending and pin shear stresses as those calculated for the single-flap stator.

First bending frequencies calculated for the forward and rear flap sections were 200 and 285 cps, respectively. Although 200 cps corresponds to 2E (2 times the rotor frequency) at design speed, this condition is less consequential for the stator than for the rotor, and vibration problems are not expected. The rear flap first bending frequency and the first torsion frequencies for both flap sections do not indicate any vibration problems.

Compressor Test Rig

The Pratt & Whitney Aircraft (FRDC) compressor research test rig, available for the experimental evaluation of variable geometry guide vanes and stators, was designed to simulate the aerodynamic environment of the front stage of a state-of-the-art compressor. Figure 52 shows a sectional view of the test rig. The test rig comprises a bellmouth inlet section, guide vane, rotor, and stator case sections, and an exhaust diffuser system. The exhaust system is designed with a series of radial flow vanes for overboard dumping of part of the airflow to accommodate flowrates up to 330 lb/sec using the existing compressor test stand exhaust system. The flowrate is controlled by means of 24 motor-driven throttle vanes located upstream of the overboard dump section.

The rotor assembly is supported by a forward (roller) bearing that provides radial support and a rear (ball) bearing that provides both radial and axial support. Front bearing radial loads are transmitted to the outer case by means of stationary leading edge sections of the inlet guide vanes. These sections contain bearing oil and instrumentation lead passages. Rear bearing radial and thrust loads are transmitted to the outer case by means of eight struts located downstream of the throttle valve.

Stiff and flexible bearing critical rotative speeds were calculated for the combined drive turbine and compressor shaft system with the following results:

Vibration Mode	Critical Speed, rpm
Stiff Bearing	
First Bending	10,000
Flexible Bearing	
First Bending	7,000
Bounce	5,900
Tilt	6,400

Although the calculated bounce and tilt vibration modes are nearly equal to the 90 and 110% design rotor speed operating conditions, respectively, no vibration problems are expected because of the relatively low amplitude of these vibrations. To substantiate this conclusion, an 0.8 hub/tip ratio compressor research rig was operated over a narrow range of speeds that encompassed the calculated bounce mode frequency for the rig, and only a 0.0005-in. (double amplitude) increase in rig vibration amplitude was observed.

Compressor Test Facility

The compressor test facility is shown in figure 53. Primary components of the facility are a J75 slave engine, a two-stage exhaust ejector system, a turbine drive system, and an ASME standard inlet duct. The J75 engine supplies exhaust gases to the turbine to drive the compressor or to the exhaust ejectors for operation in a nonrotating mode. The turbine drive system is rated at 7000 maximum horsepower at 8500 rpm. The two-stage exhaust ejector system can maintain over 100 lb/sec airflow through the compressor test rig when rotating stages are not installed and the turbine drive system is disengaged.

Air enters the compressor test section through a 78-ft inlet duct, a plenum chamber, and a bellmouth inlet, and exhausts either directly to the atmosphere or through the two-stage ejector system. The airflow rate is measured in the inlet duct using a thin plate orifice. The inlet duct and plenum chamber are mounted on a track and can be rolled away from the compressor rig to facilitate test configuration and instrumentation changes.

REFERENCES

1. "Single Stage Experimental Evaluation of Variable-Geometry Guide Vanes and Stators, Part II - Annular Cascade Investigations of Candidate Variable Geometry Designs," NASA CR-54555, PWA FR-2297, 14 July 1967.

2. Steinke, Ronald J. and James E. Crouse, "Preliminary Analysis of the Effectiveness of Variable-Geometry Guide Vanes to Control Rotor-Inlet Flow Conditions," NASA TN D-3823, January 1967.

3. Dunavant, James C., "Cascade Investigation of a Related Series of 6-Percent-Thick Guide-Vane Profiles and Design Charts," NACA TN-3959, May 1957.

4. "Single Stage Experimental Evaluation of Slotted Rotor and Stator Blading, Part I, Analysis and Design," NASA CR-54544, PWA FR-1713, July 1966.

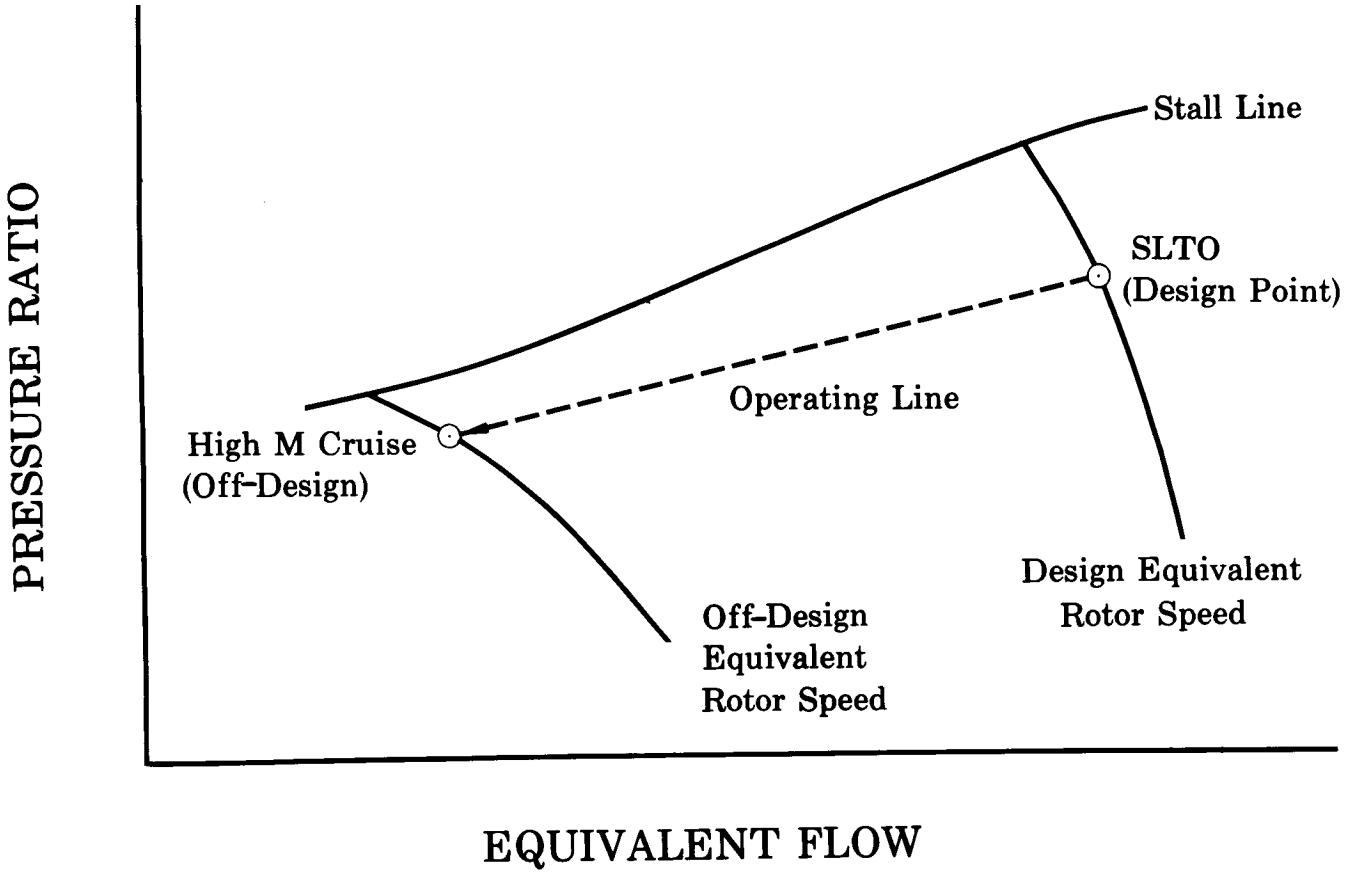

Figure 1. Typical Compressor Map for High Mach No. Cruise Aircraft

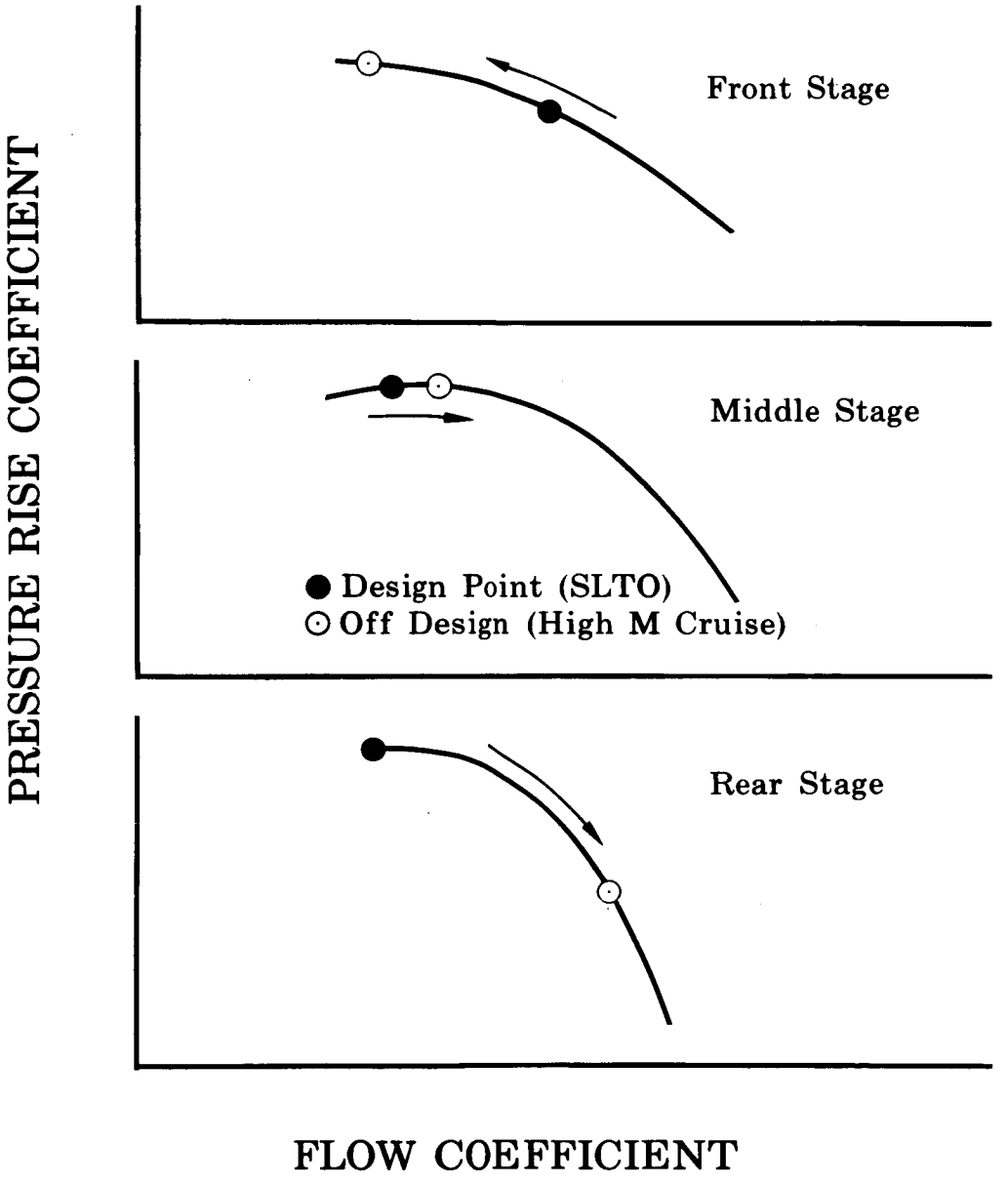

Figure 2. Typical Migration of Stage Operating Points Between SLTO and Cruise

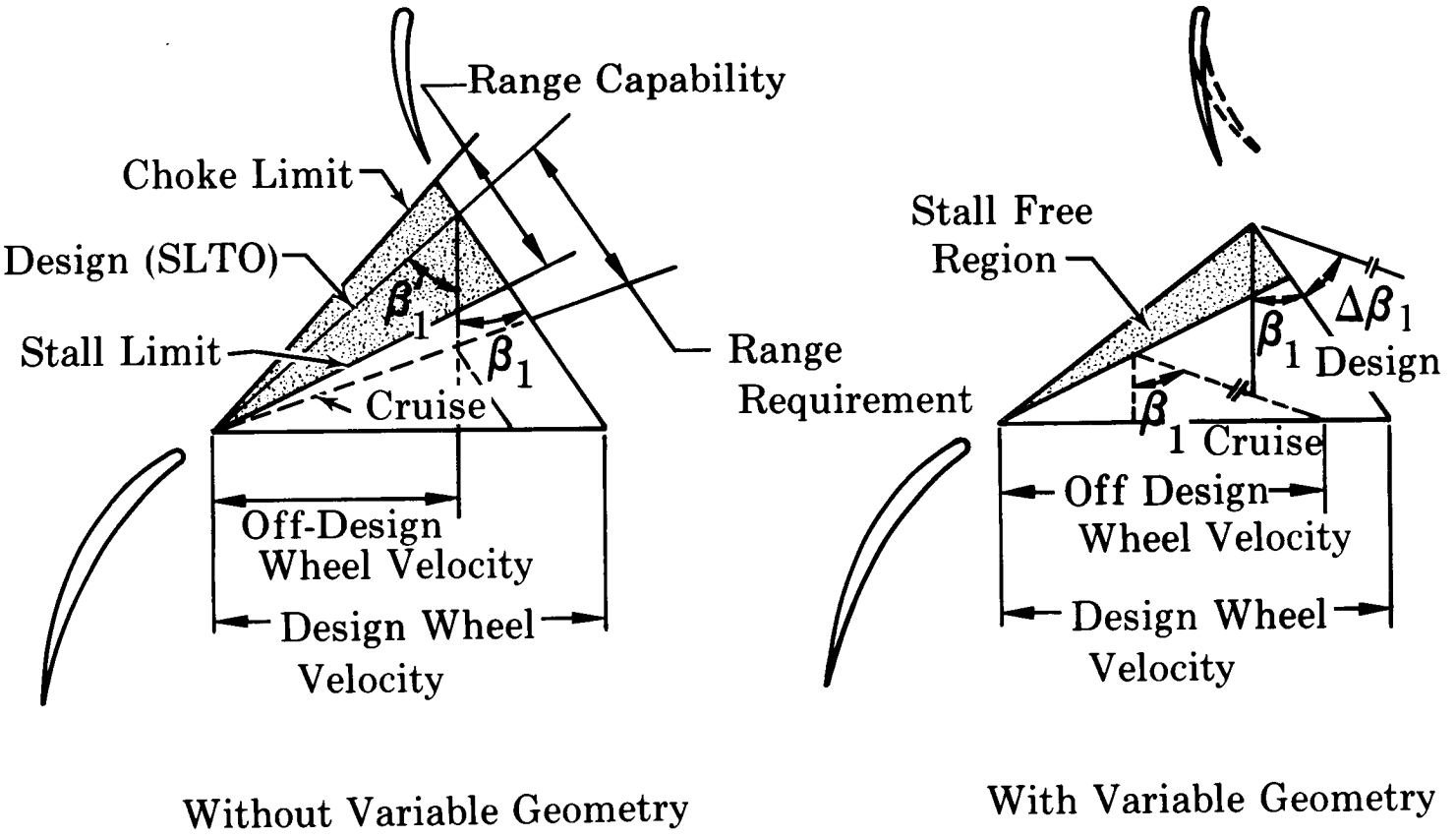

Figure 3. Rotor Blade Element Vector Diagram

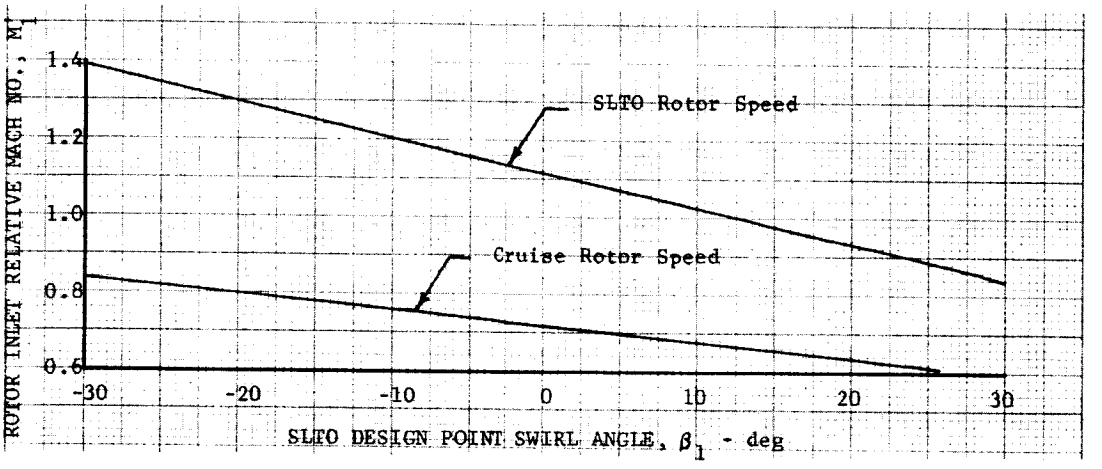

Figure 4b. Meanline Variation of Rotor Inlet Relative Mach Number With Design Point Guide Vane Exit Air Angle

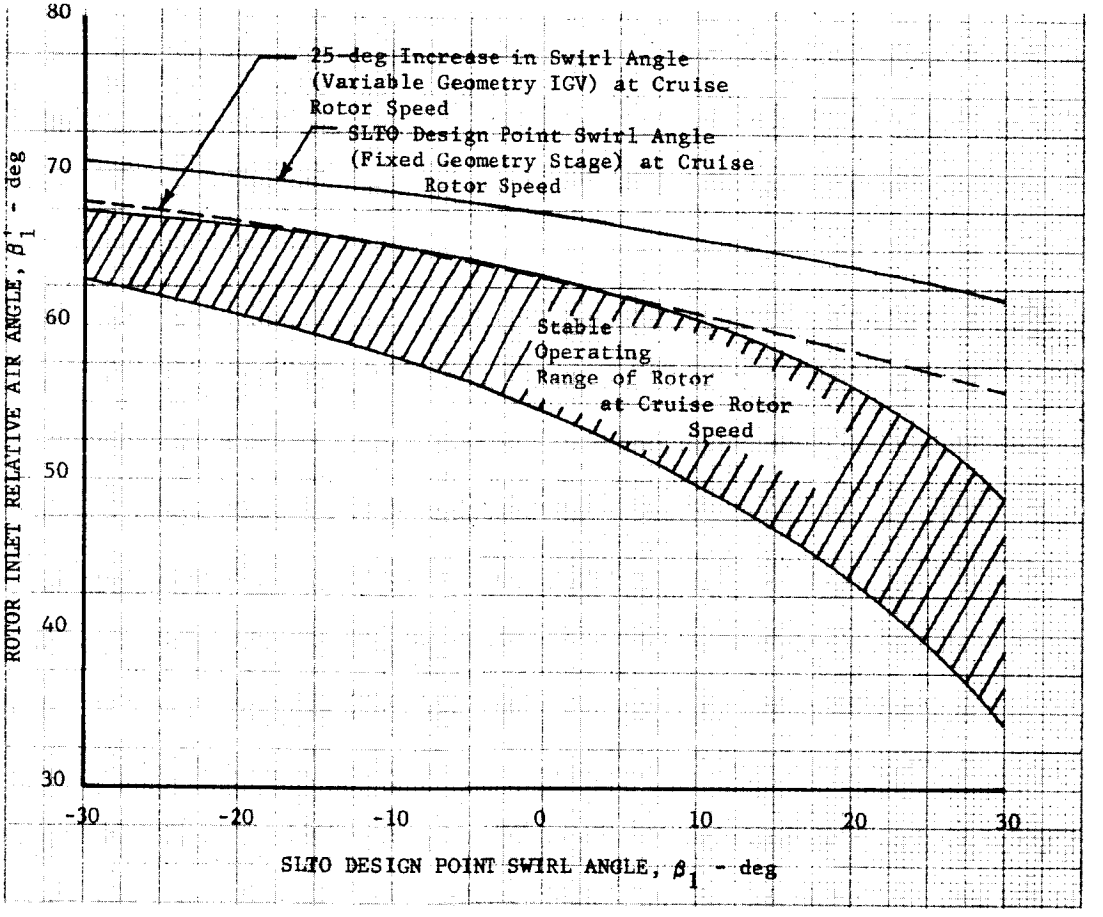

Figure 4a. Meanline Variation of Rotor Inlet Relative Air Angle With Design Point Guide Vane Exit Air Angle

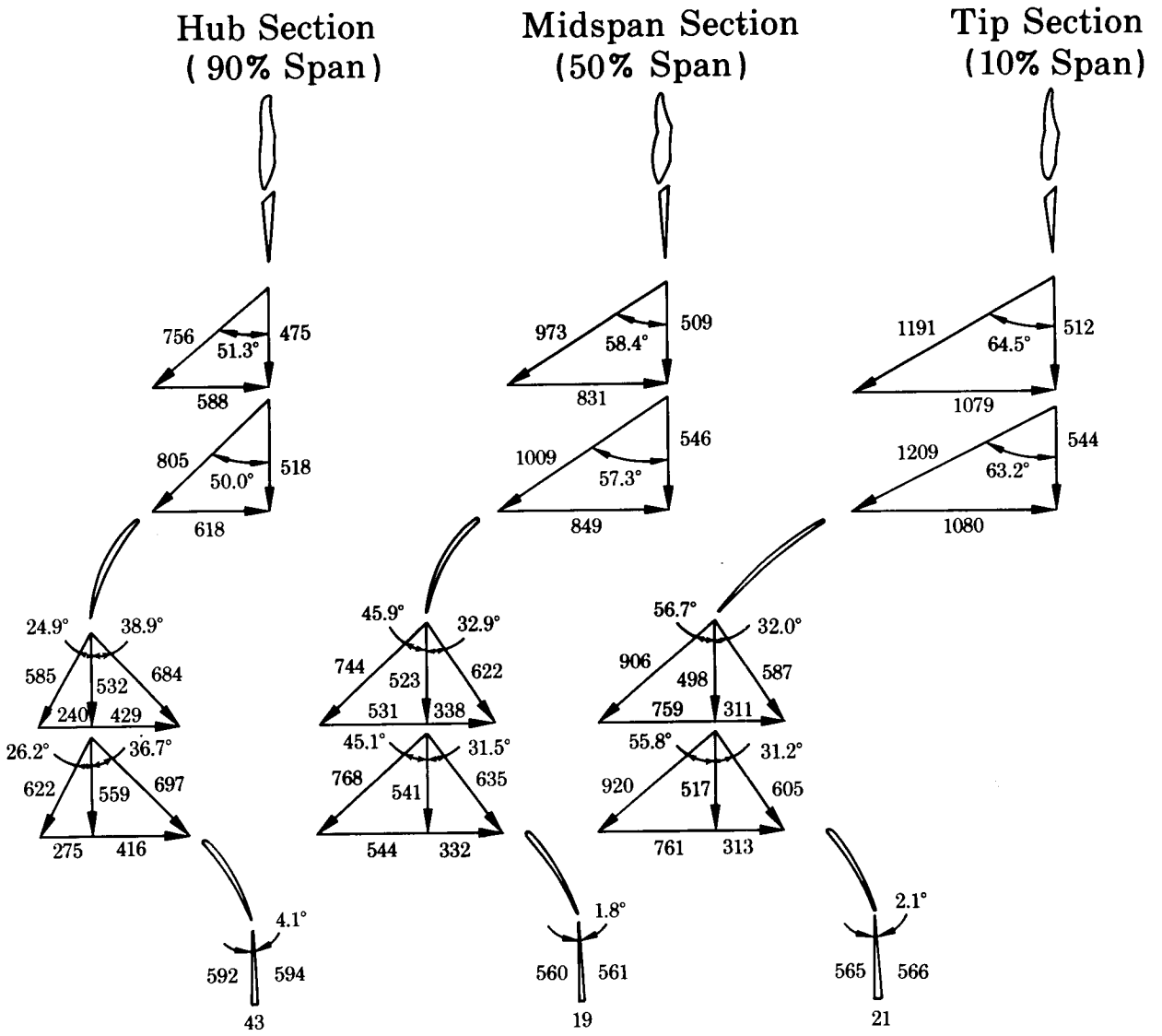

Figure 5. Design Point Vector Diagrams

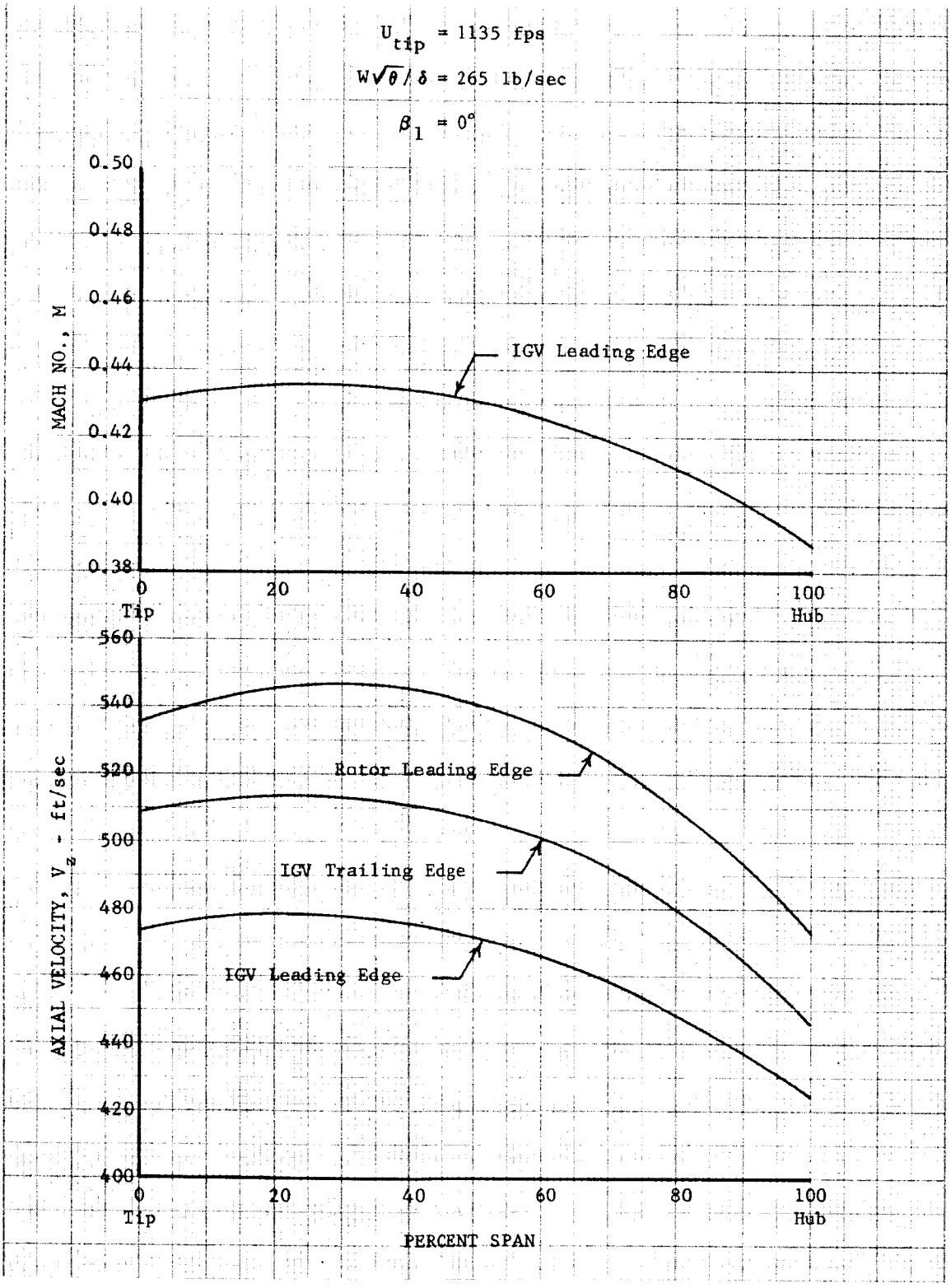

Figure 6. Design Point Radial Distributions of Inlet Mach No. and Axial Velocity

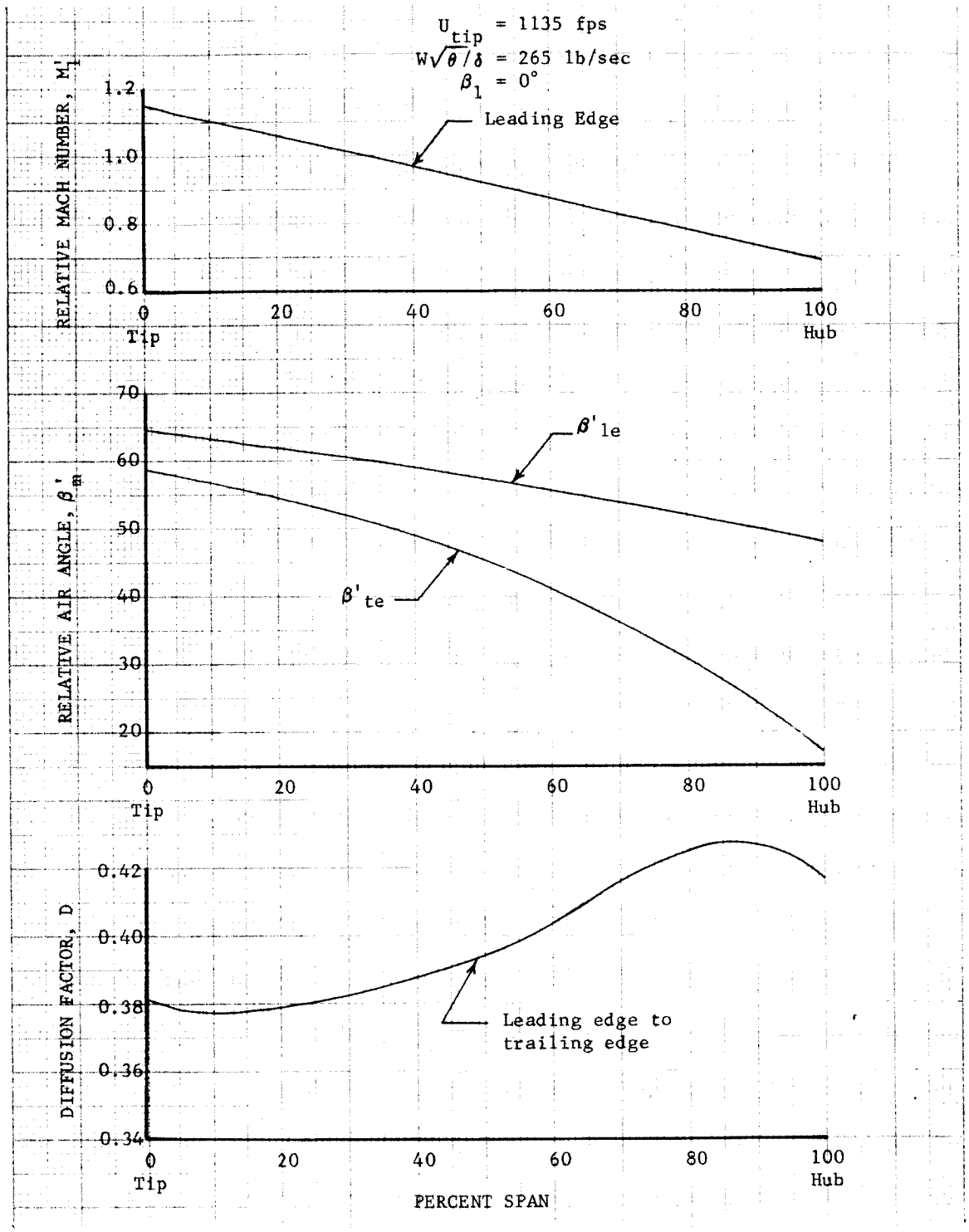

Figure 7. Design Point Radial Distribution of Rotor Inlet Relative Mach No., Inlet and Exit Relative Air Angle, and Diffusion Factor

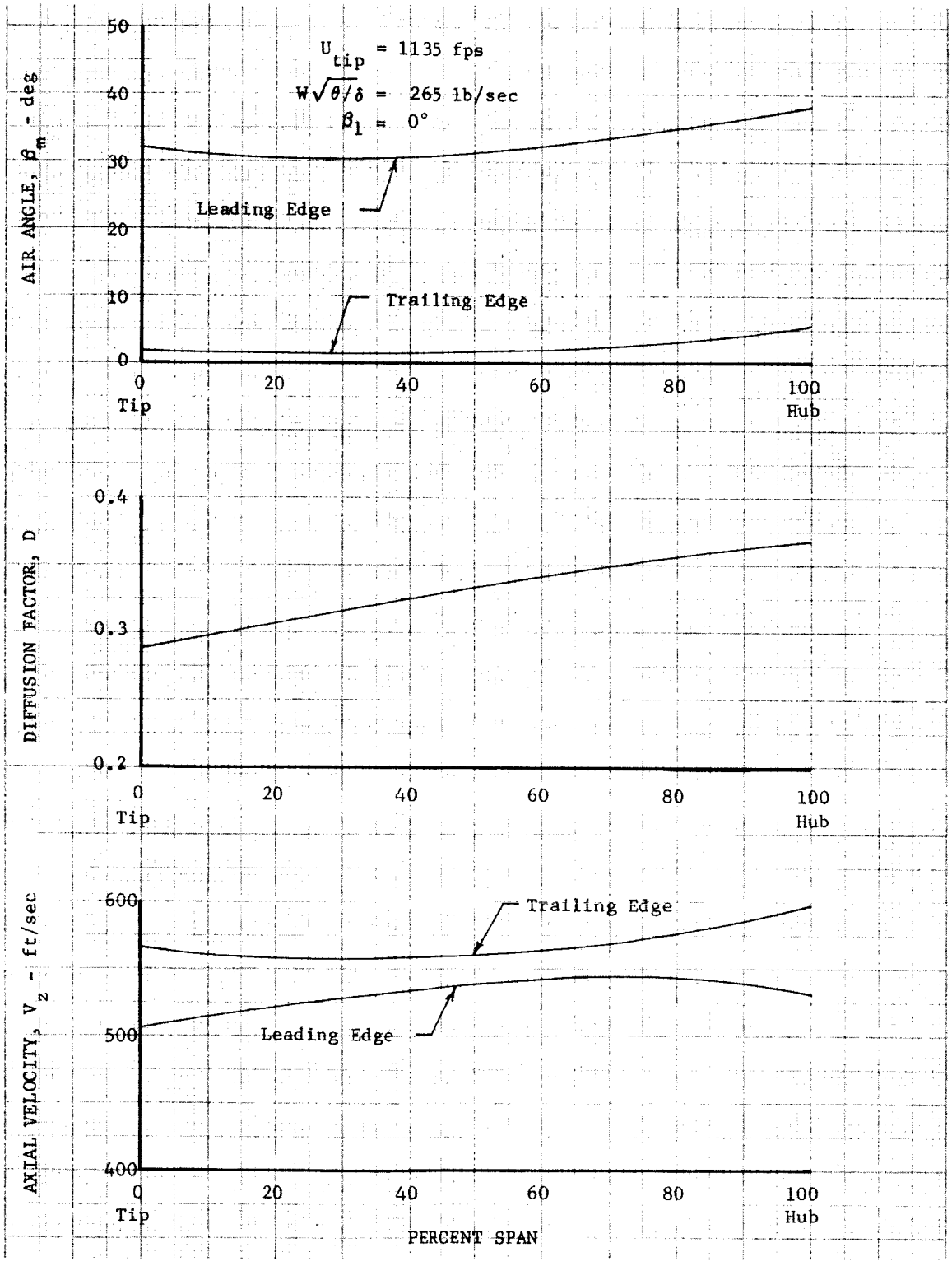

Figure 8. Design Point Radial Distribution of Stator Air Angle, Diffusion Factor, and Axial Velocity

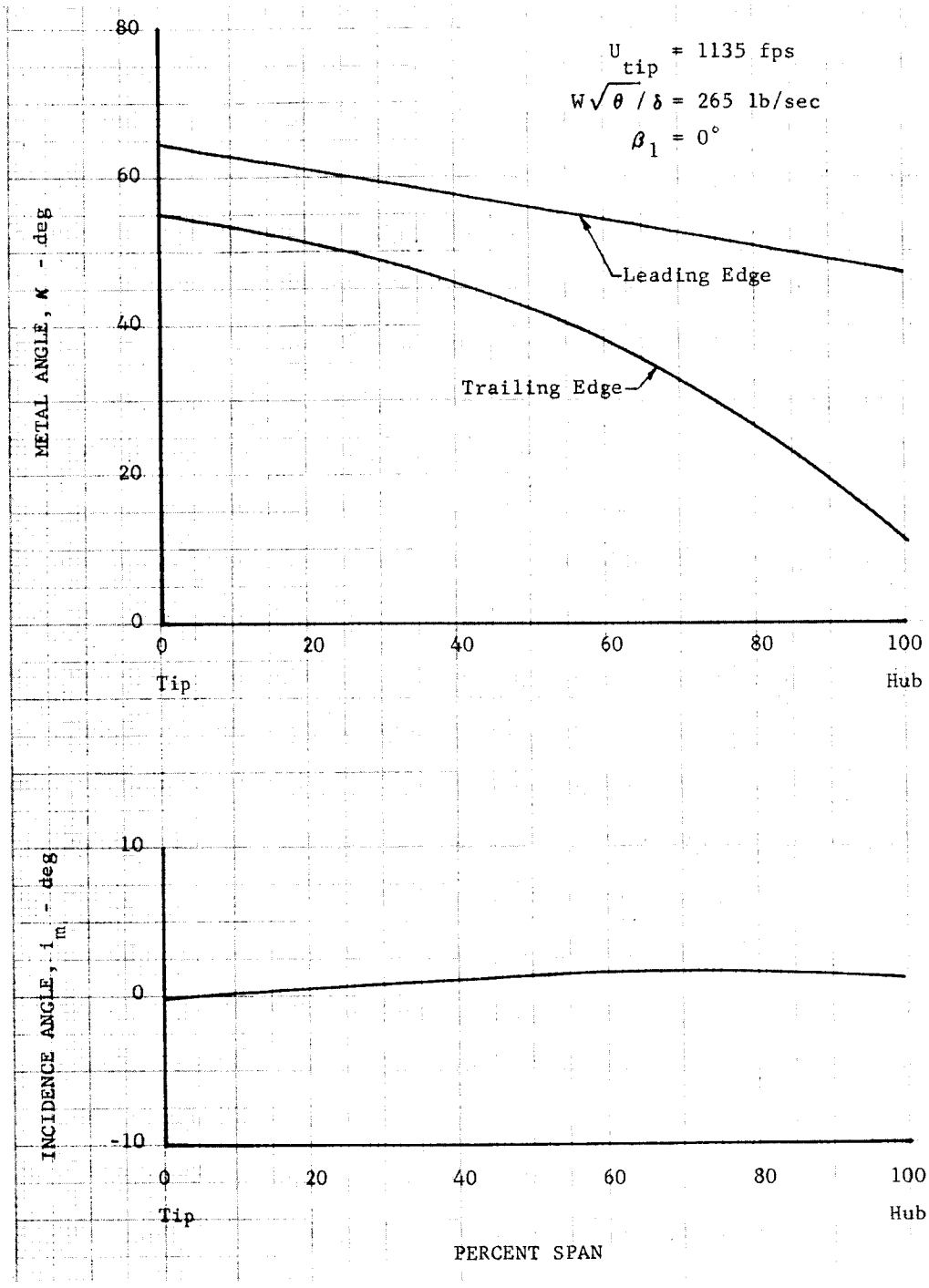

Figure 9. Design Point Radial Distribution of Rotor Metal and Incidence Angles

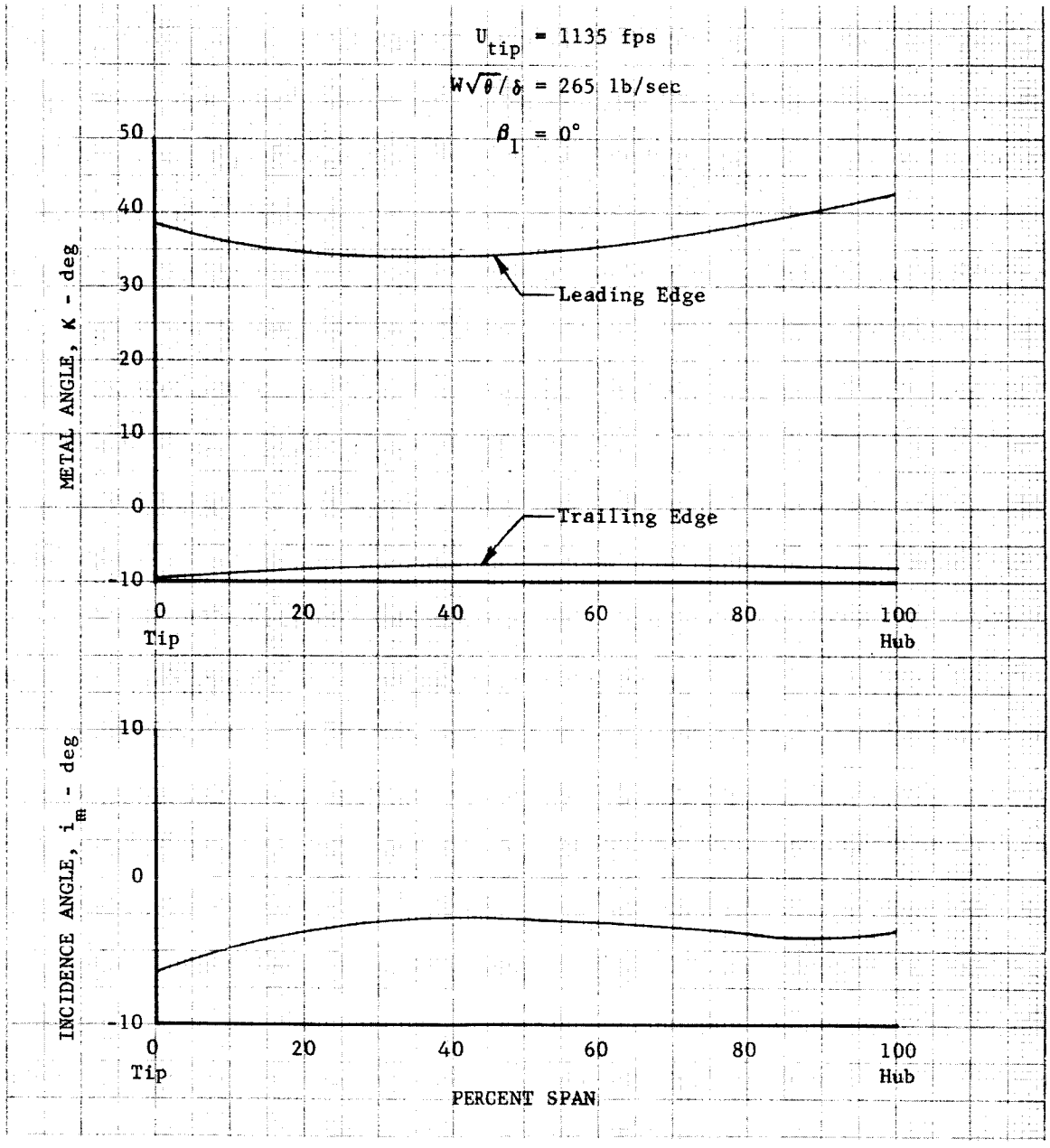

Figure 12. Design Point Radial Distribution of Stator Metal Angles and Incidence Angle

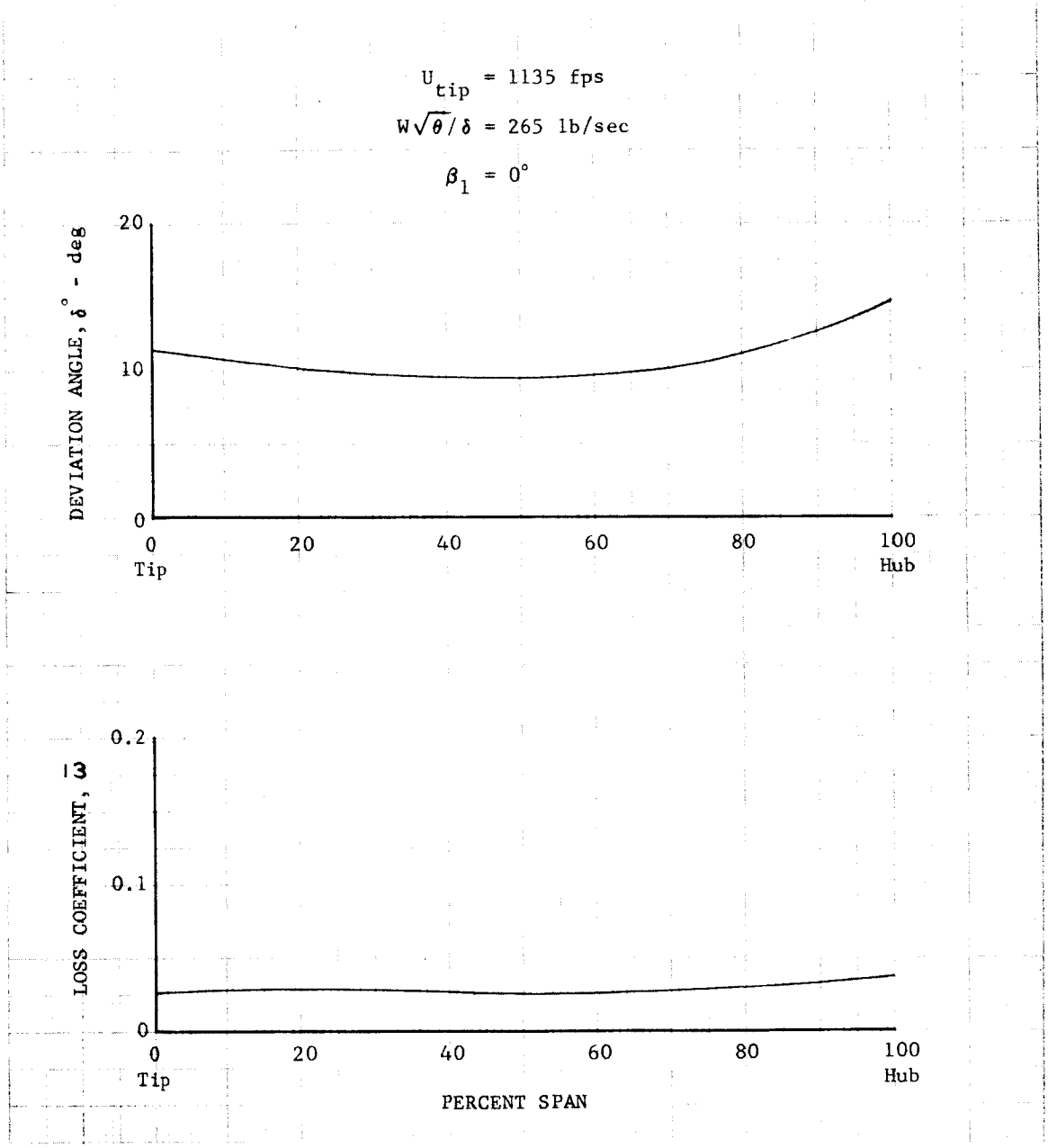

Figure 13. Design Point Radial Distribution of Stator Deviation Angle and Loss Coefficient

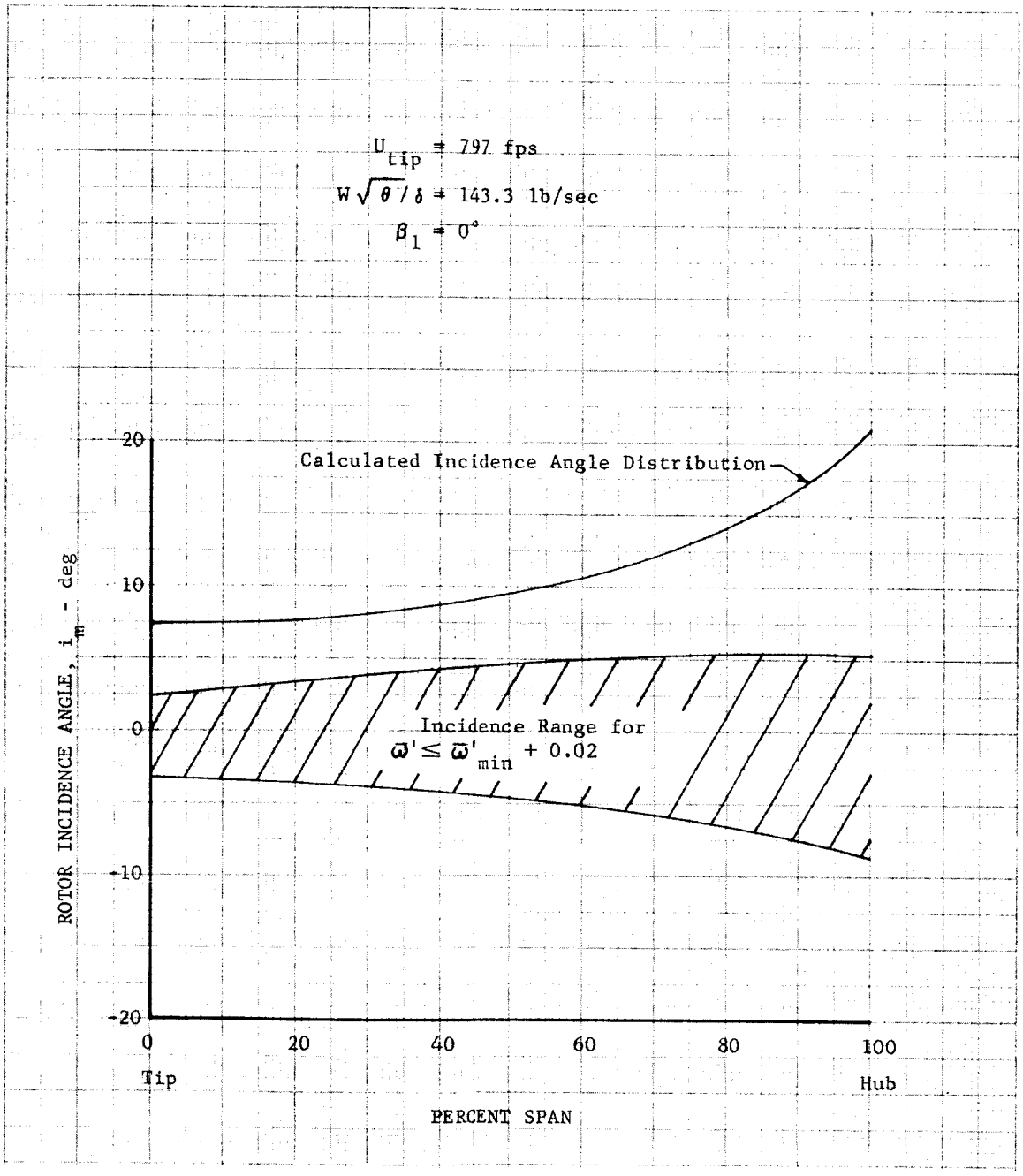

Figure 14. Radial Distribution of Rotor Incidence Angle for Design Point Geometry at Off-Design Operation

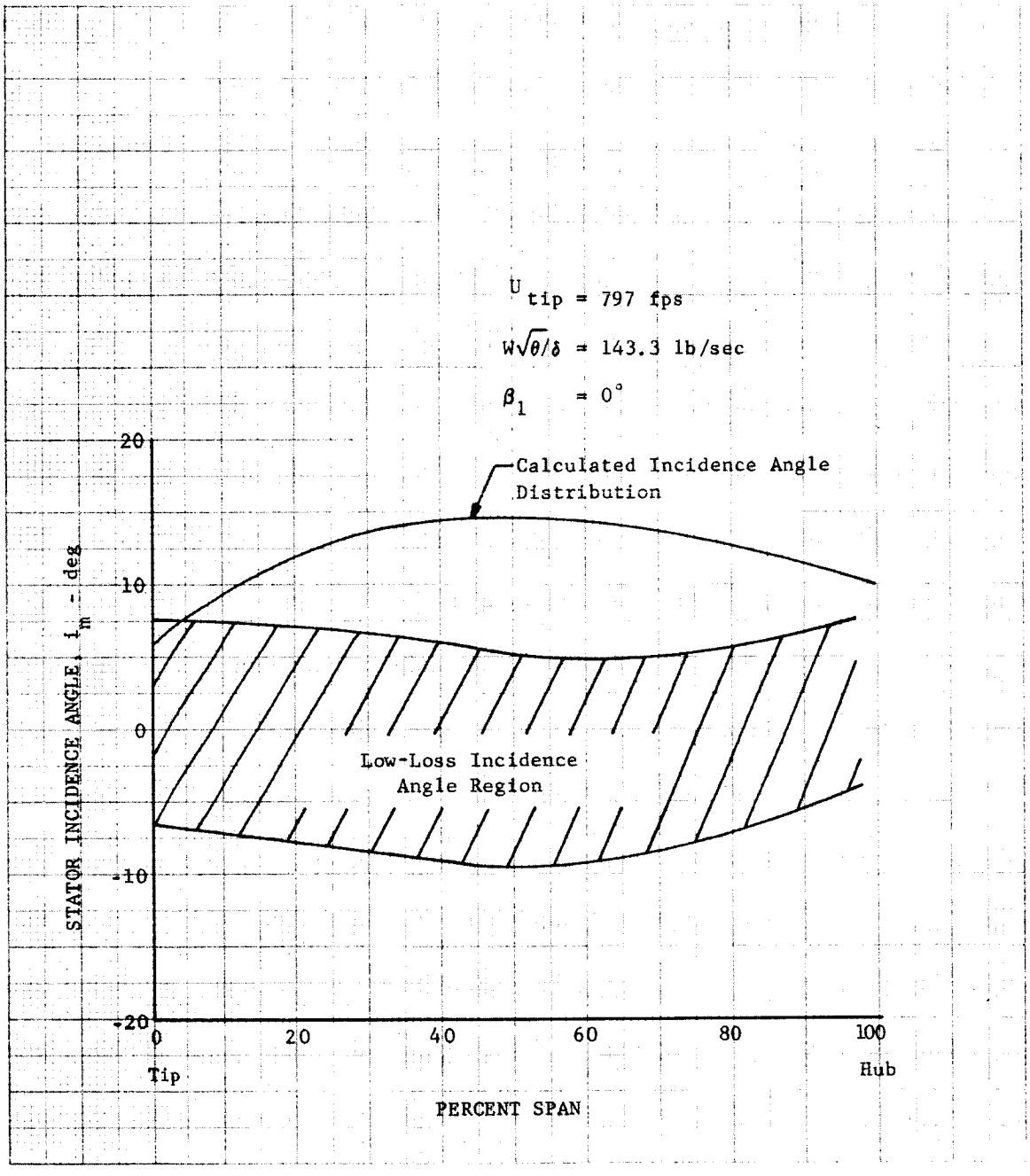

Figure 15. Radial Distribution of Stator Incidence Angle for Design Point Geometry at Off-Design Operation

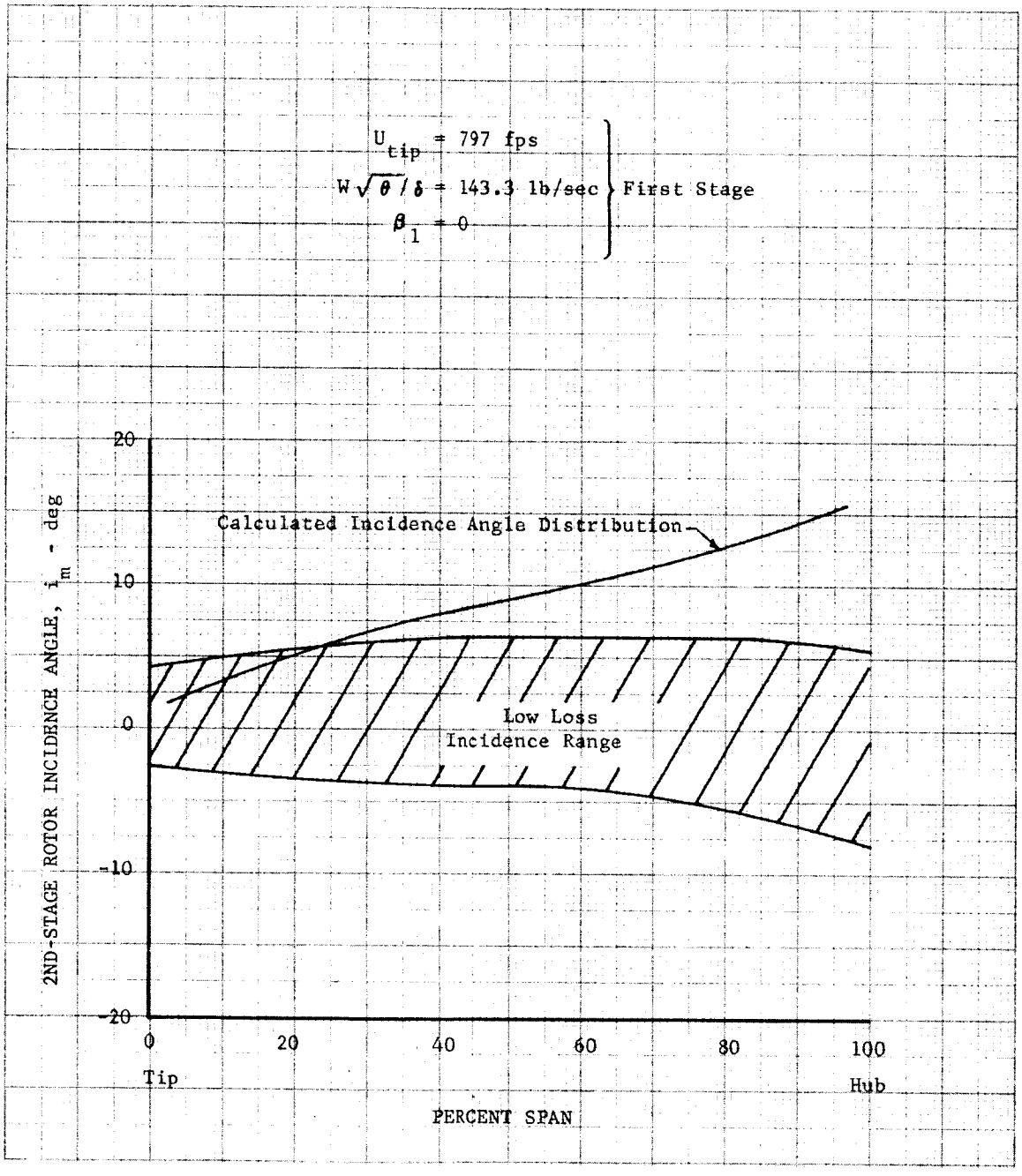

Figure 16. Radial Distribution of 2nd-Stage Rotor Incidence Angle at Off-Design, Behind Design Point Geometry First Stage

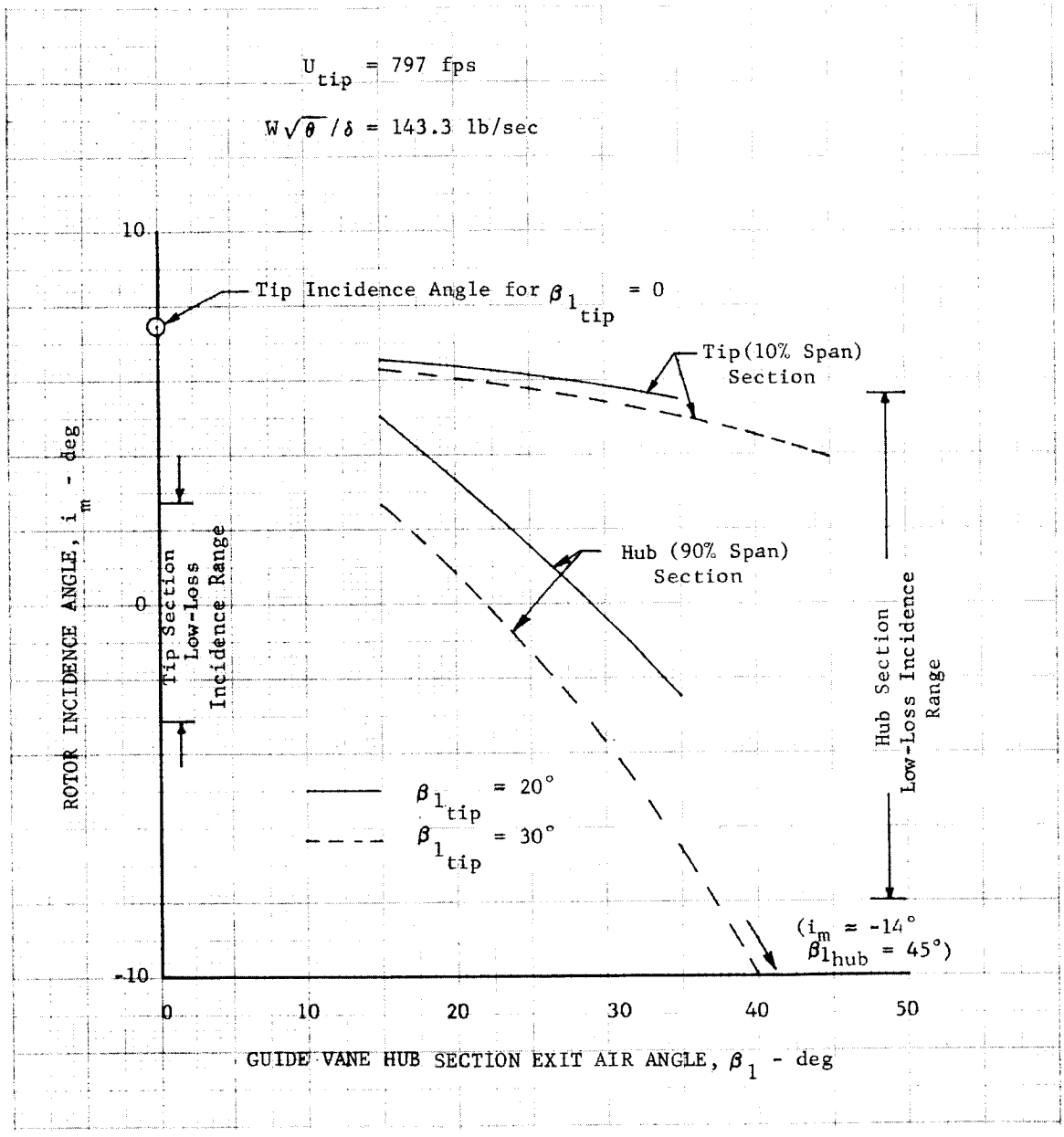

Figure 17. Effect of Guide Vane Swirl Distribution on Rotor Incidence

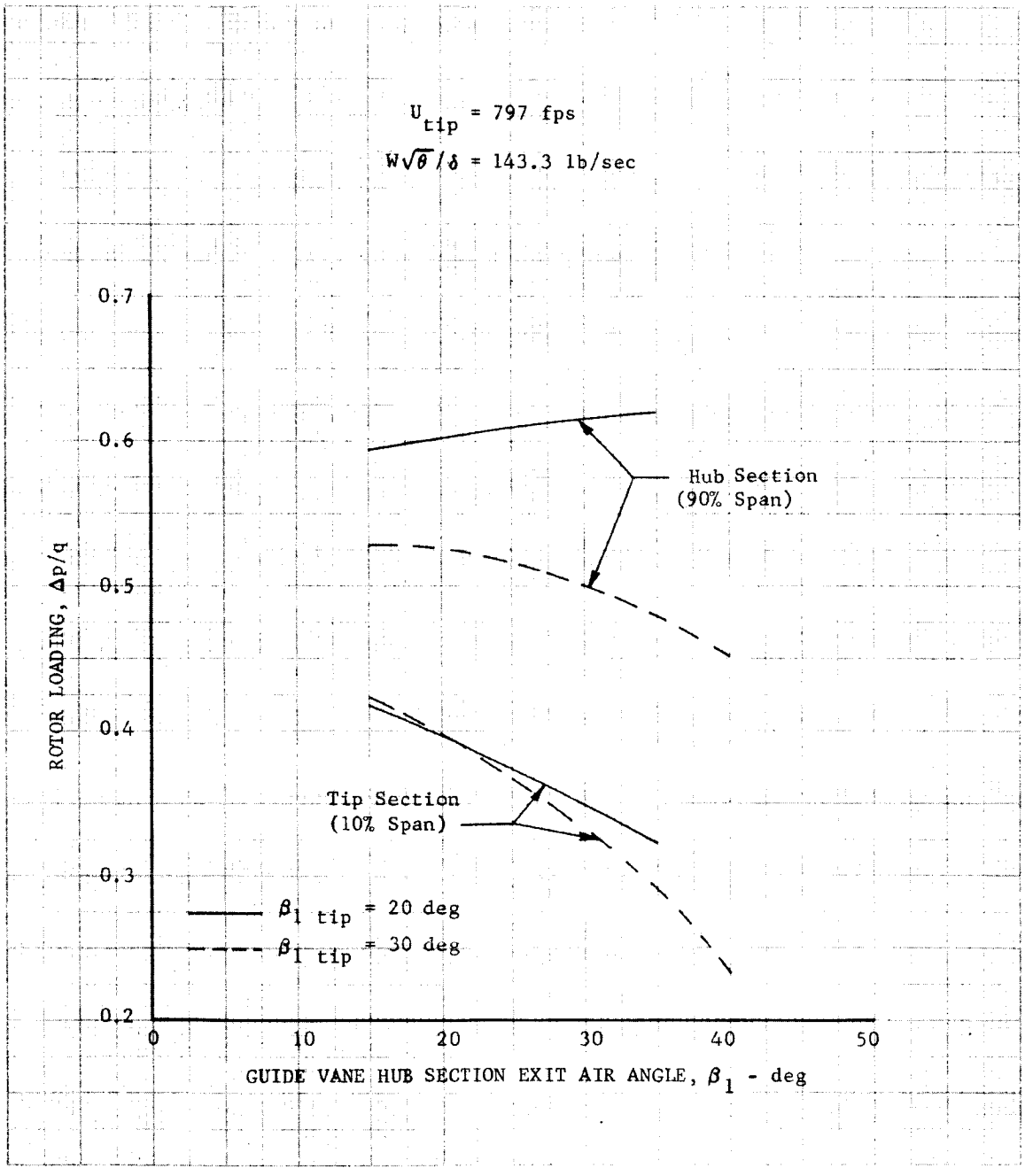

Figure 18. Effect of Guide Vane Swirl Distribution on Rotor Loading

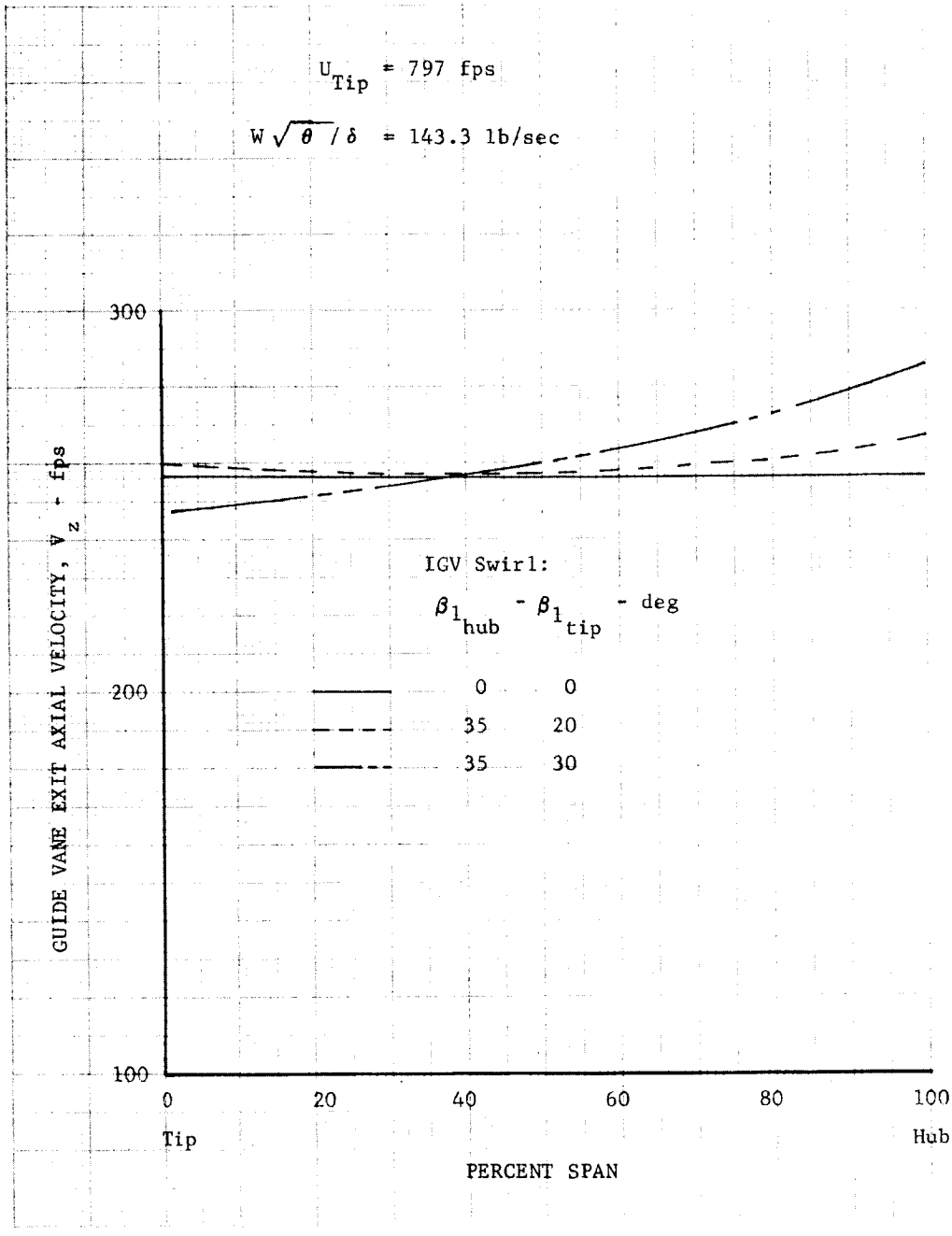

Figure 19. Effect of Guide Vane Swirl Distribution on Axial Velocity Distribution

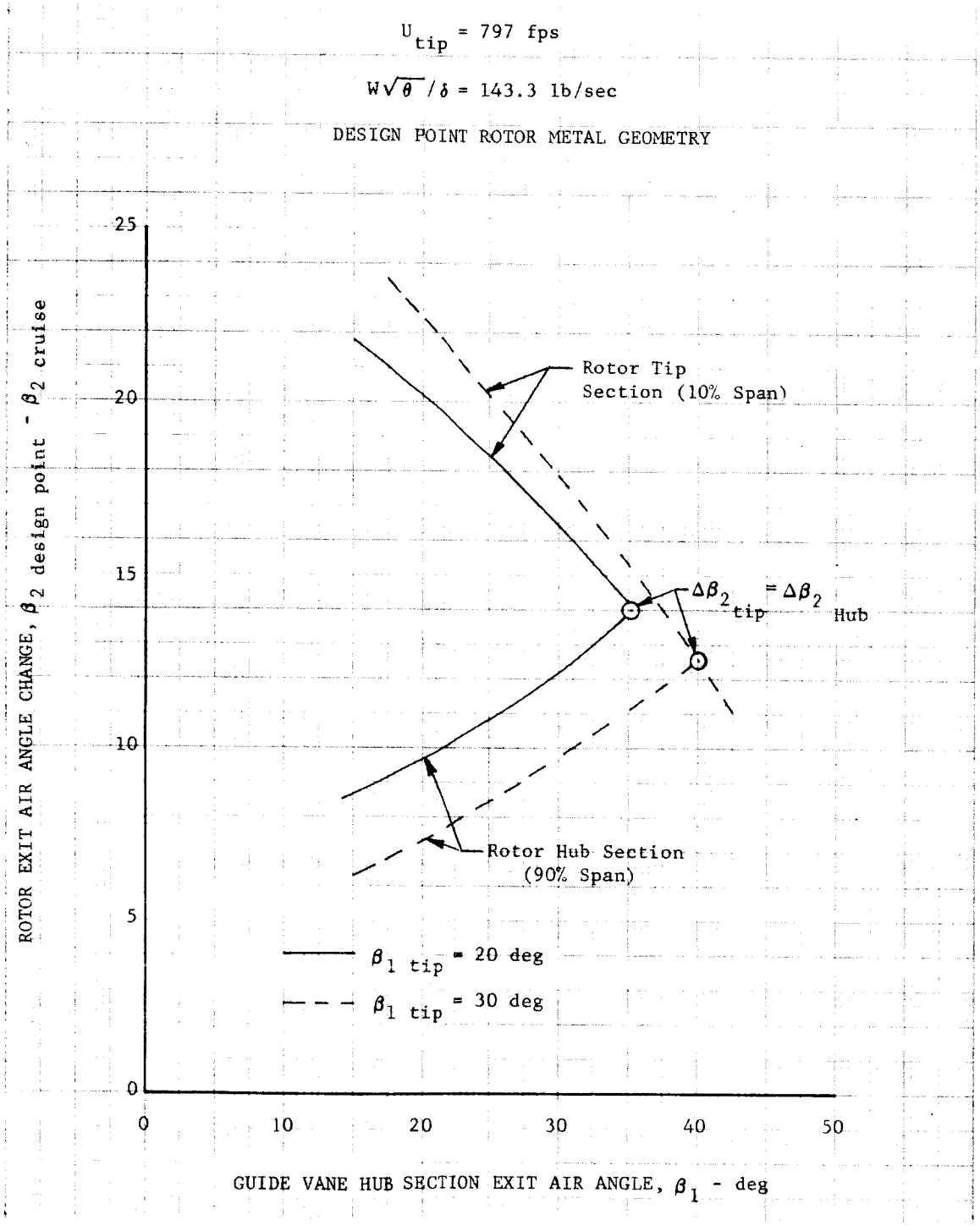

Figure 20. Rotor Exit Absolute Air Angle Change (Design Point to Cruise) vs Guide Vane Hub Section Exit Air Angle

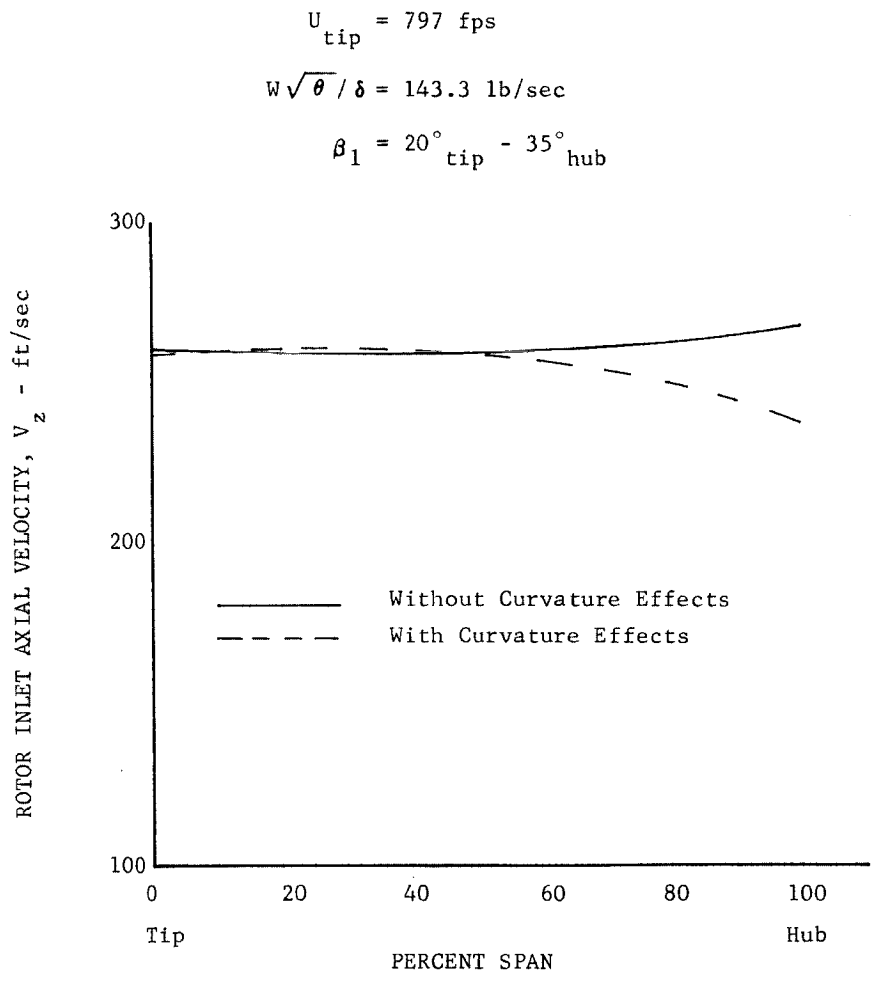

Figure 21. Effect of Wall Curvature on Rotor Inlet Axial Velocity Distribution

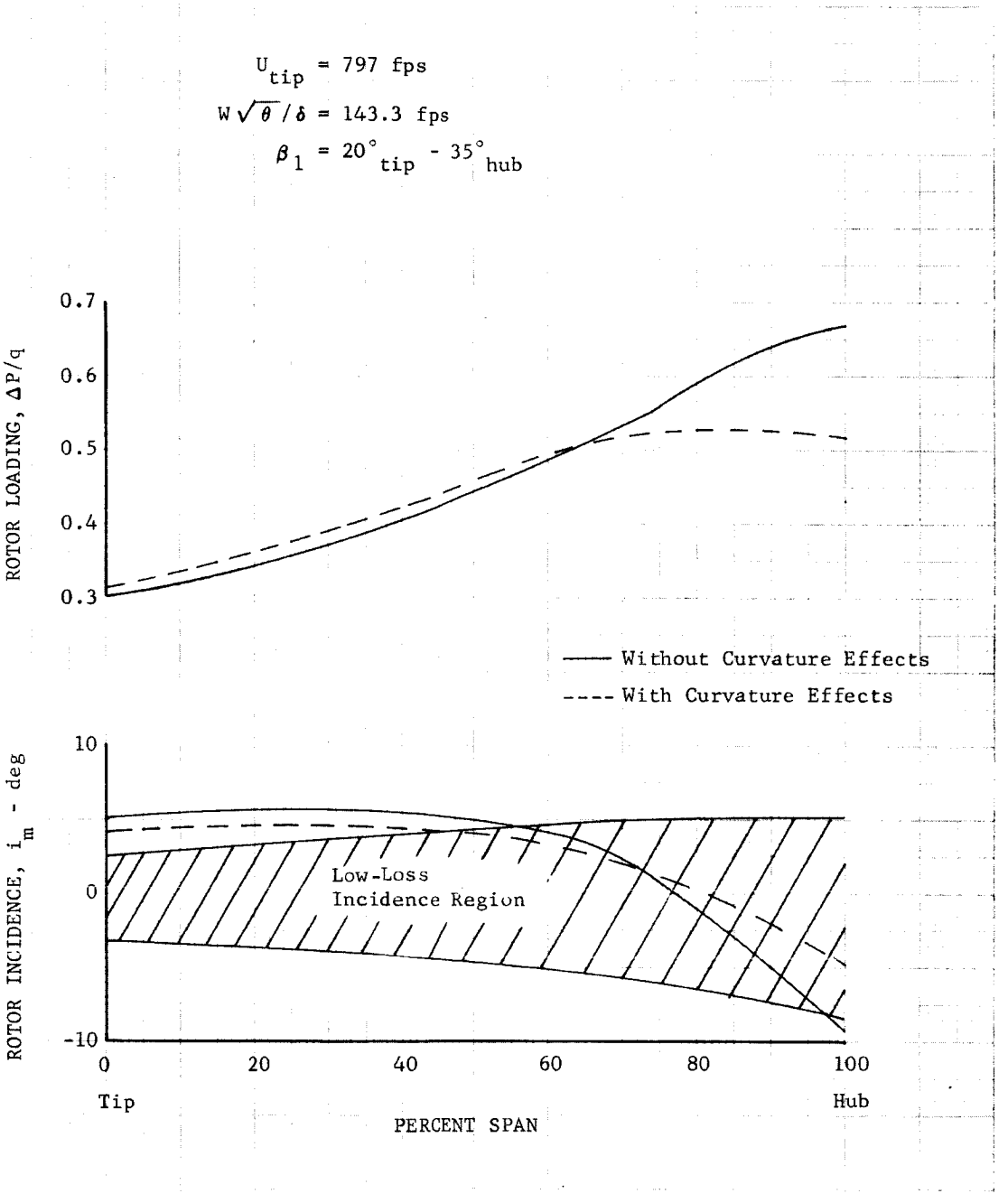

Figure 22. Effect of Wall Curvature on Rotor Incidence Angle and Loading Distributions

U_{tip} = 797 fps

$W\sqrt{\theta}/\delta$ = 143.3 lb/sec

$\beta_1 = 20^\circ_{tip} - 35^\circ_{hub}$

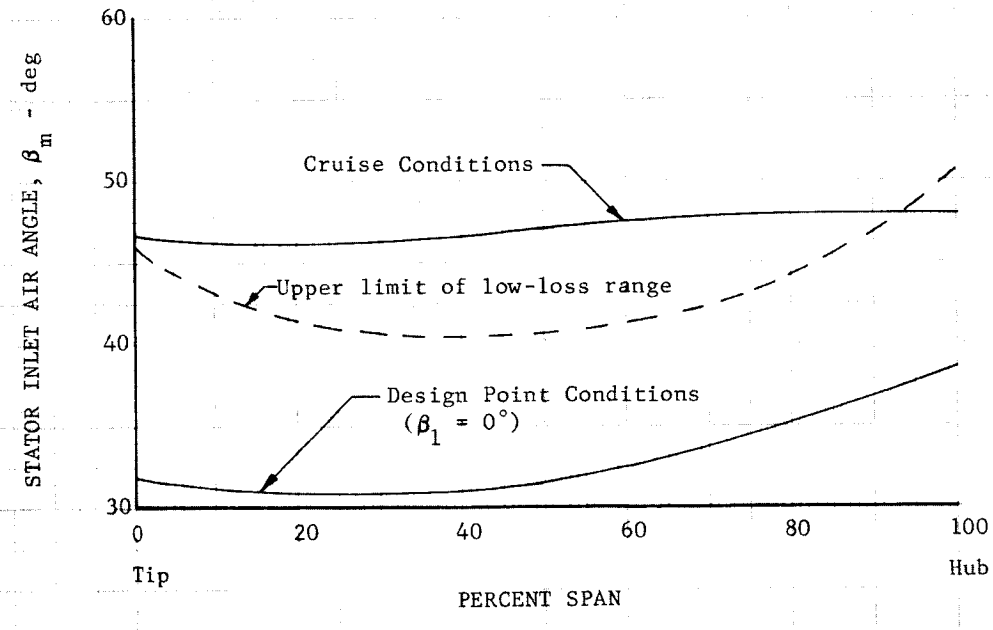

Figure 23. Radial Distribution of Stator Inlet Air Angle

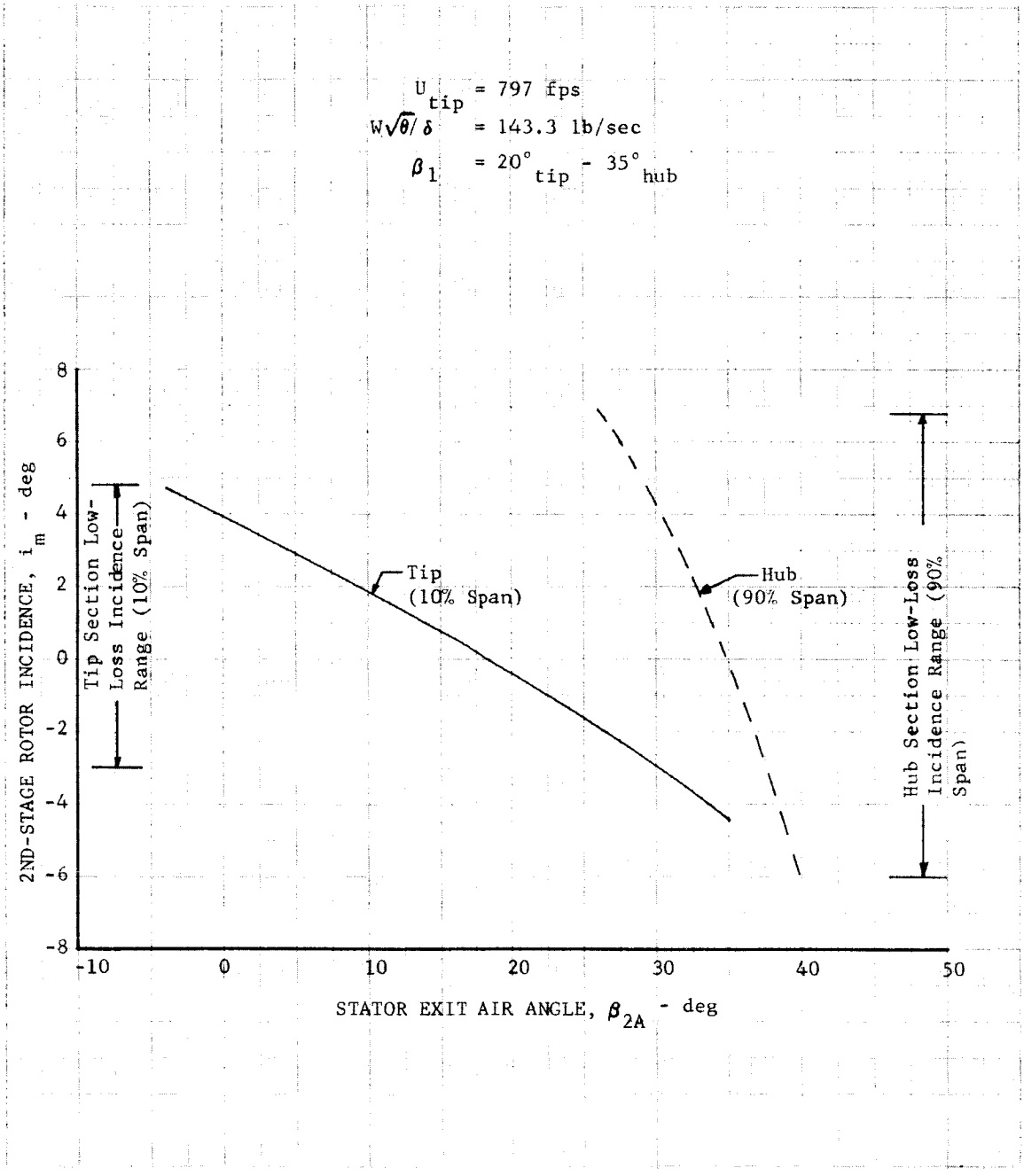

Figure 24. Effect of Stator Exit Air Angle on 2nd-Stage Rotor Incidence Angle

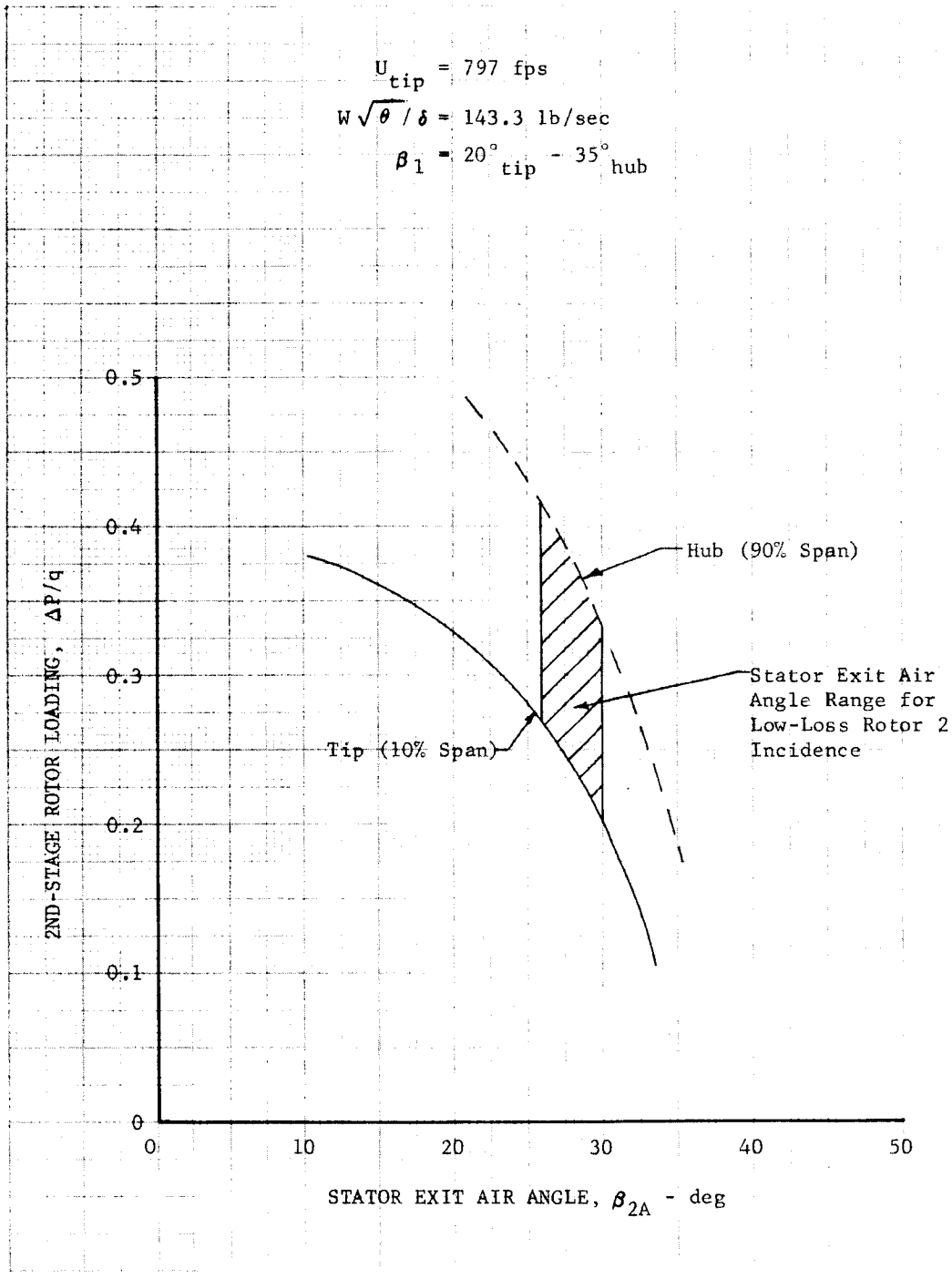

Figure 25. Effect of Stator Exit Air Angle on 2nd-Stage Rotor Loading

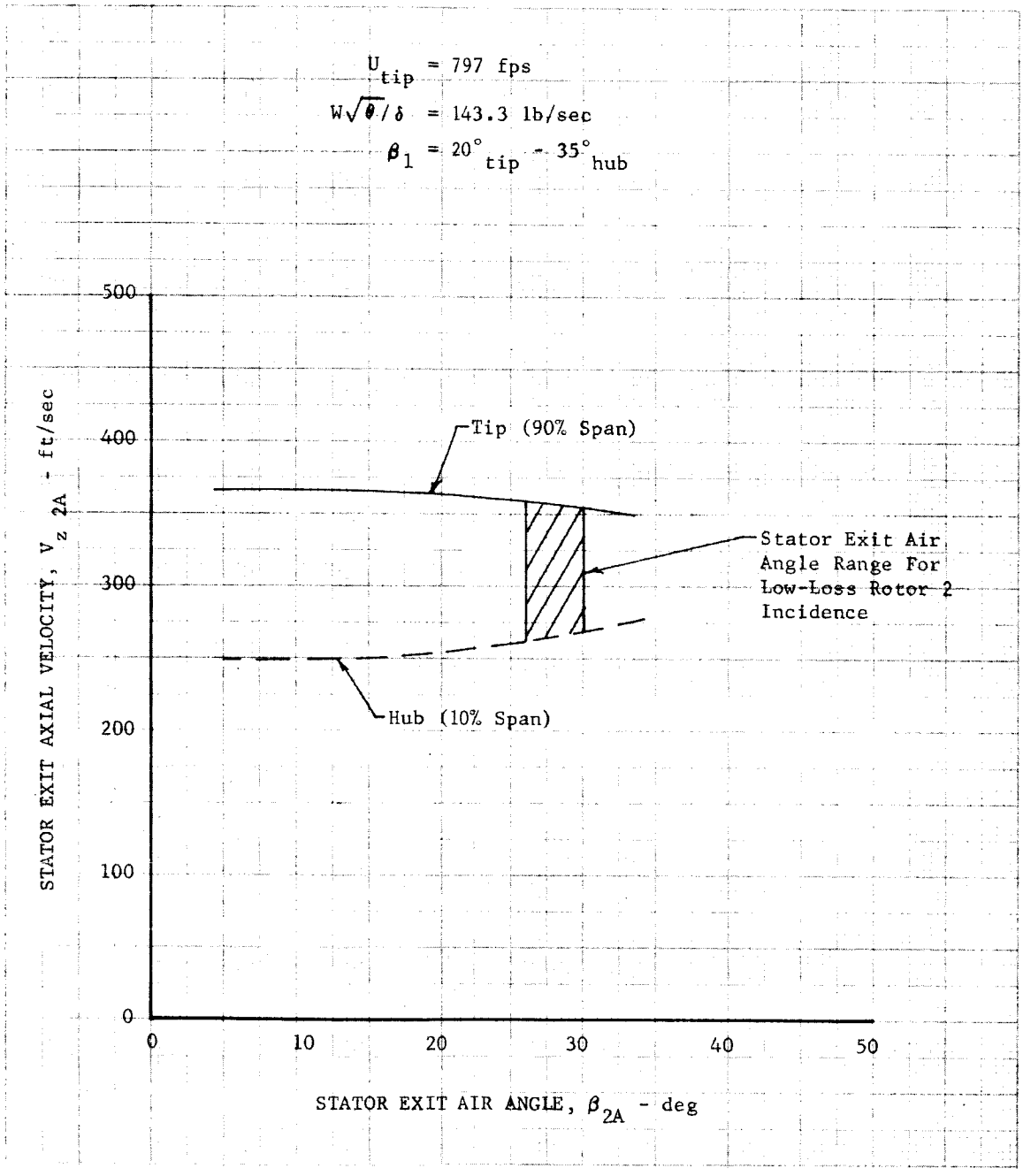

Figure 26. Effect of Stator Exit Air Angle on Stator Exit Axial Velocity

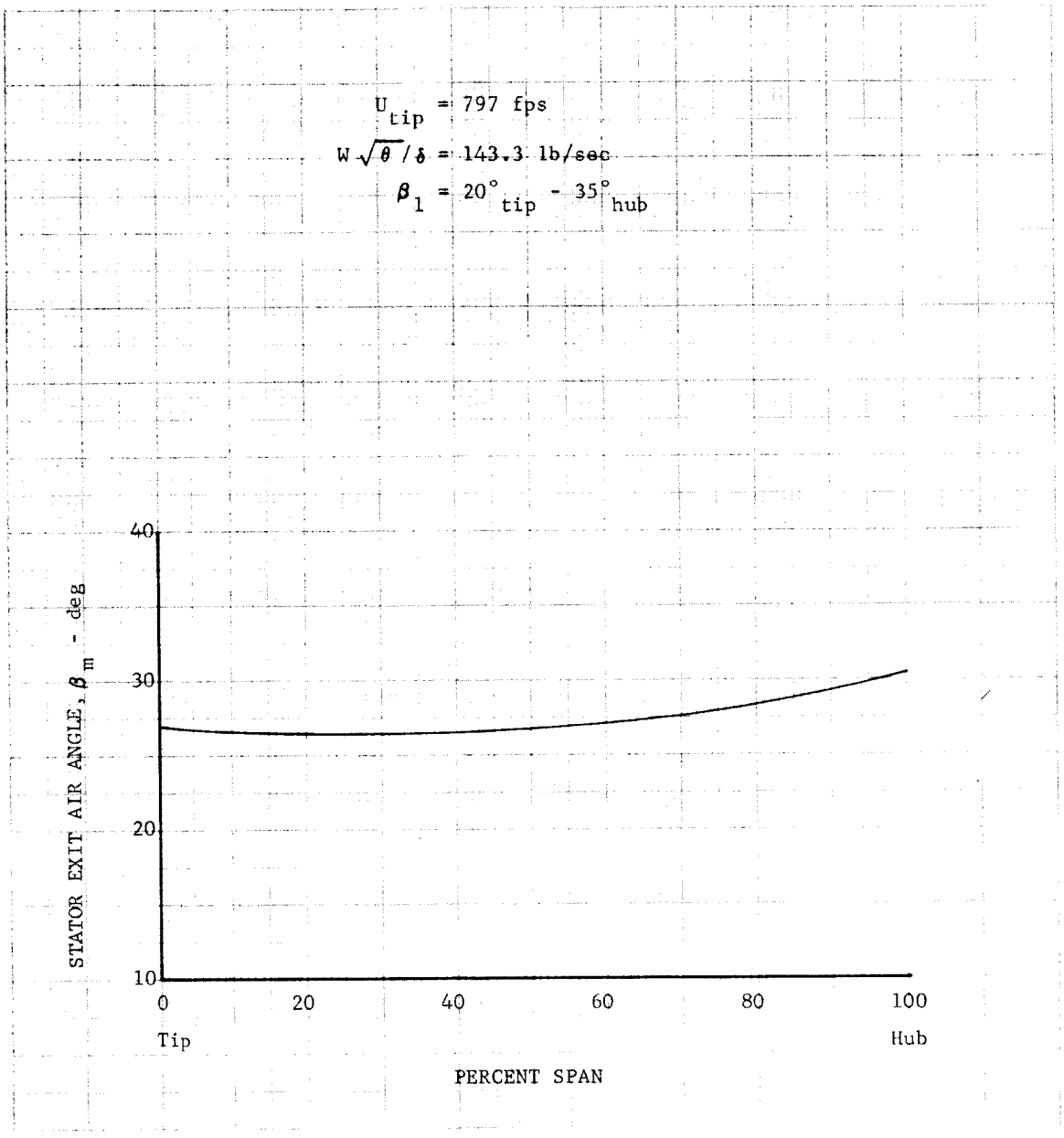

Figure 27. Radial Distribution of Stator Exit Air Angle at Off-Design Conditions

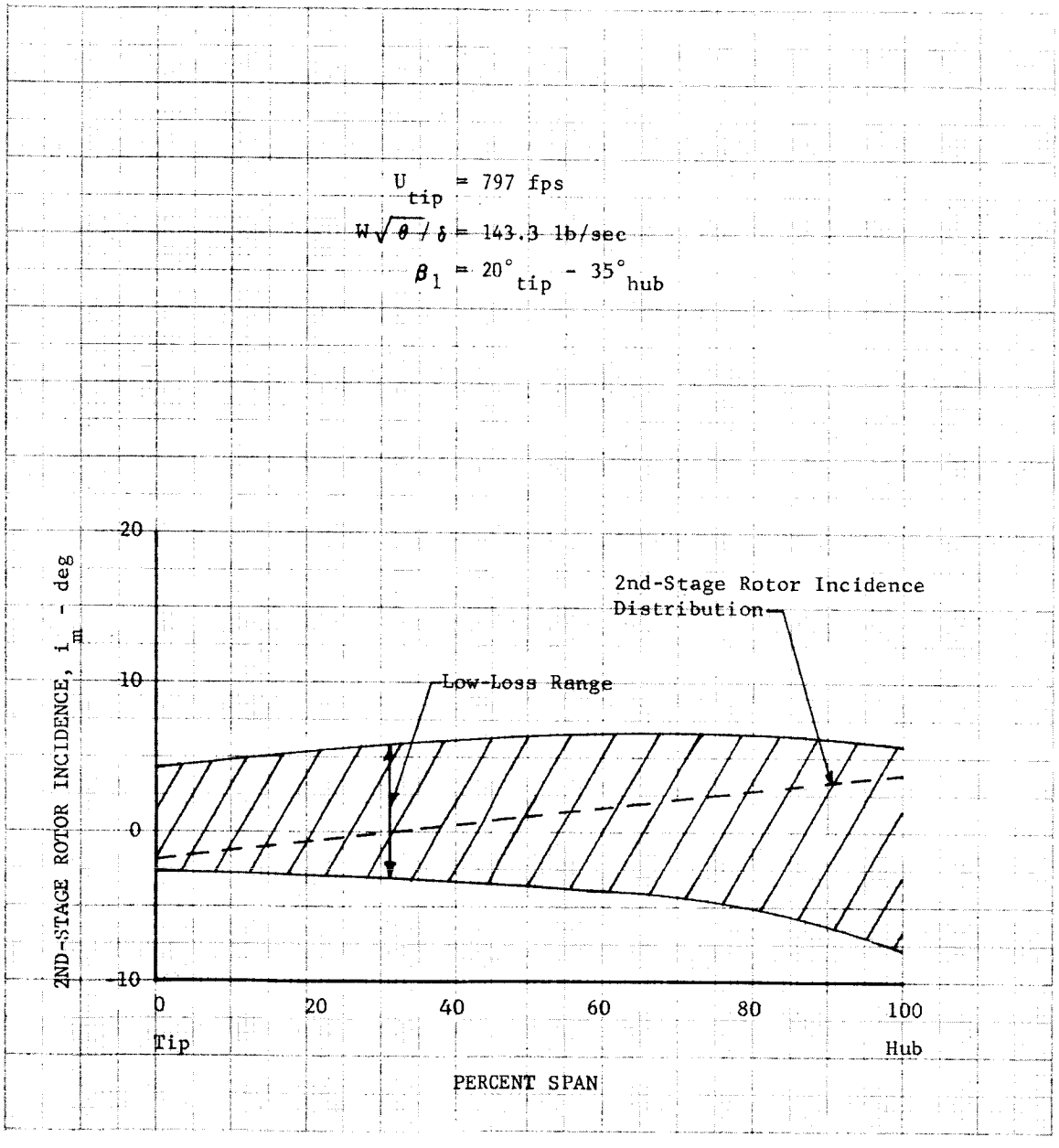

Figure 28. Radial Distribution of 2nd-Stage Rotor Incidence Angle for Selected Off-Design Stator Exit Air Angle

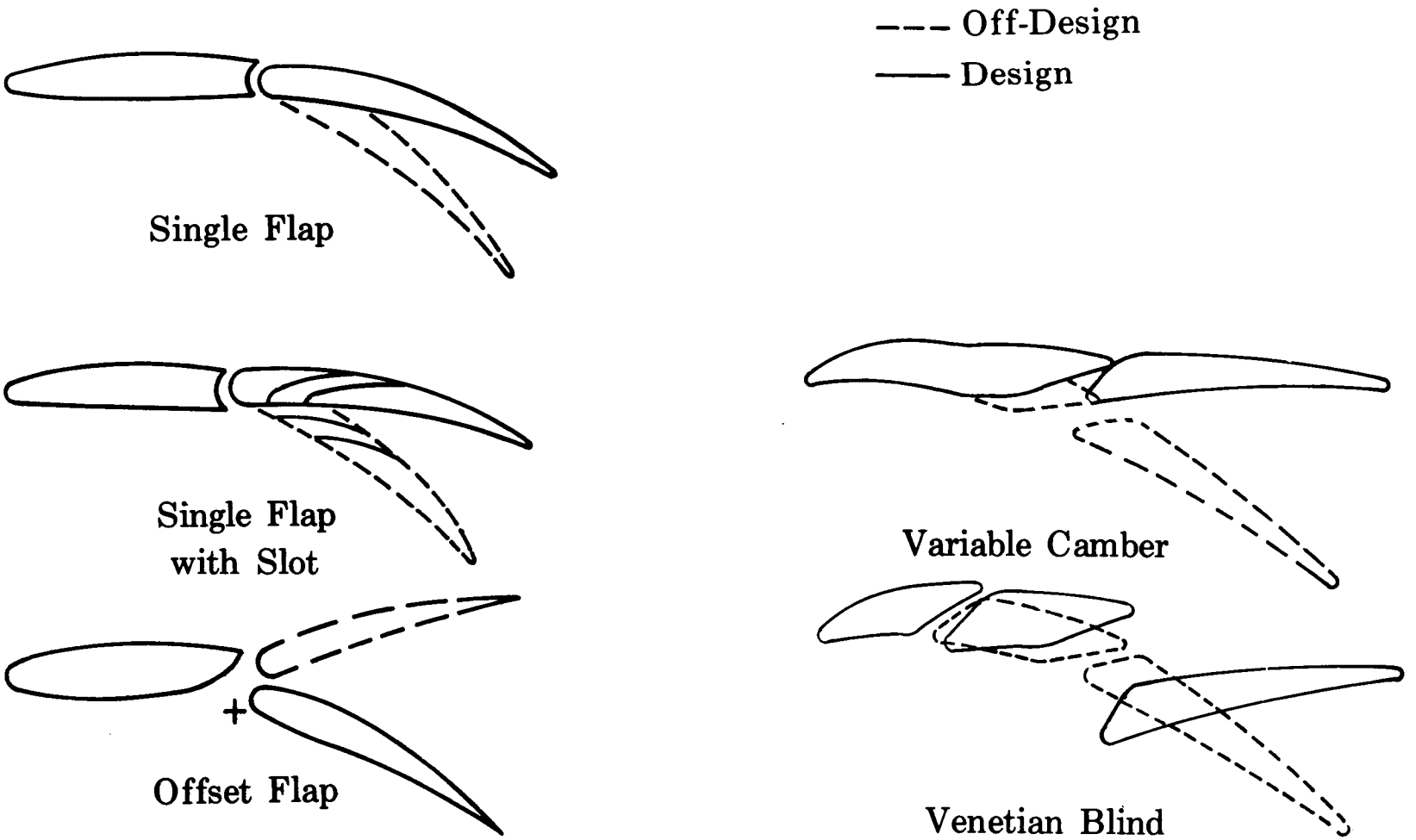

Figure 29. Variable Geometry Inlet Guide Vane Concepts

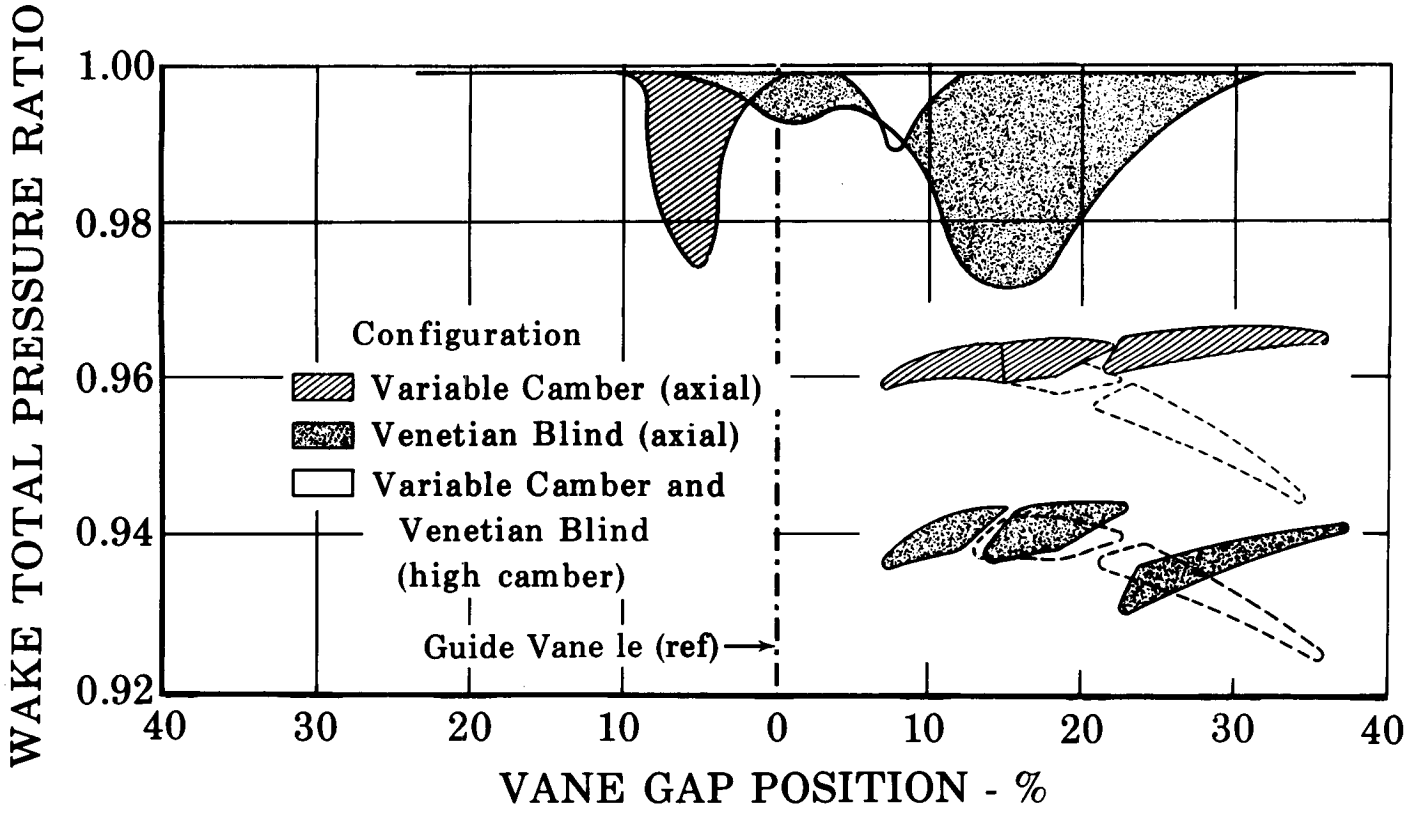

Figure 30. Variable Geometry Guide Vane Midspan Wake Comparison

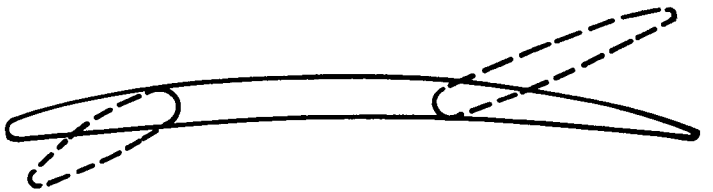

Leading and Trailing
Edge Flaps

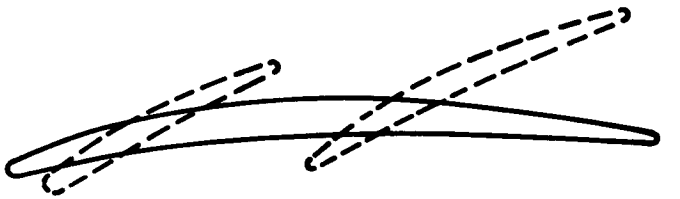

Double Flap Stator
(Stator B)

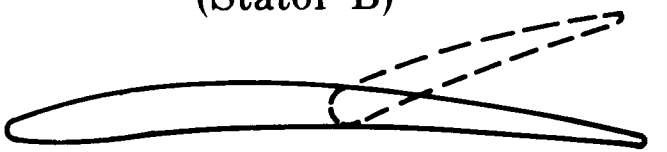

Trailing Edge Flap
(Stator A)

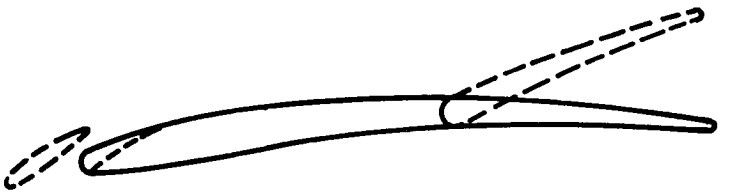

Retractable
Leading Edge Slat,
Trailing Edge Flap

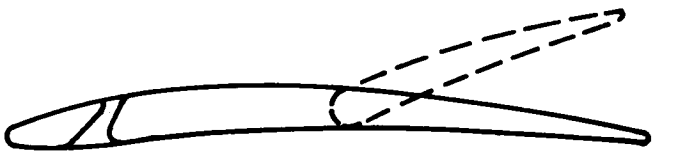

Trailing Edge Flap
With Leading Edge Slot

--- Off-Design

—— Design

Figure 31. Variable Geometry Stator Concepts

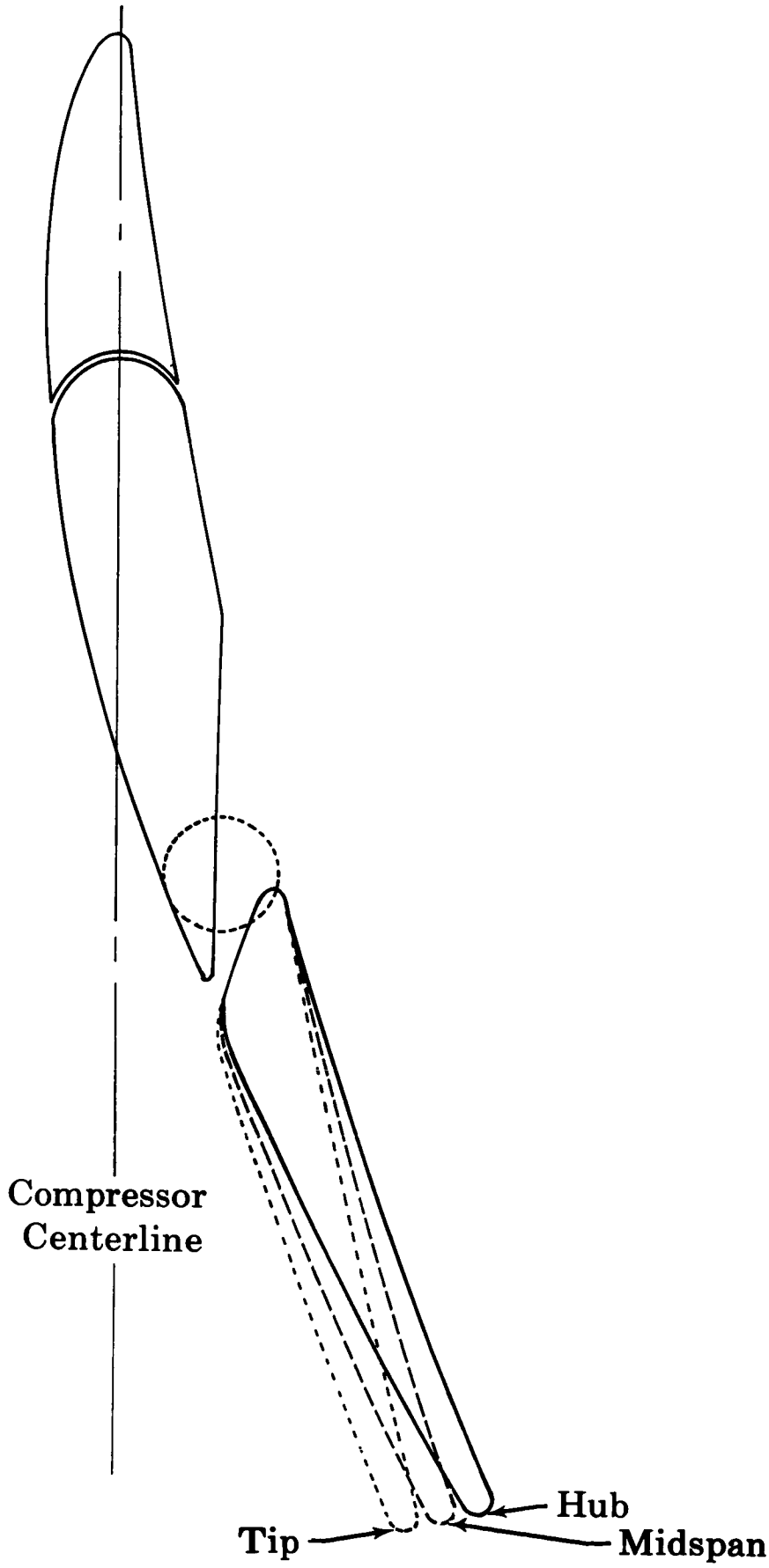

Figure 32. Basic Inlet Guide Vane Geometry

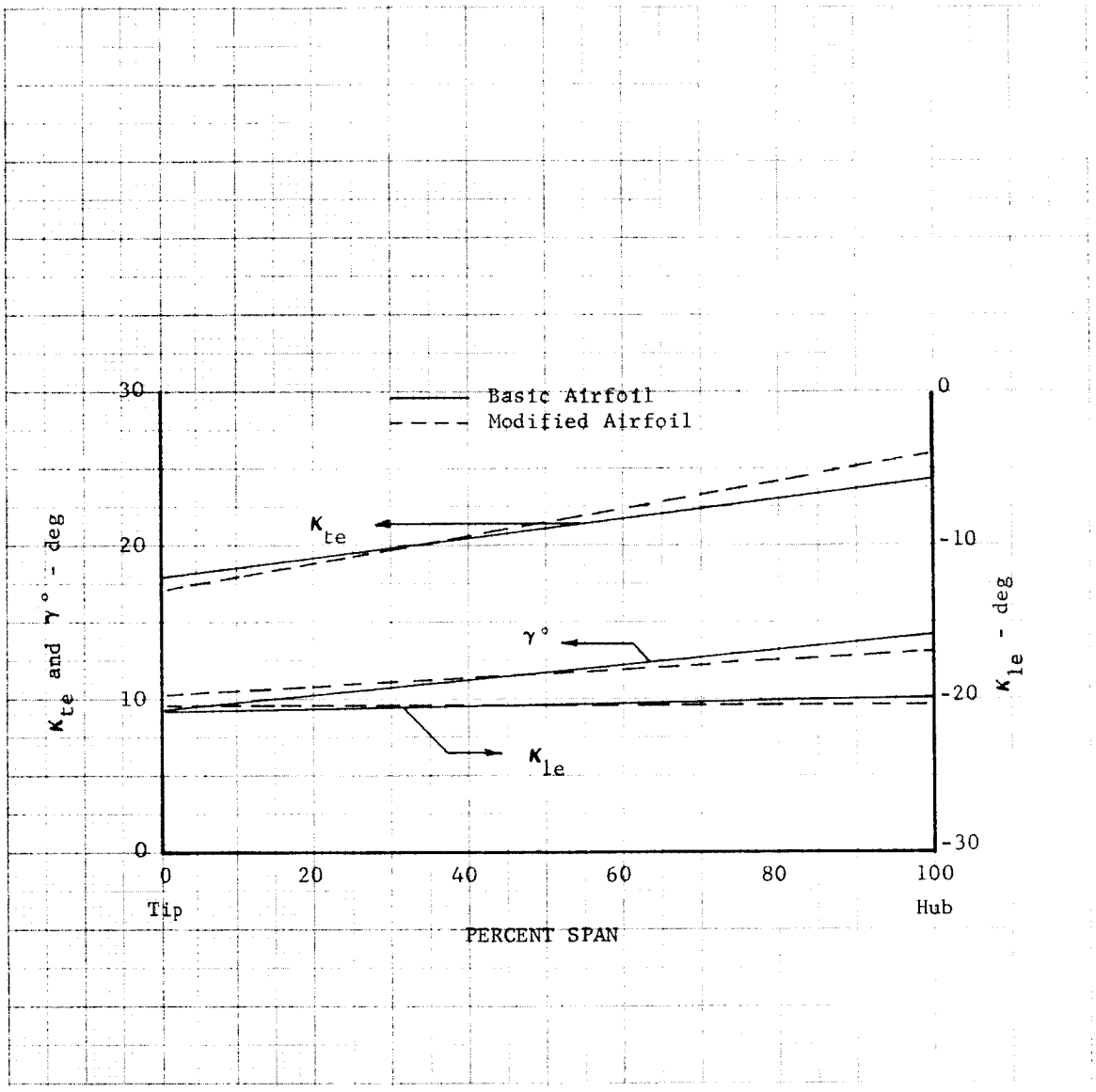

Figure 33. Radial Distribution of Metal Angles and Chord Angles for Basic and Modified Inlet Guide Vanes

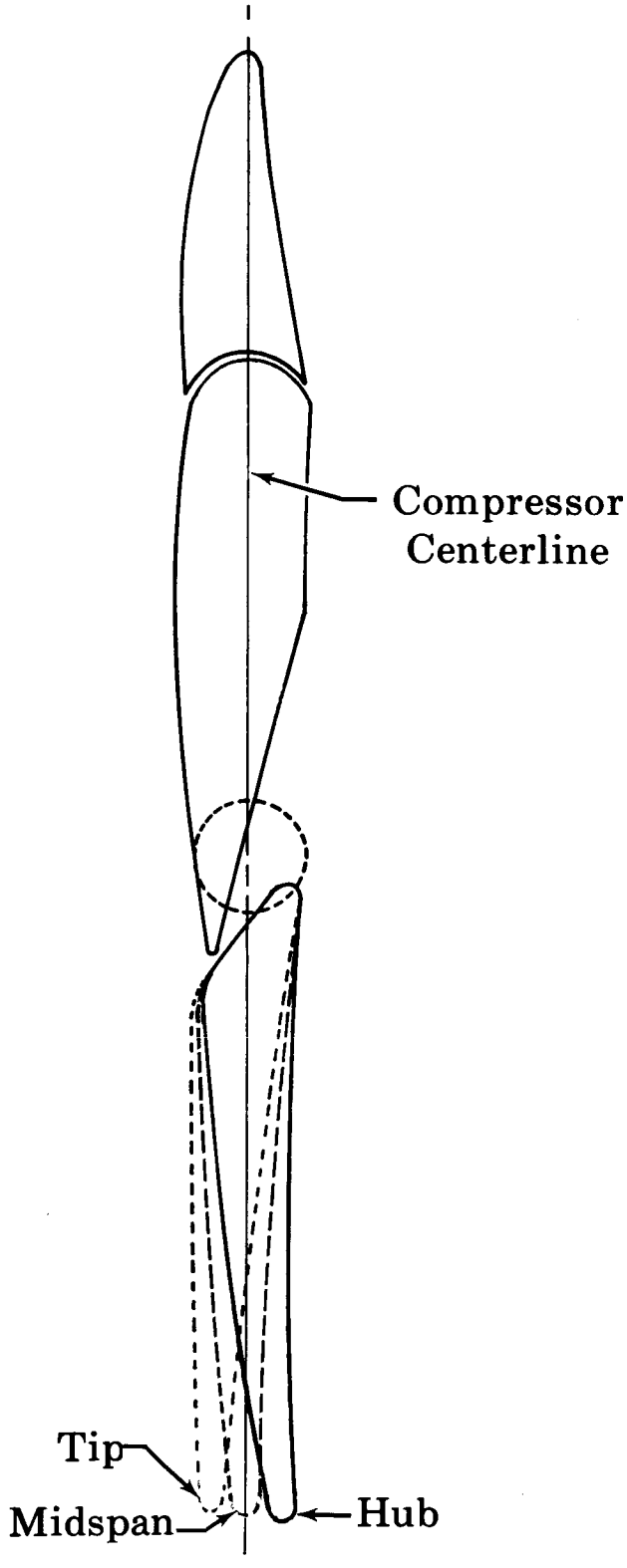

Figure 34. Inlet Guide Vane Design Point Geometry

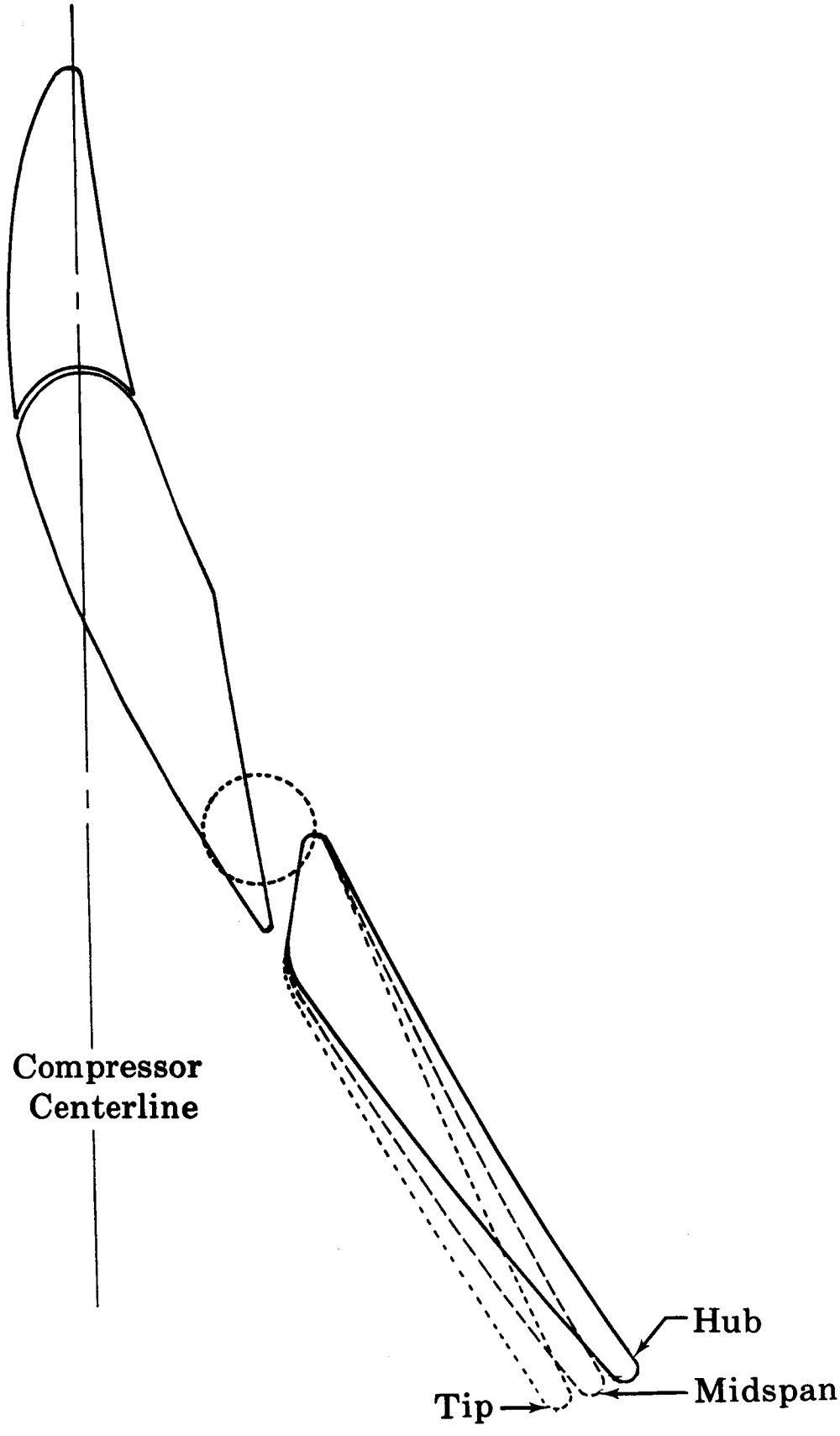

Figure 35. Inlet Guide Vane Off-Design Geometry

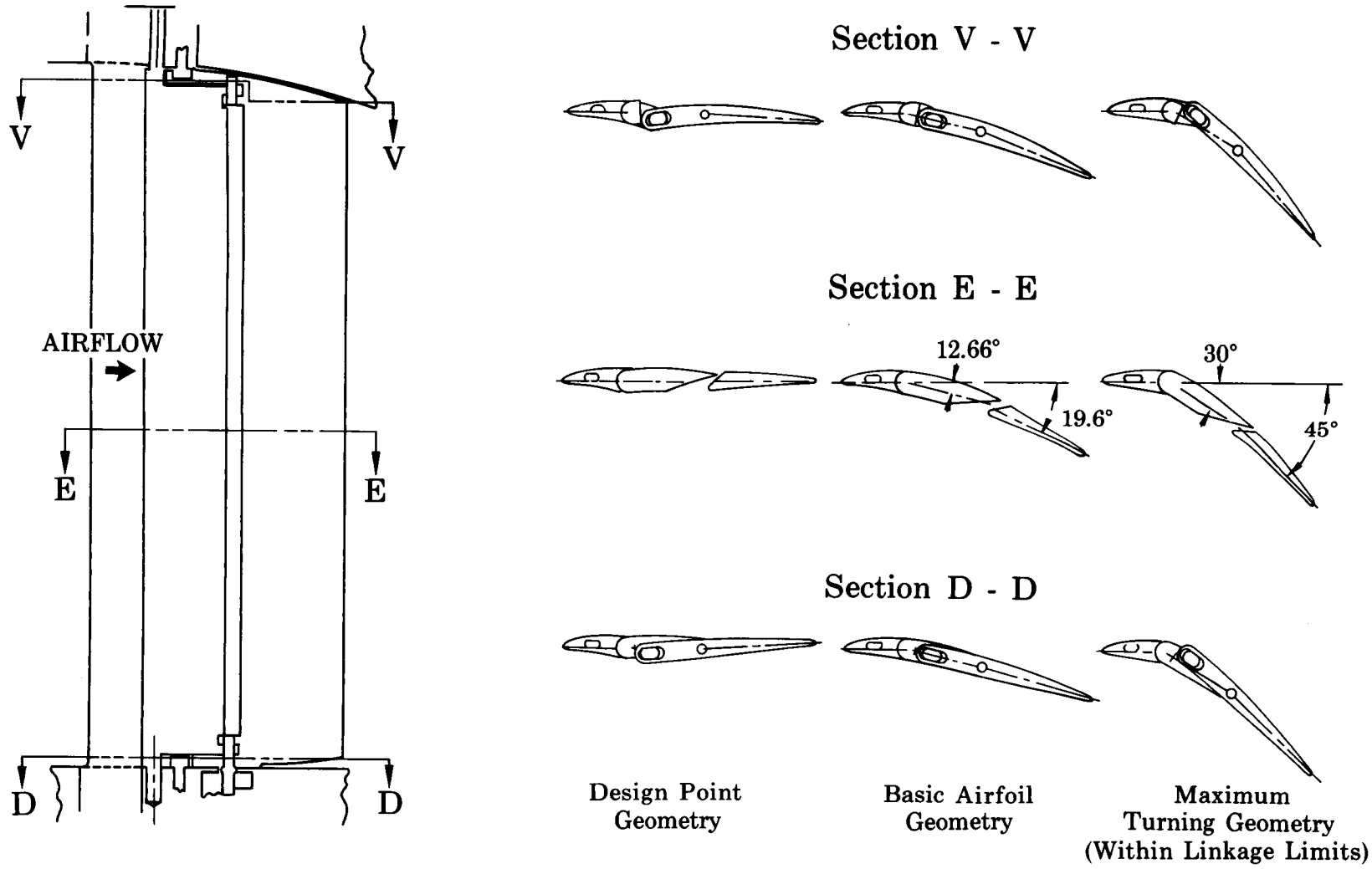

Figure 36. Variable Camber Inlet Guide Vane Linkage Influence on Extreme Hub and Tip Section Profiles

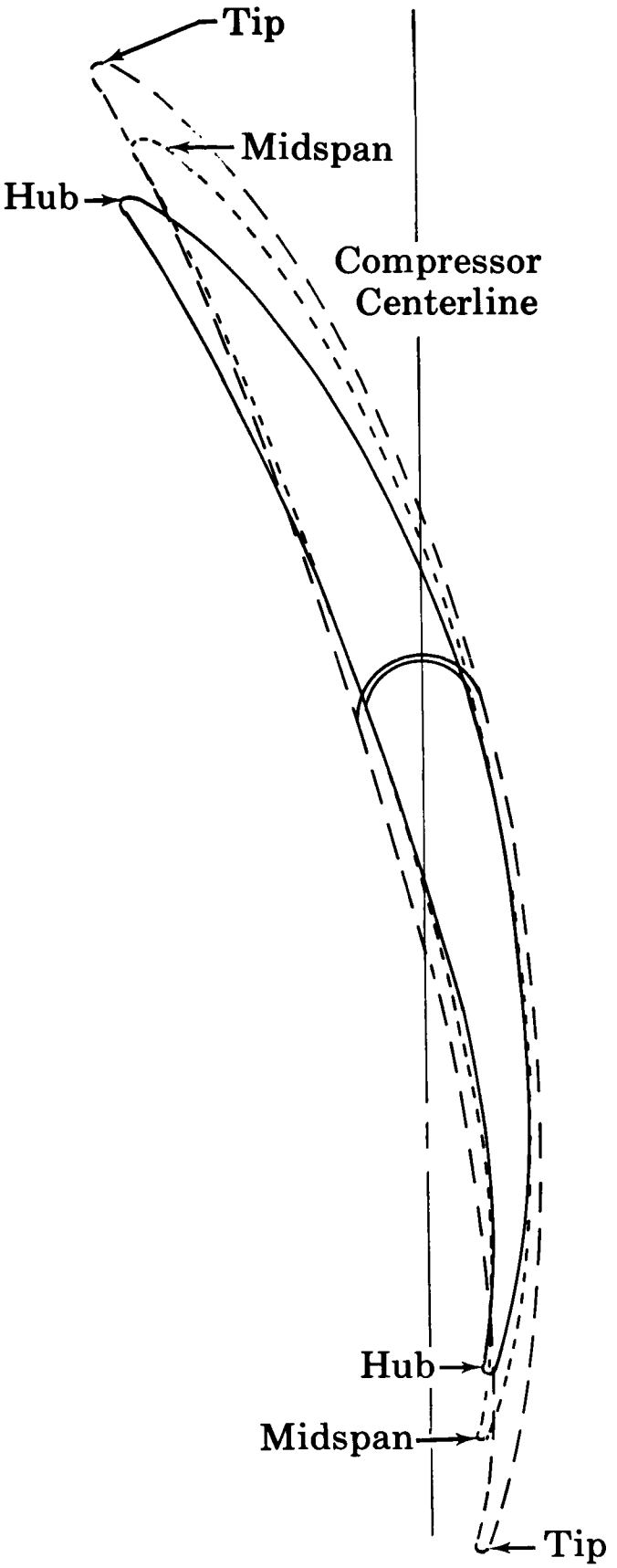

igure 37. Stator A Design Point Geometry

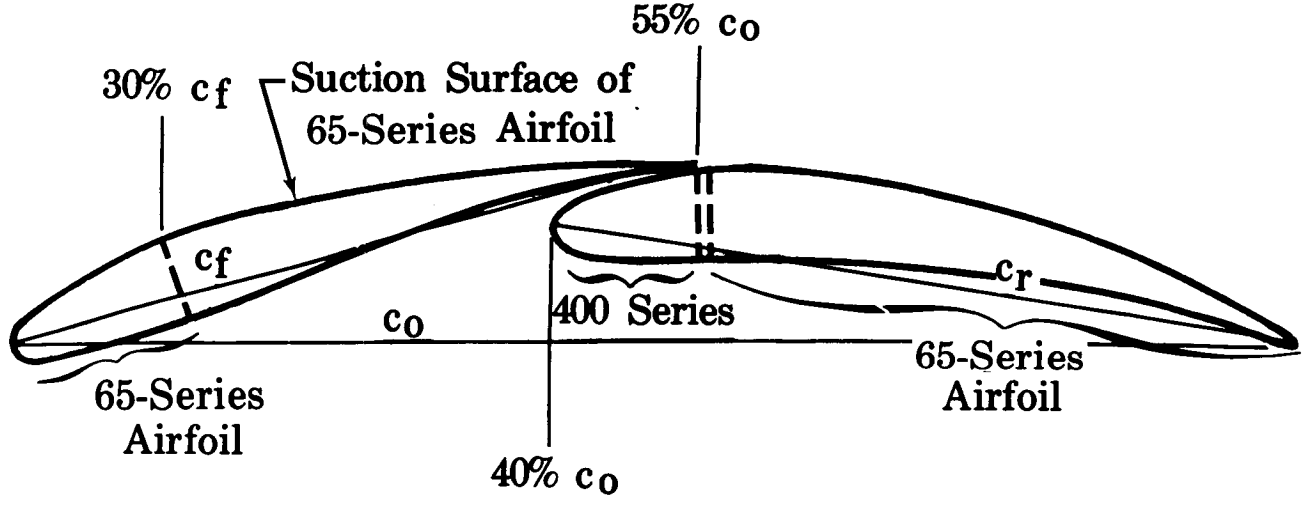

c_o = Chord of Basic 65-Series Airfoil
c_f = Chord of Front Flap
c_r = Chord of Rear Flap

Figure 38. Development of Stator B Design Point Section Geometry

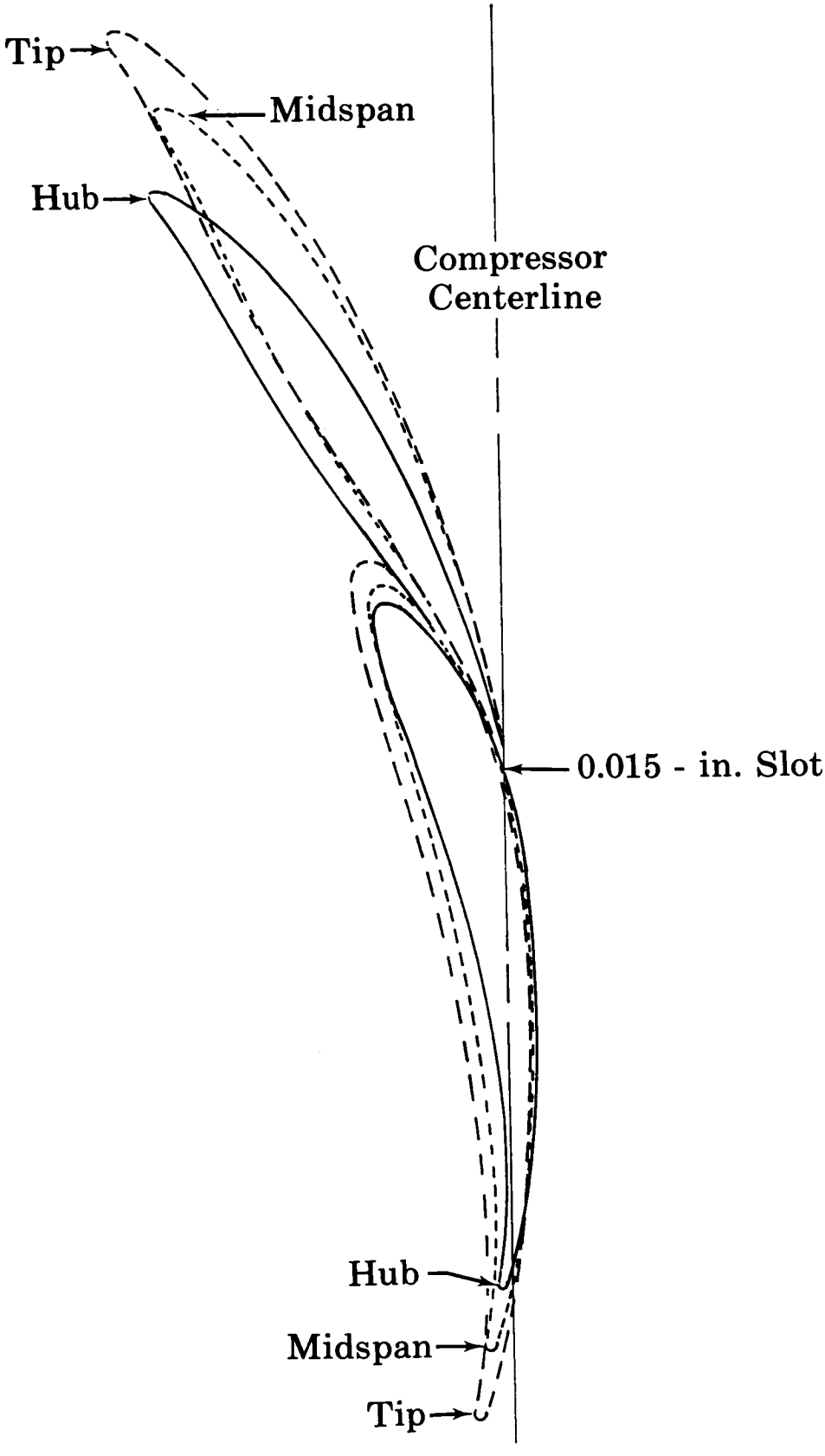

Figure 39. Stator B Design Point Geometry

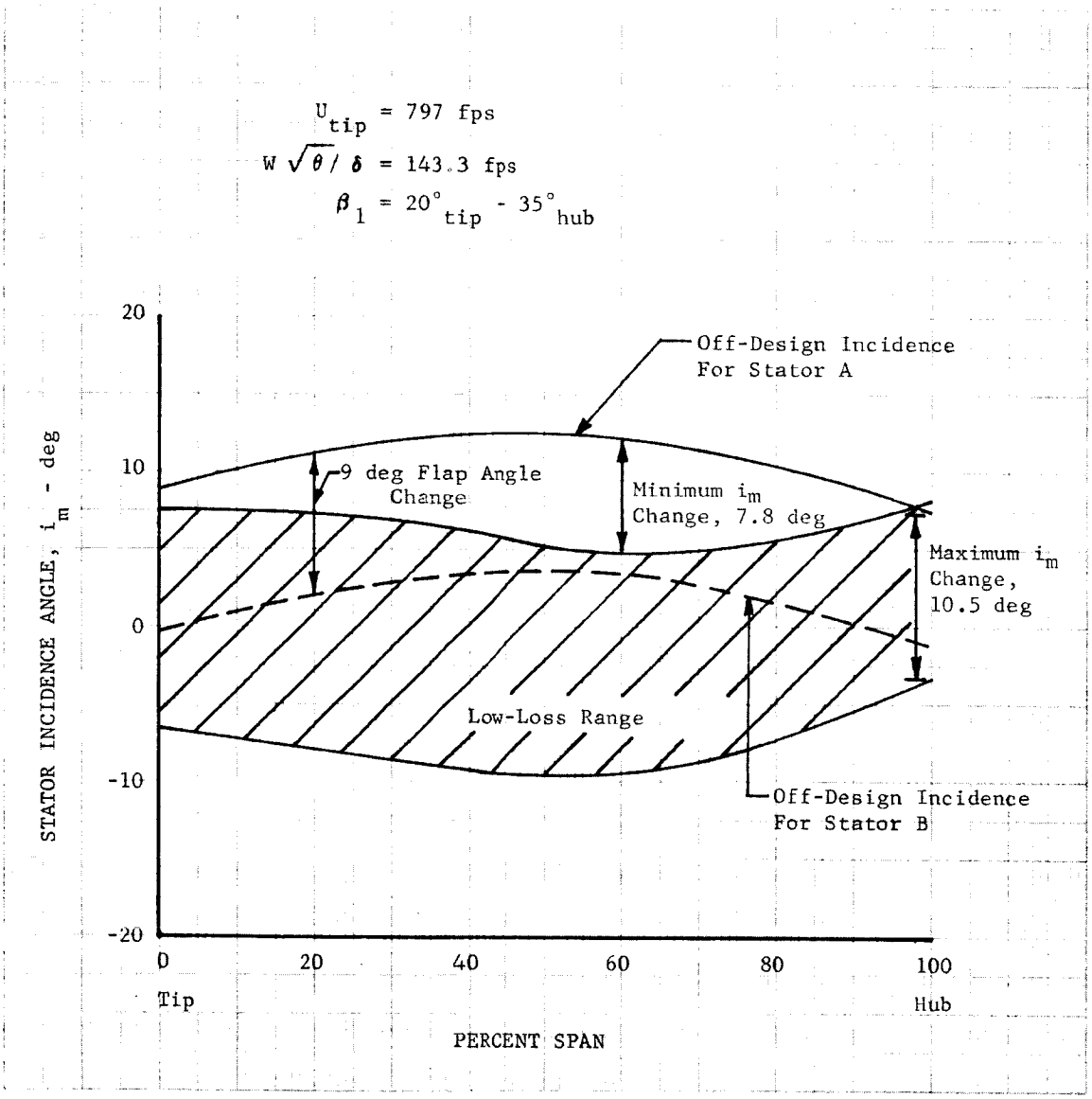

Figure 40. Effect of Stator Forward Flap Angle Change on Stator Incidence Angle at Off-Design Operation

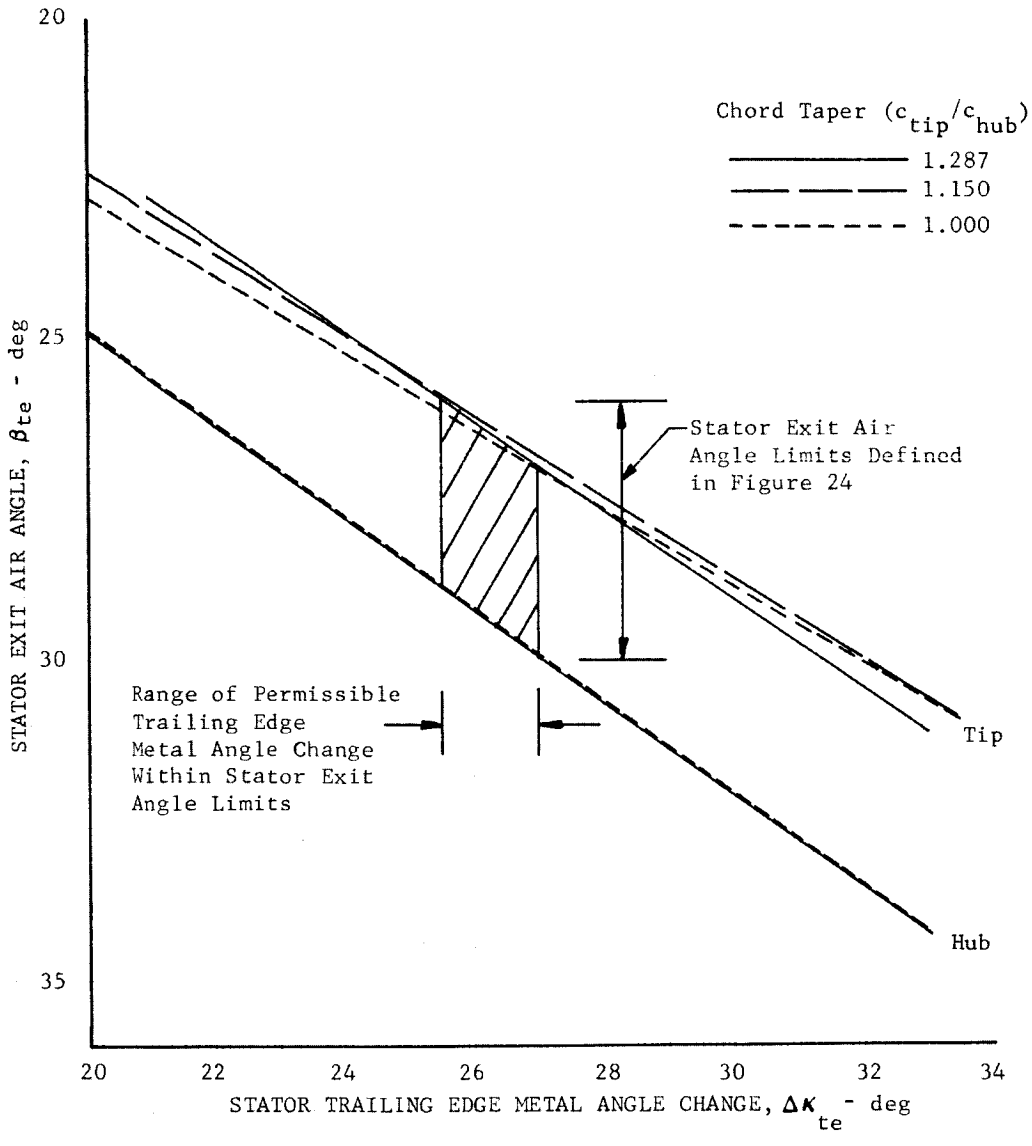

Figure 41. Effect of Stator Trailing Edge Metal Angle Change on Stator Exit Air Angle

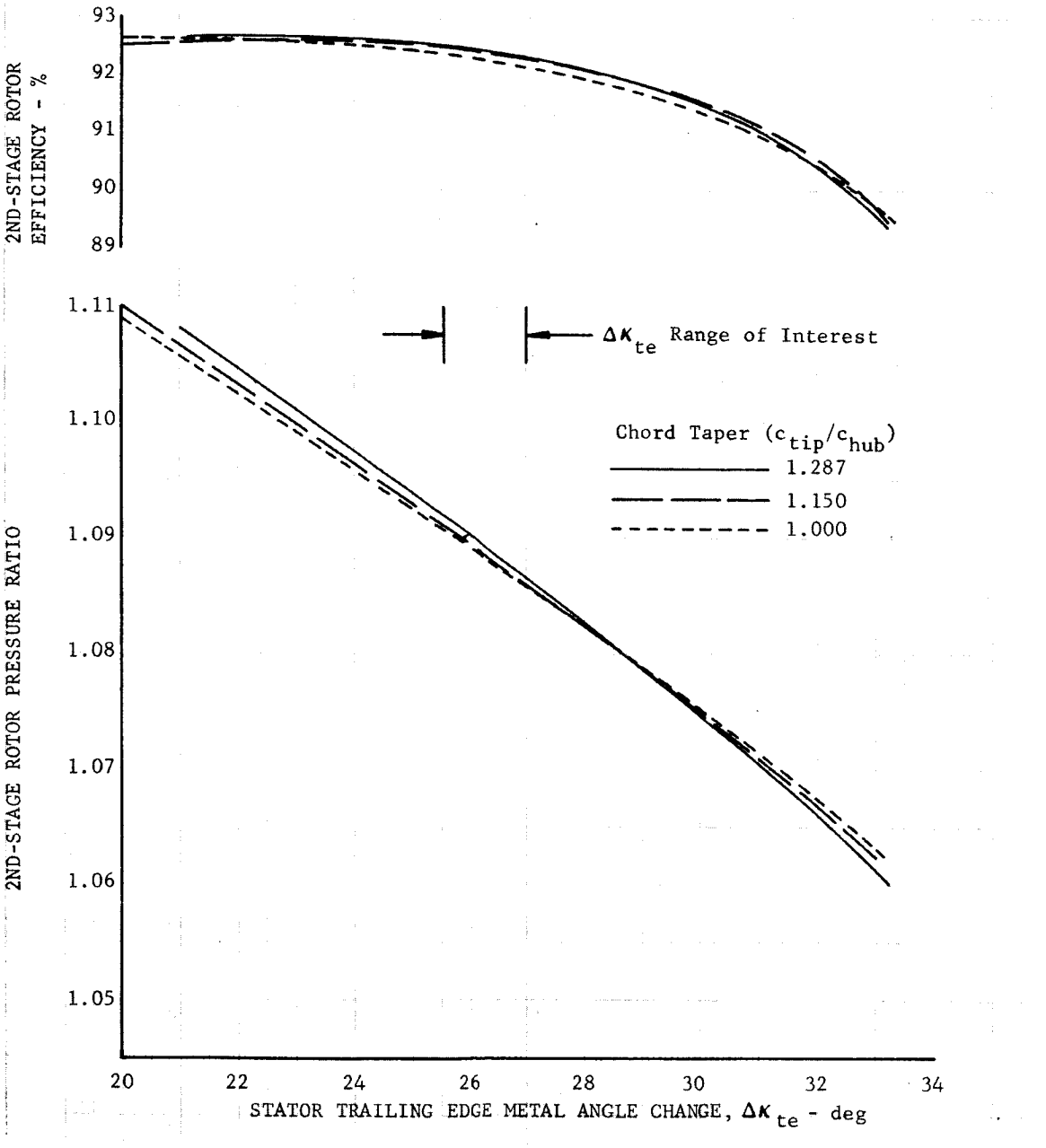

Figure 42. Effect of Stator Trailing Edge Metal Angle on 2nd-Stage Rotor Performance

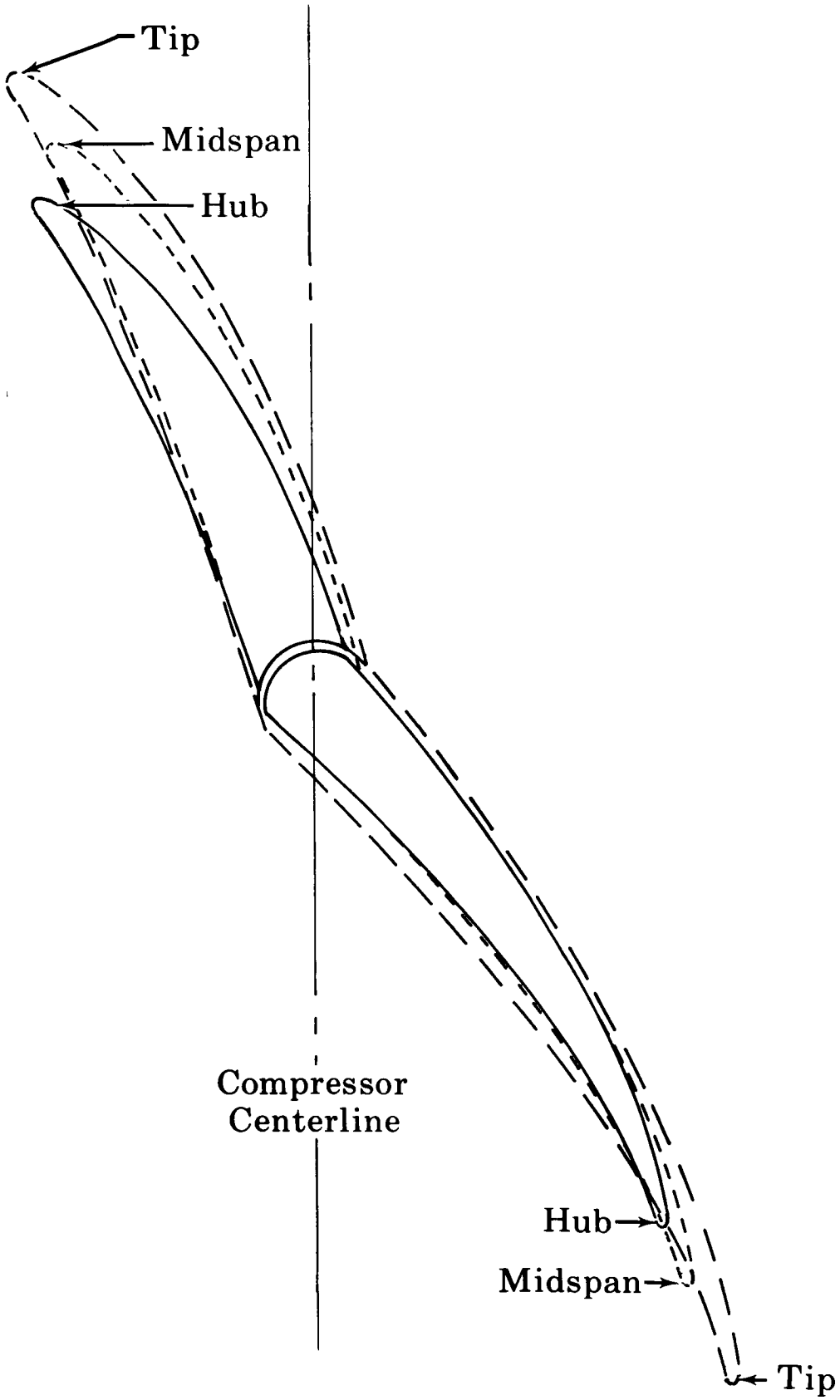

Figure 43. Stator A Off-Design Geometry

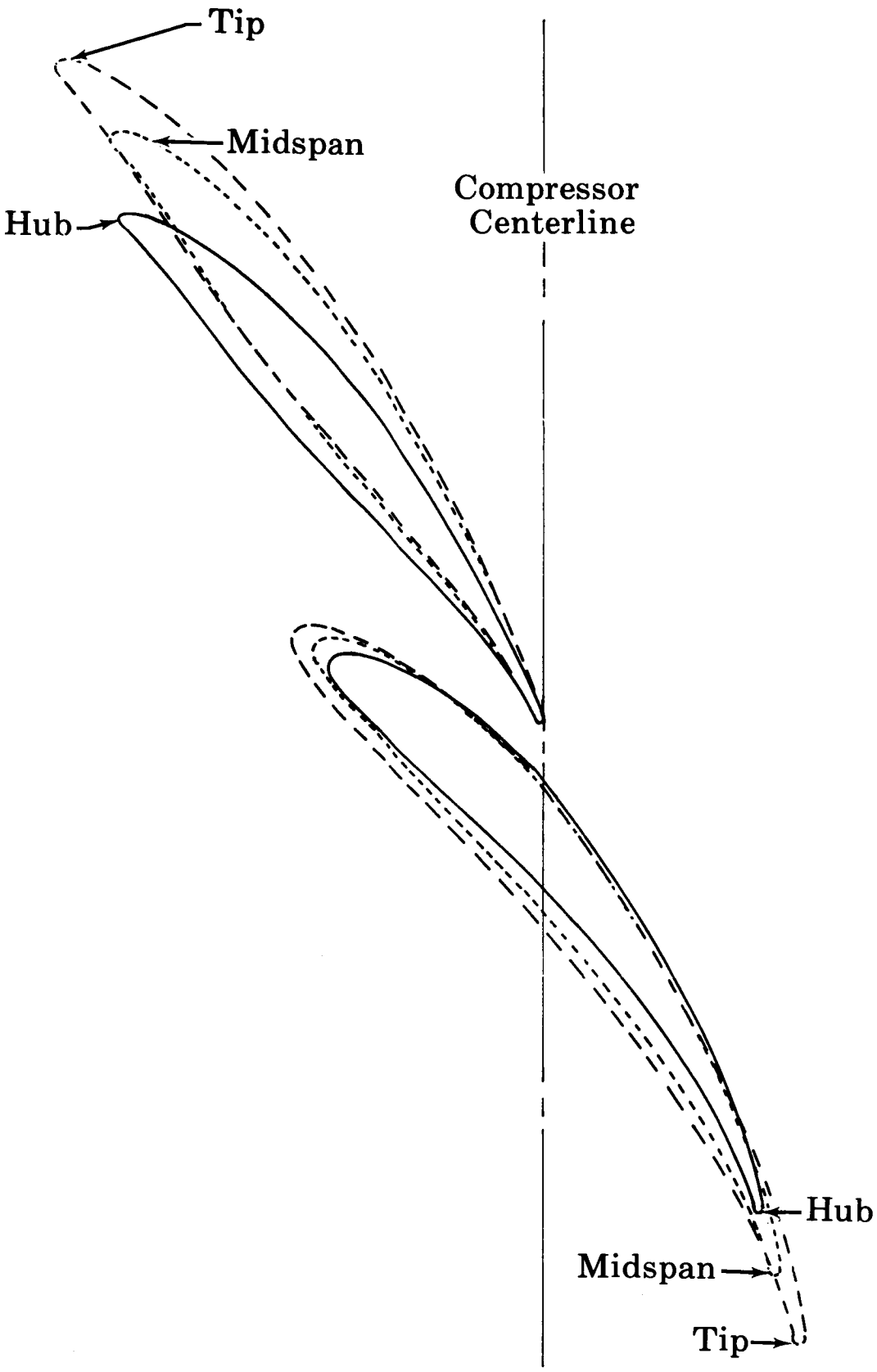

Figure 44. Stator B Off-Design Geometry

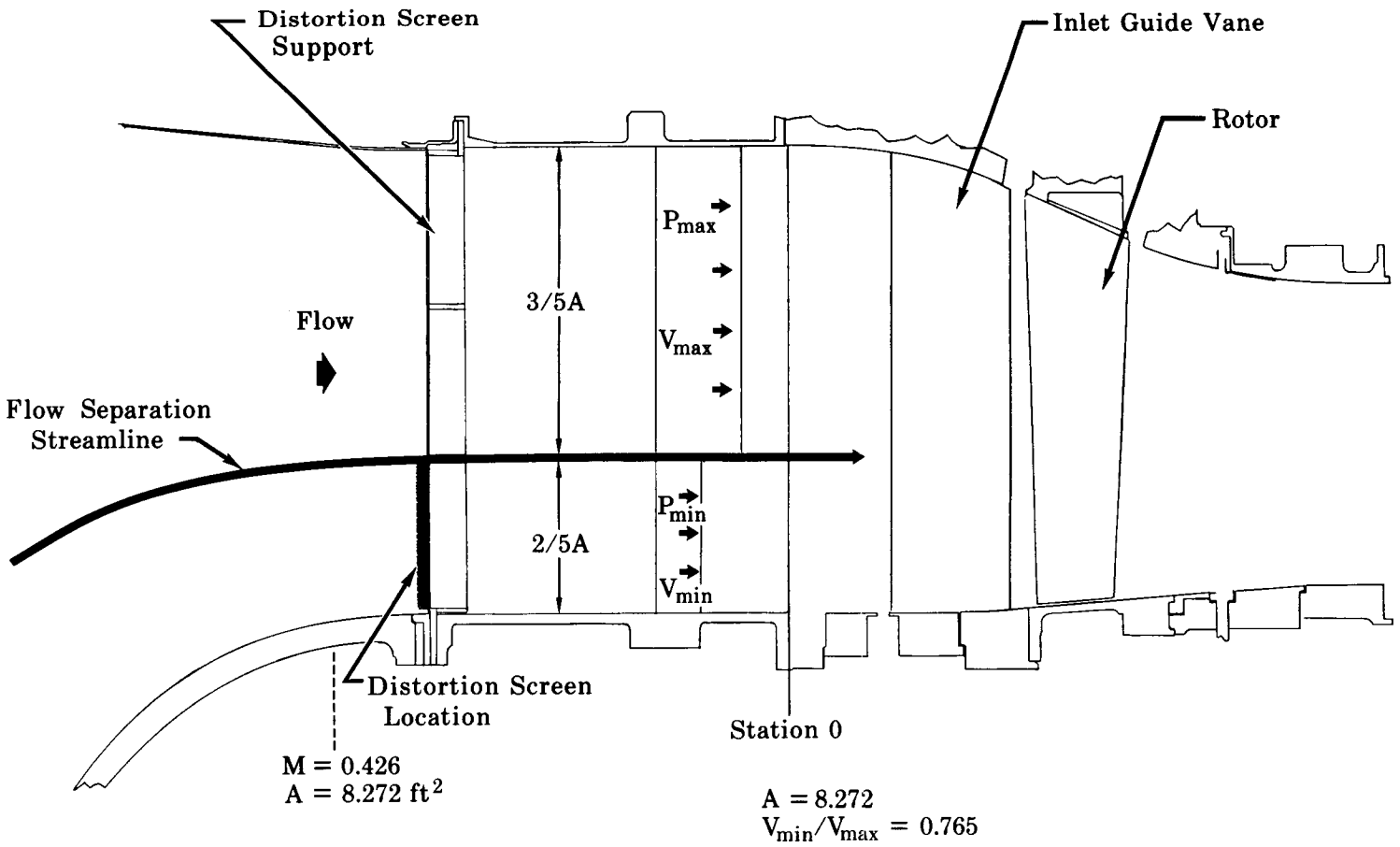

Figure 45. Flowpath Model for Radial Distortion Screen Design

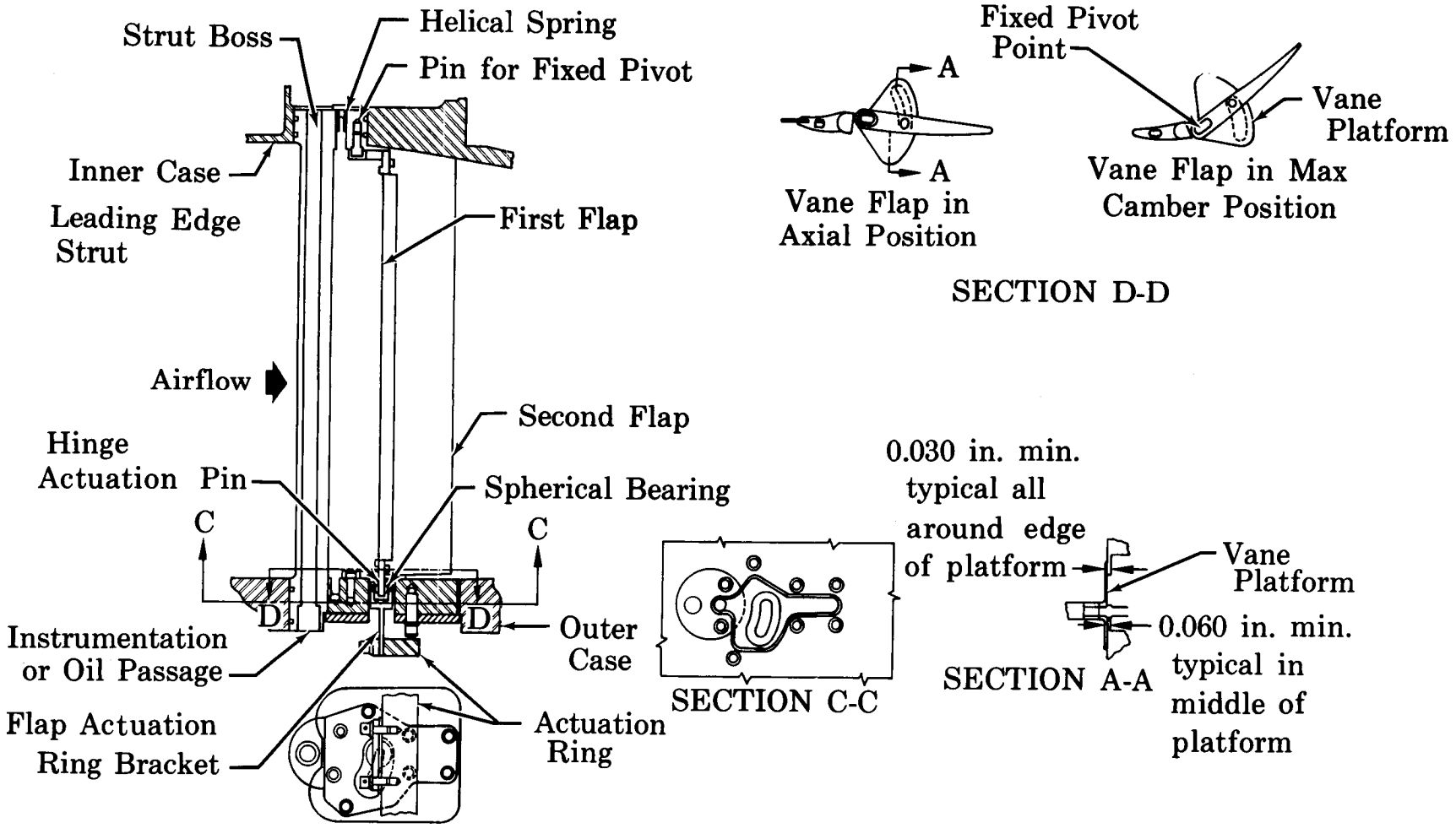

Figure 46. Inlet Guide Vane Linkage

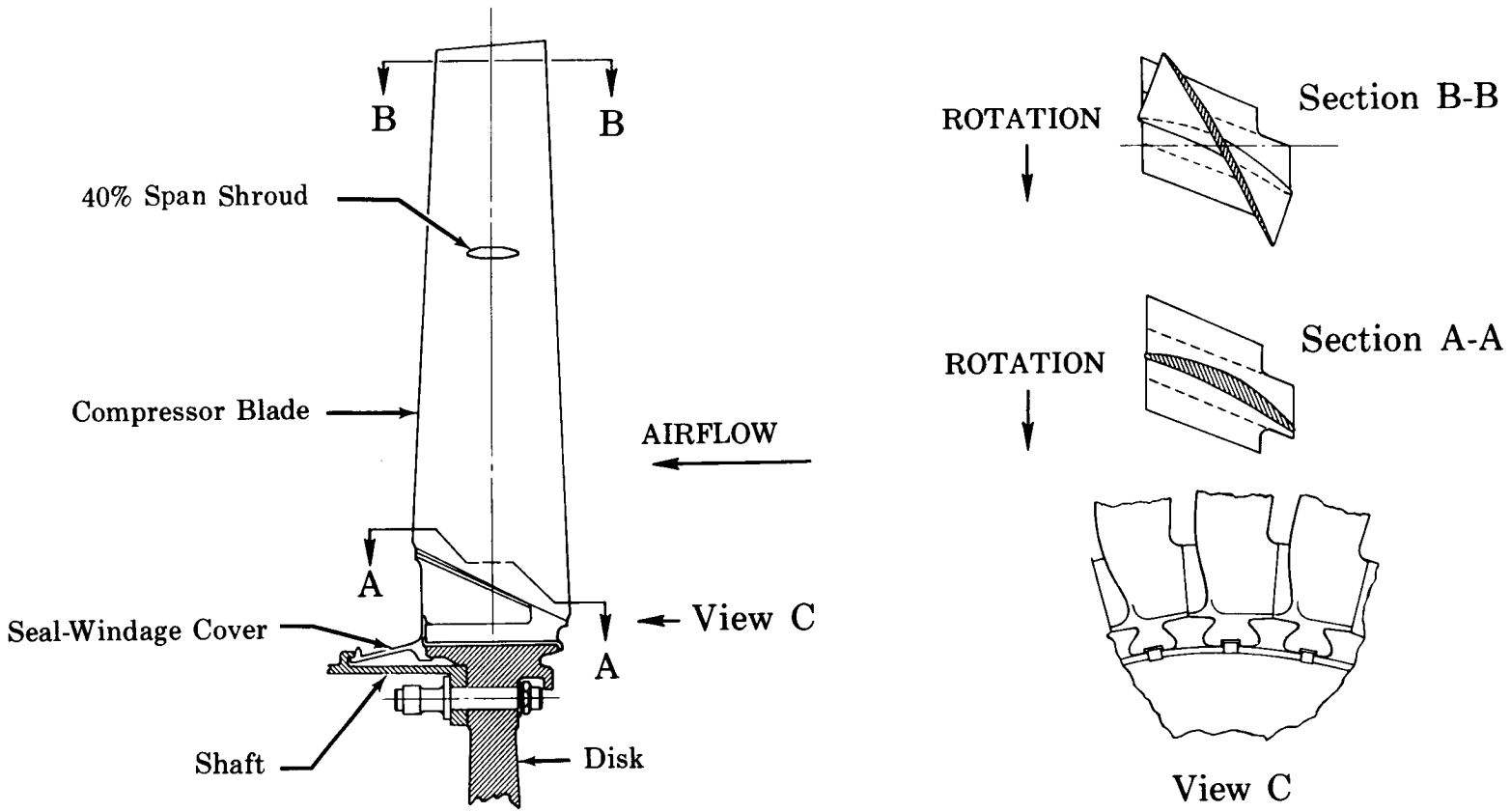

Figure 47. Rotor Blade Attachment

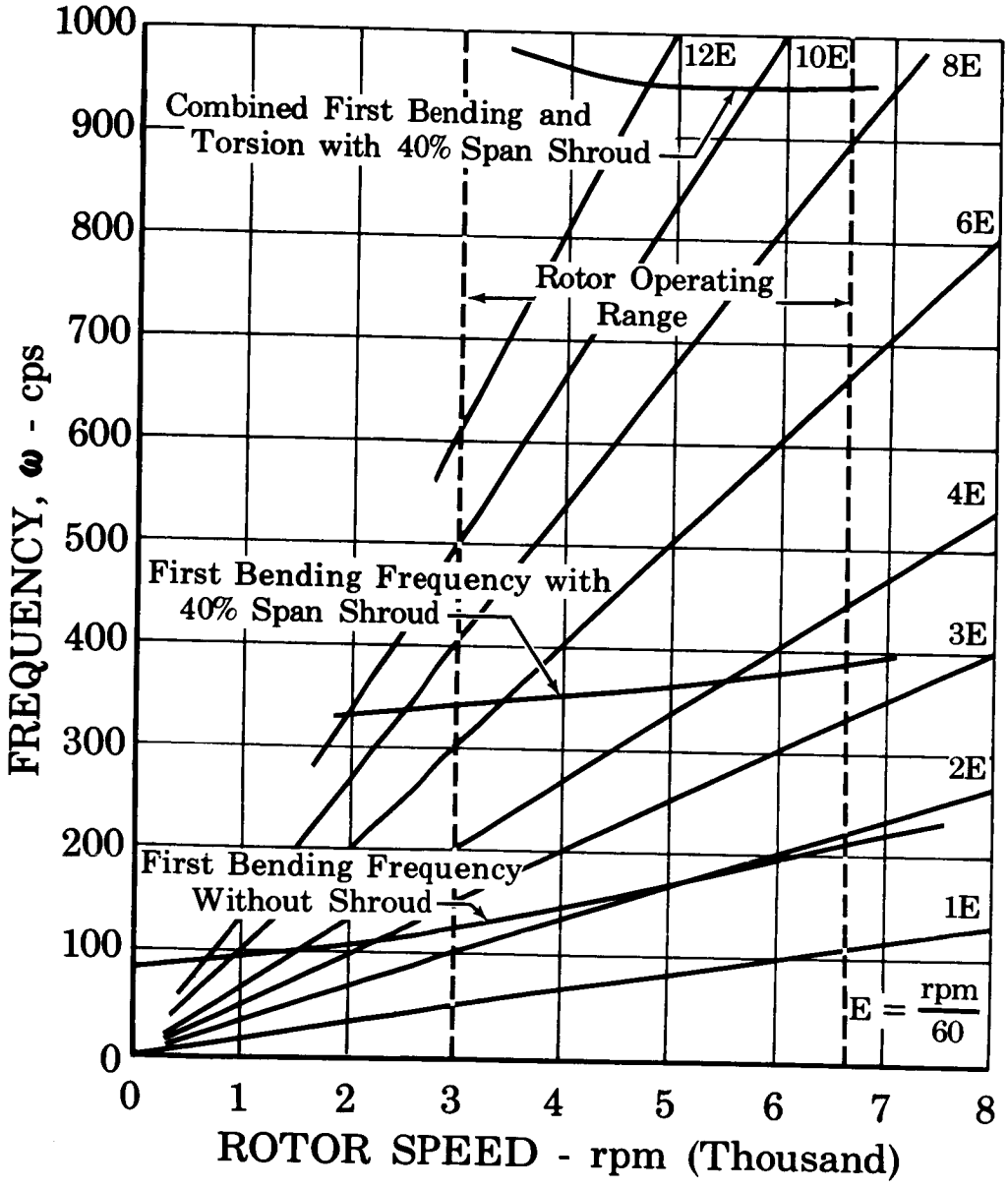

Figure 48. Resonance Diagram for Rotor

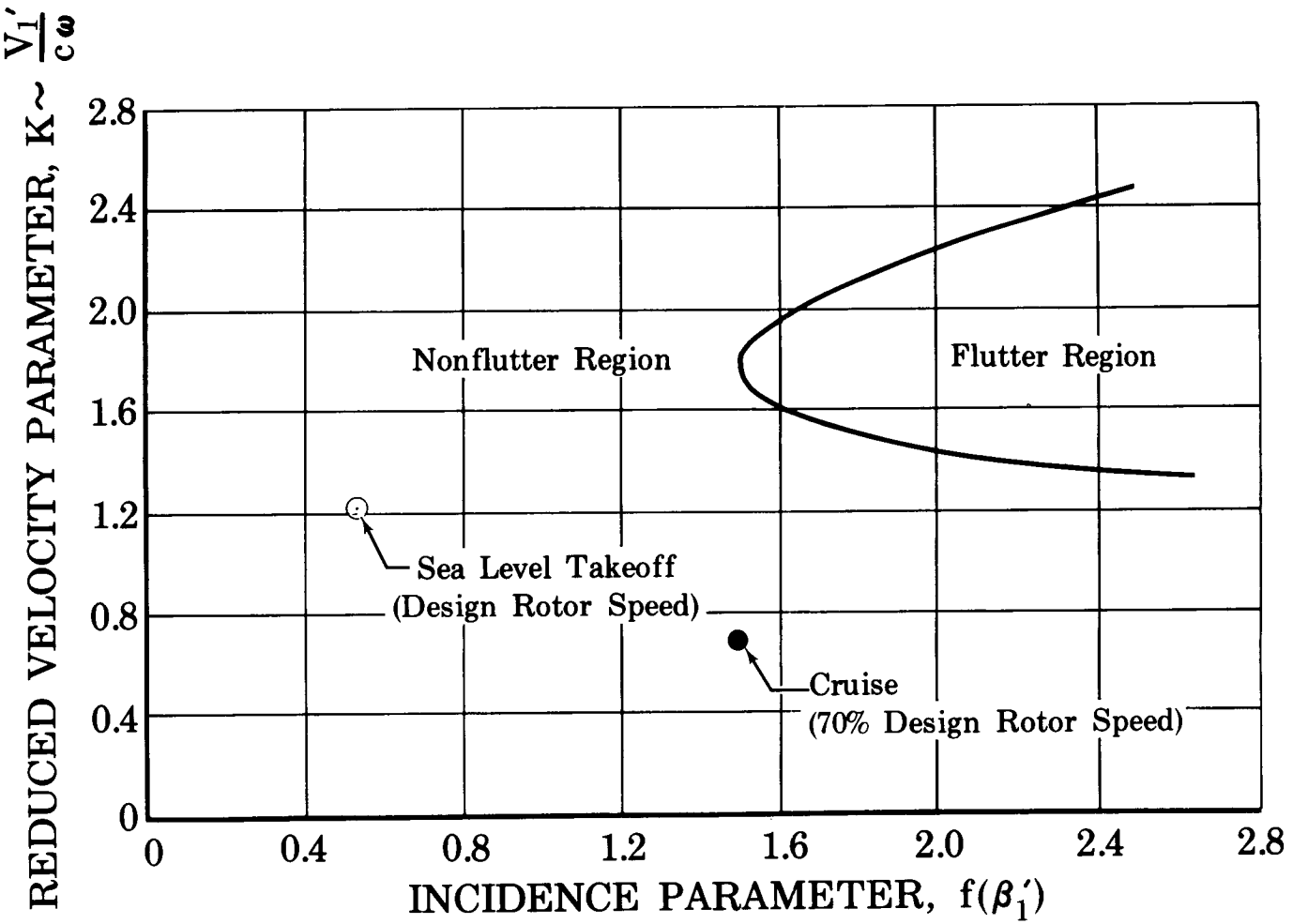

Figure 49. Calculated Rotor Blade Flutter Characteristics

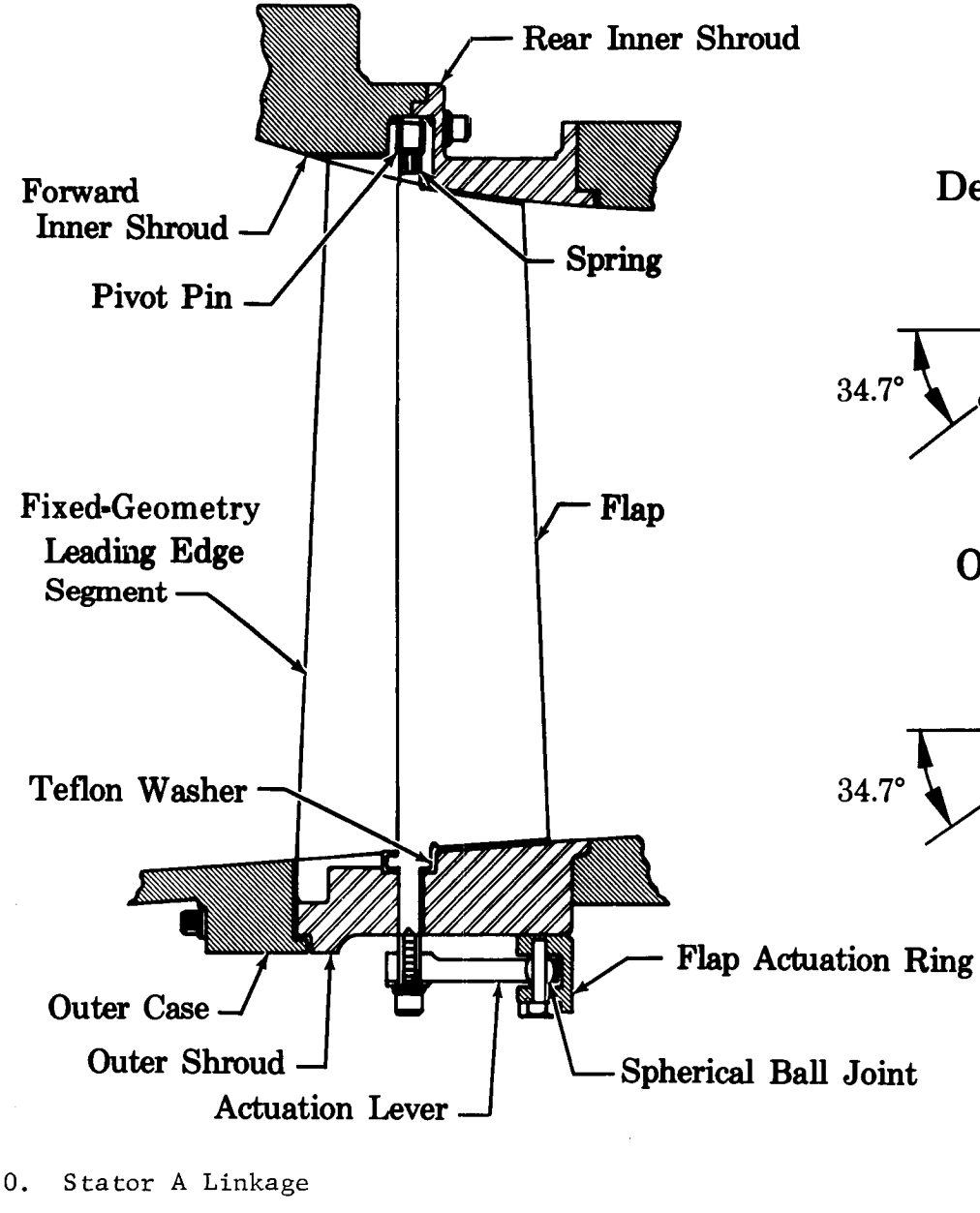

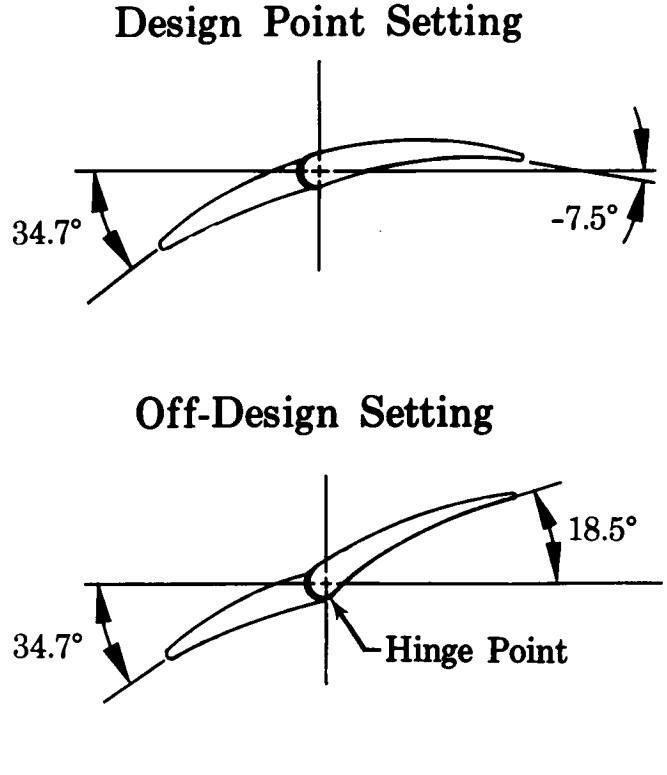

Figure 50. Stator A Linkage

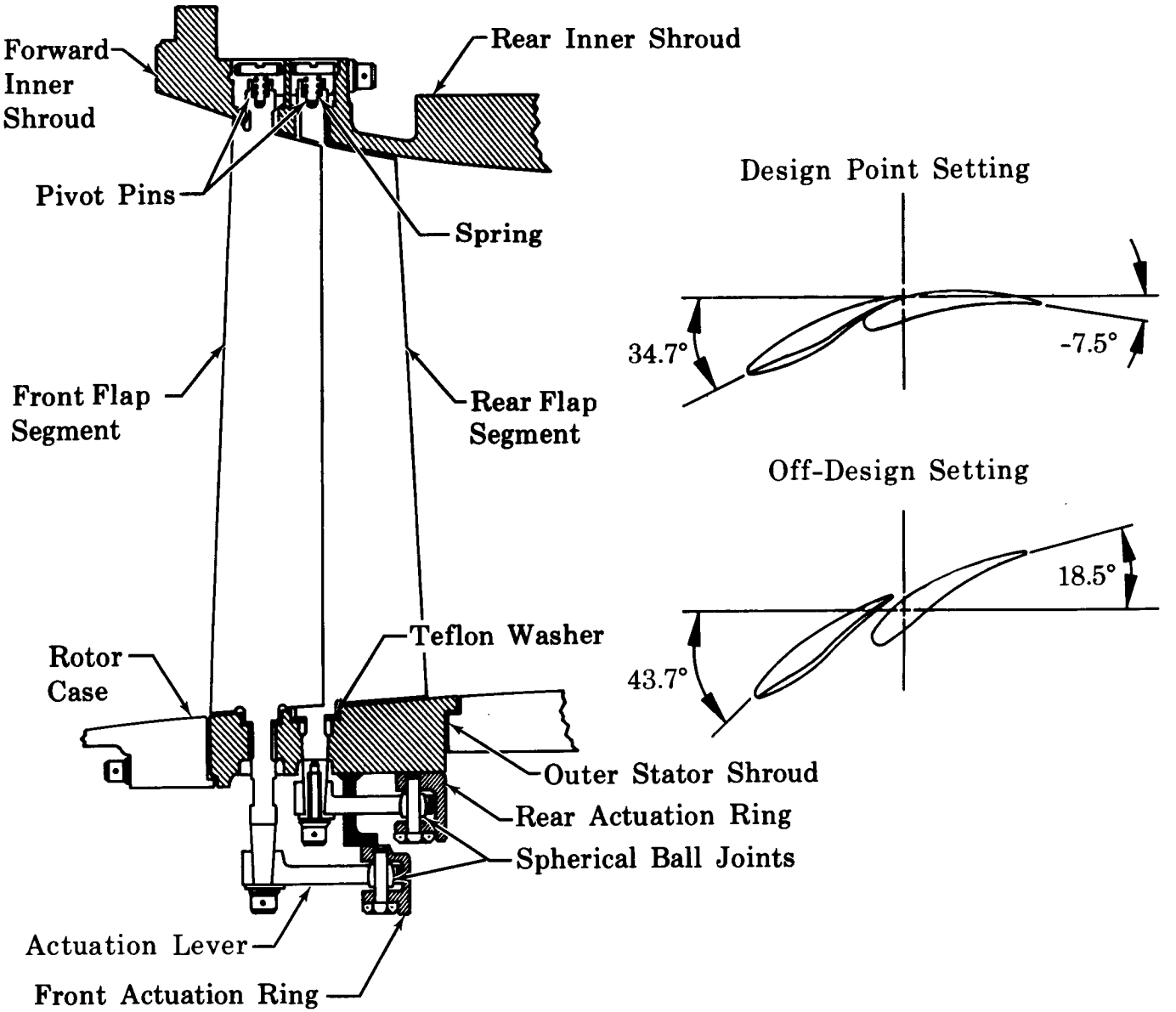

Figure 51. Stator B Linkage

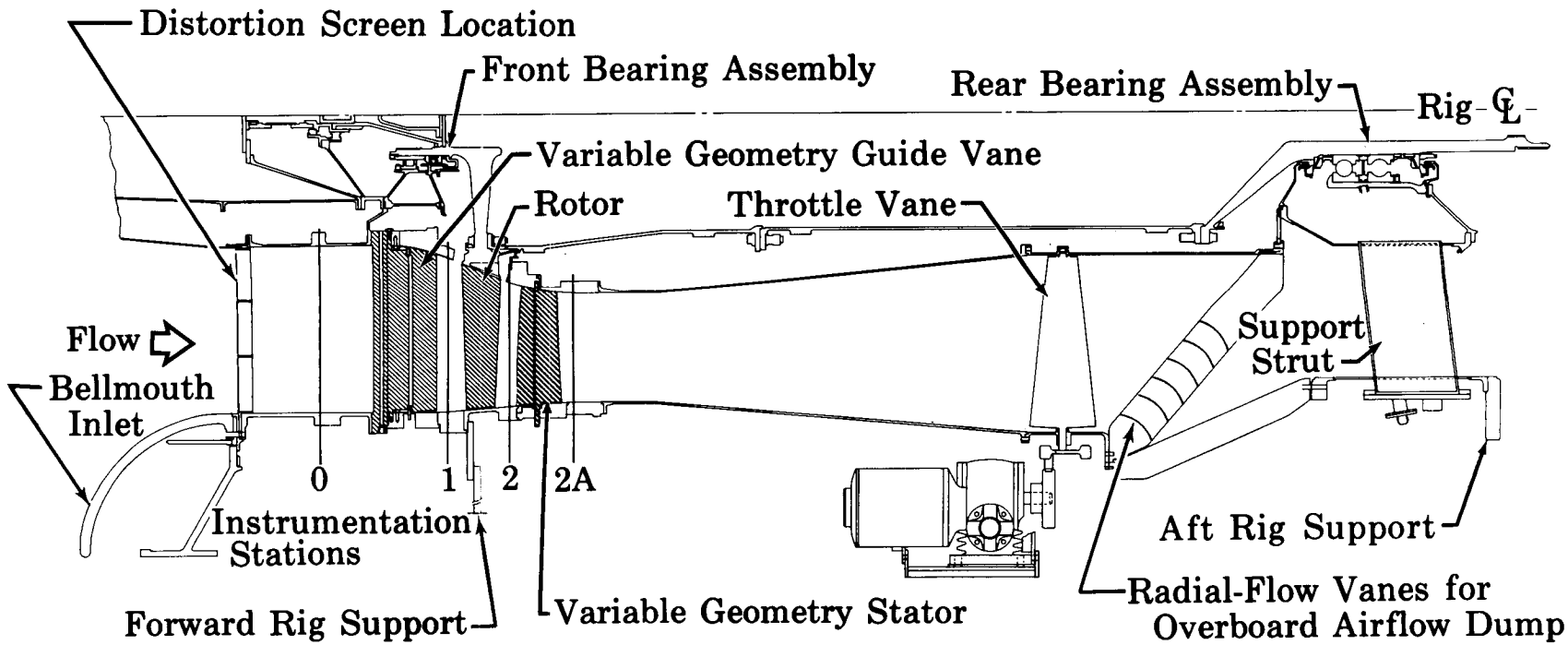

Figure 52. Compressor Test Rig

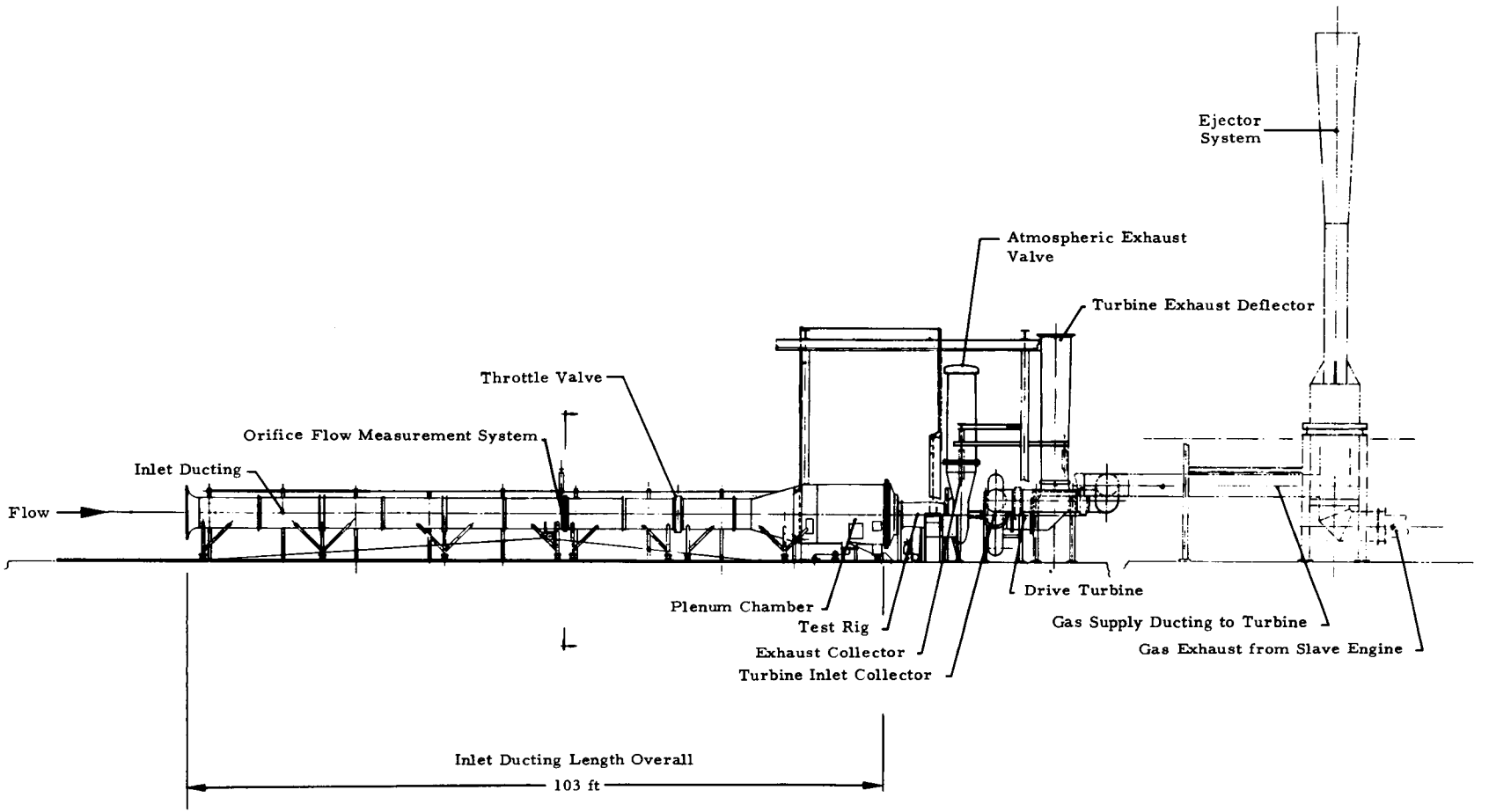

Figure 53. Compressor Research Facility

APPENDIX A
DEFINITION OF SYMBOLS

A_A	Flowpath annular area, $in.^2$
c	Chord length, in.
D	Diffusion factor
E	Rotor speed frequency, rpm/60
i_m	Incidence angle, deg (based on equivalent circular arc meanline)
k	Reduced velocity parameter, $V_1'/c\omega$
m	Meridional plane
M	Mach number
p	Static pressure, psia
q	Pressure equivalent of the velocity head, psia
S	Blade spacing, in.
s	Blade span, in.
t	Blade maximum thickness, in.
U	Rotor speed, ft/sec
V	Velocity, ft/sec
W	Actual flowrate, lb_m/sec
β	Air angle, deg (from axial direction)
$\Delta\beta$	Flow turning angle
ϵ	Flow angle in meridional plane
γ°	Blade-chord angle, deg
δ	Ratio of total pressure to NASA standard sea level pressure of 2116 psf
δ°	Deviation angle, deg
η_{ad}	Adiabatic efficiency
θ	Ratio of total temperature to NASA standard sea level temperature of 518.7°R
κ	Blade metal angle, deg (based on equivalent circular arc meanline)
ρ	Density, lb_m/ft^3
σ	Solidity, c/S
ϕ	Blade camber angle, $\kappa_{le} - \kappa_{te}$, deg
ω	Torsional vibration frequency, cycles/sec
$\bar{\omega}$	Total pressure loss coefficient

Subscripts

0	Guide vane inlet
1	Rotor inlet
2	Rotor exit
2A	Stator exit
le	Leading edge
te	Trailing edge
m	Meridional component
z	Axial component
θ	Tangential component

Superscripts

'	Relative rotor blade

APPENDIX B
DESCRIPTION OF COMPUTER PROGRAMS AND FLOWPATH MODEL

Computer Programs

Two computer programs are utilized to model axial flow compressor aerodynamics: (1) Axial Flow Compressor Calculation and (2) Streamline Calculation Deck. The functions of these two programs are summarized in the succeeding paragraphs.

Axial Flow Compressor Calculation (AFCC)

This computer program calculates the entrance and discharge conditions for each blade row of an axial flow compressor. The calculation is required to satisfy the equation of motion for an axisymmetric flow at each of these transverse planes with the assumption that the streamline curvature in the meridional plane may be neglected. Thus, the radial distribution of static pressure reflects swirl velocities but does not account for wall curvature. Radial velocity components, although not calculated, may be introduced as an input item to the program. The program is provided with optional subroutines to calculate the loss coefficient, minimum loss incidence angle, and unstalled operating range, for all of the compressor blade types currently in use at P&WA, at relative Mach numbers up to 1.5. At higher Mach numbers, these data must be specially input. Various methods of calculating deviation angle are also provided as subroutines.

The program has the capacity to iterate to a solution along several optional paths. The two major paths permit (1) the selection of blade metal geometry that satisfies input vector diagrams and (2) solution of the flow field for arbitrary blading, thus permitting solution of both the "design" and "off-design" problems.

Streamline Calculation Deck

Many variations of this computer procedure are in use for the solution of specific flow problems. The basic procedure, however, permits the calculation of an axisymmetric flow field for a specified flow annulus

containing rotor and stator blade rows. The major difference between this and the AFCC program is that the equations of motion are herein solved, including those terms reflecting the influence of streamline curvature in the meridional plane on the radial static pressure gradient.

Flowpath Description

The flowpath geometry for the single-stage investigation of variable geometry inlet guide vane and stators was designed to resemble the front stage of a state-of-the-art compressor. Axial spacing of the blade rows was slightly increased beyond engine compressor design practice to accommodate instrumentation. The flowpath is shown in figure B-1. The entrance section consists of an outer wall bellmouth and conical inner wall inlet followed by a constant area section to the inlet guide vane leading edge. The inner wall diameter increases from 18.72 in. at the guide vane inlet to a diameter of 25.60 in. at the stator exit. The outer wall converges slightly from a diameter of 43.20 in. at the guide vane trailing edge to a diameter of 42.10 in. at the stator exit. Location of the rig instrumentation stations and the pertinent axial and diametral dimensions are indicated in figure B-1.

The design flowpath model shown in figure B-2 indicates the axial and approximate radial stations at which the blade row design and supporting calculations were performed. The meridional streamlines shown correspond to the final design point meridional streamlines. Streamline analysis calculations were performed at the indicated instrumentation stations and at the leading and trailing edges of each blade row. (The dashed vertical lines at the rotor hub and stator tip leading and trailing edges in figure B-1 are the axial stations that were used to represent the leading and trailing edges of these two blade rows.) The calculated vector diagram data presented graphically in the body of this design report and tabulated in Appendix C refer to the intersections of leading and trailing edge axial stations and design meridional streamline segments that pass through the leading edge of each blade row at 10, 30, 50, 70, and 90% span from the tip (figure B-2). The diameters of these streamline segments at the leading and trailing edges of each blade row are tabulated in table B-1.

Table B-1. Streamline Diameters

Percent Span from Tip at Leading Edge of Blade Row	Streamline Diameters, in.					
	Inlet Guide Vane		Rotor		Stator	
	Leading Edge	Trailing Edge	Leading Edge	Trailing Edge	Leading Edge	Trailing Edge
0	43.28	43.28	43.05	42.67	42.50	42.10
10	40.75	40.75	40.865	40.45	40.669	40.4
30	35.85	36.1	36.495	36.495	37.007	37.0
50	30.95	31.4	32.125	32.75	33.345	35.7
70	26.05	26.8	27.755	29.10	29.68	30.45
90	21.15	22.2	23.385	25.4	26.02	27.1
100	18.70	19.86	21.2	23.65	24.19	25.61

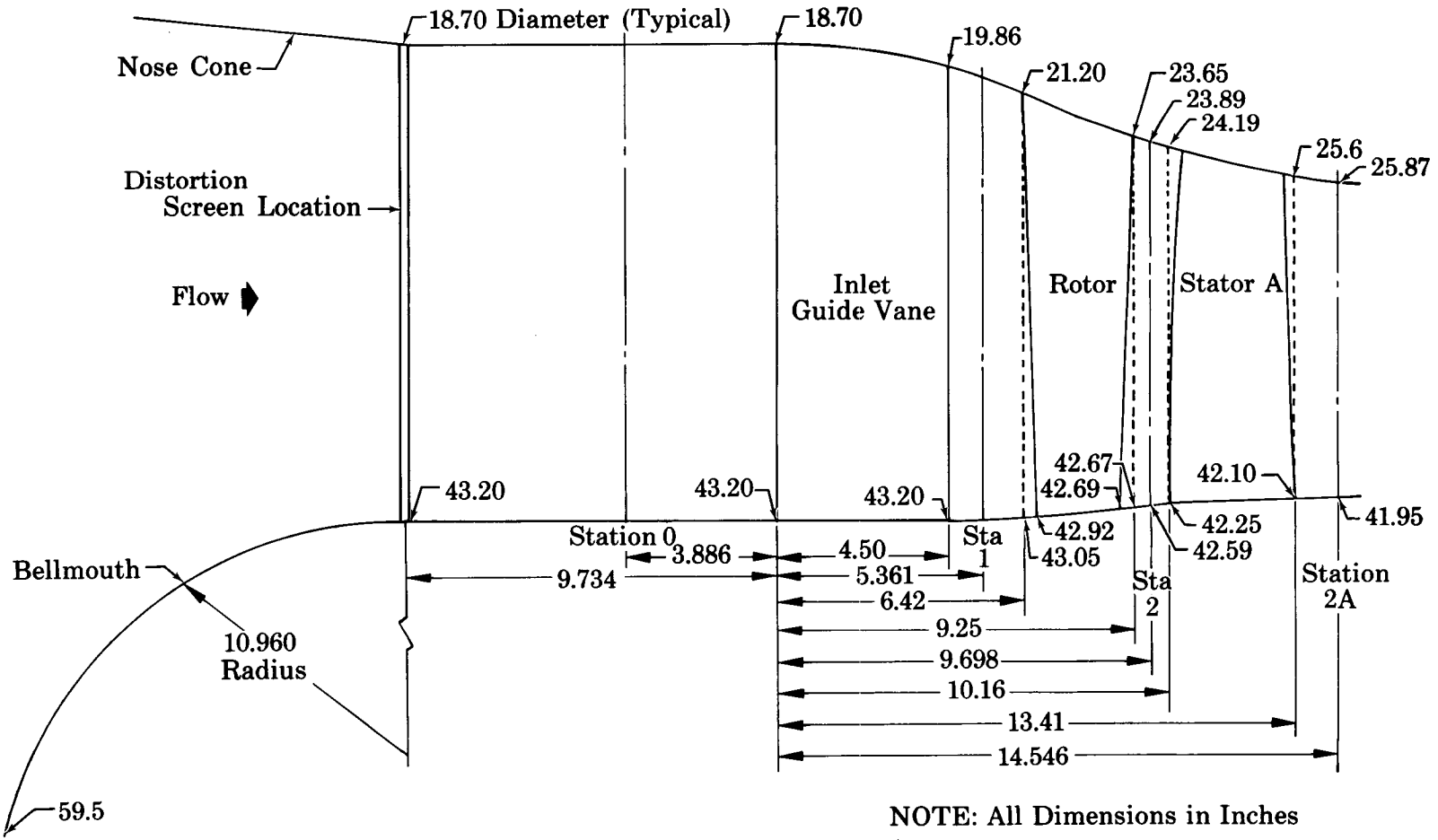

Figure B-1. Flowpath Geometry

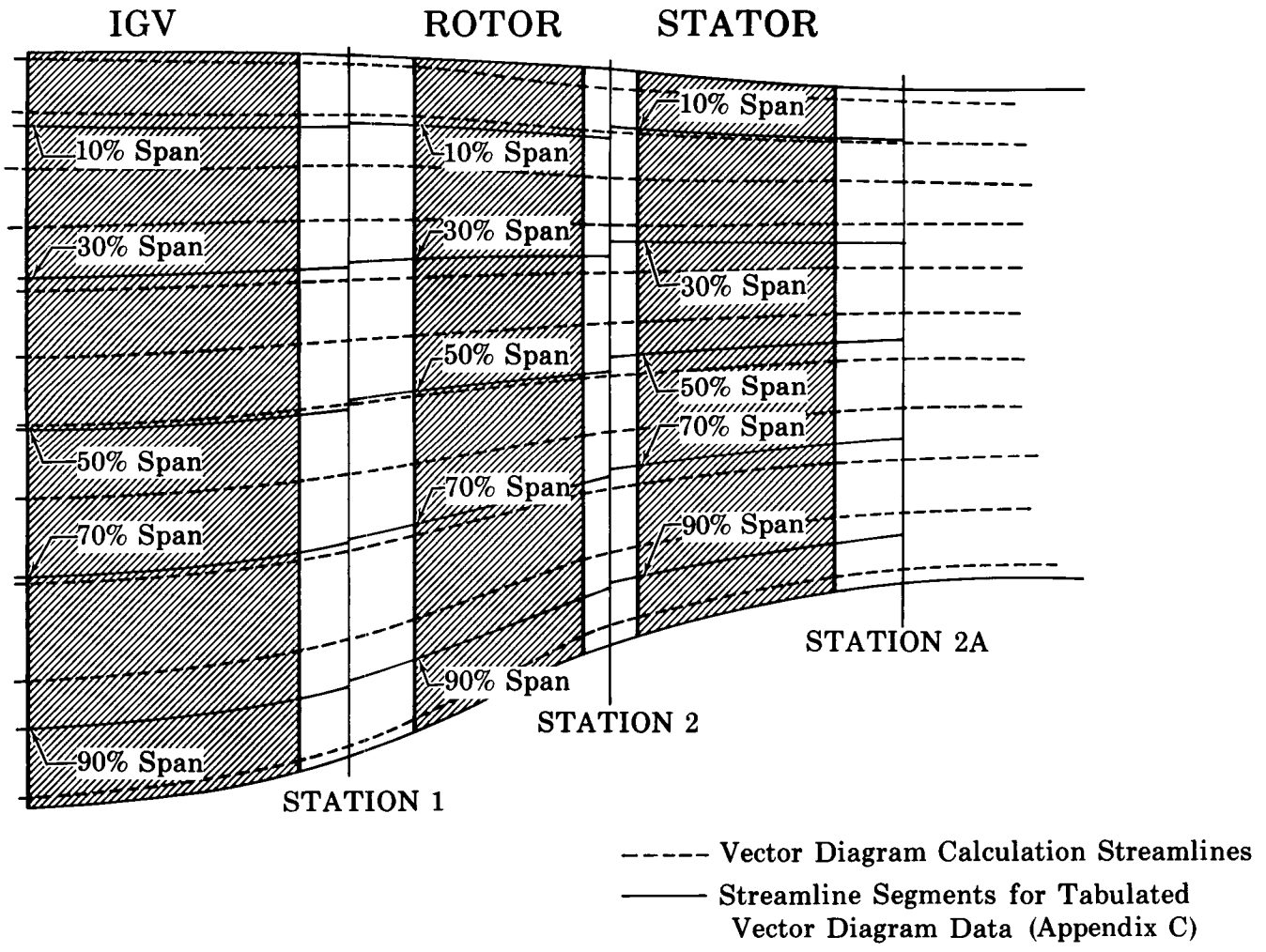

Figure B-2. Flowpath Model for Vector Diagram Analysis

APPENDIX C
TABULATED VECTOR DIAGRAM AND BLADE GEOMETRY DATA

Calculated vector diagram data for design point and off-design velocity triangles are presented in tables C-1, C-2, and C-3. The velocity triangles are in planes that contain the meridional velocity vector, V_m (figure C-1). The reference axial and radial locations for the tabulated vector diagram data are, respectively, the blade row leading and trailing edges and meridional streamline segments that pass through the blade row leading edges at 10, 30, 50, 70, and 90% span from the tip.

Blade element geometry and performance data are presented in tables C-4, C-5, and C-6. Leading and trailing edge metal angles are referred to two-dimensional cascade convention. Camber, incidence, and deviation angles correspond to the meridional streamline segments described above.

Calculated overall performance data are presented in table C-7.

Table C-1. Inlet Guide Vane Vector Diagram Data

Design Point

Percent Span from Tip at Leading Edge	V_{1e}	β_{mle}	V_{te}	V_{mte}	$V_{\theta te}$	β_{mte}	M_{1e}	$\Delta\beta$	ϵ_{te}
90	441.0	0.0	475.1	475.1	0.0	0.0	0.400	0.0	12.1
70	460.0	0.0	496.3	496.3	0.0	0.0	0.419	0.0	7.9
50	473.1	0.0	509.2	509.2	0.0	0.0	0.432	0.0	4.2
30	477.6	0.0	514.2	514.2	0.0	0.0	0.435	0.0	1.1
10	477.0	0.0	512.1	512.1	0.0	0.0	0.434	0.0	-1.4
Off-Design									
90	218.9	0.0	293.9	243.8	164.1	33.8	0.199	-33.8	12.1
70	230.9	0.0	288.1	246.9	148.6	31.1	0.208	-31.1	8.1
50	238.3	0.0	283.8	250.4	134.0	28.2	0.215	-28.2	4.8
30	242.3	0.0	279.7	253.5	118.9	25.0	0.218	-25.0	1.8
10	242.4	0.0	274.4	254.3	113.0	21.9	0.218	-21.9	-1.0

Table C-2. Rotor Vector Diagram Data

Percent Span from Tip at Leading Edge	V'_{le}	V_{mle}	$V'_{\theta le}$	β'_{mle}	V'_{te}	V_{mte}	$V'_{\theta te}$	β'_{mte}	U_{le}	U_{te}	M_{le}	$\Delta\beta$	D_f	ϵ_{le}	ϵ_{te}
Design Point															
90	804.9	517.8	617.8	50.0	584.8	531.8	239.5	24.9	617.8	670.5	0.738	25.1	0.427	17.1	16.1
70	908.5	534.4	734.2	53.9	658.2	529.5	396.1	36.8	734.2	769.0	0.832	17.1	0.416	10.4	9.7
50	1009.2	545.5	849.1	57.3	743.8	522.5	531.0	45.9	849.1	865.5	0.929	11.4	0.394	5.1	4.6
30	1107.4	548.0	963.9	60.2	826.0	513.3	648.2	51.9	963.9	964.2	1.019	8.3	0.383	0.8	0.7
10	1208.8	544.0	1080.0	63.2	905.5	497.9	758.9	56.7	1080.0	1071.0	1.110	6.5	0.377	-2.9	-2.9
Off-Design															
90	378.7	260.8	226.2	46.9	316.3	285.9	131.7	25.0	431.2	567.5	0.341	21.9	0.282	17.1	16.9
70	450.9	261.9	368.8	54.8	353.5	282.4	210.0	36.8	513.1	536.4	0.409	18.0	0.343	11.5	11.9
50	531.7	265.0	462.5	60.4	402.7	286.8	284.5	45.0	594.6	604.5	0.482	15.4	0.368	6.5	7.1
30	618.3	267.1	557.3	64.5	465.5	293.2	361.2	50.9	674.8	673.0	0.560	13.6	0.377	2.0	2.5
10	702.5	267.8	649.8	67.8	522.0	295.9	431.8	55.4	752.5	744.5	0.635	12.4	0.403	-2.2	-2.4

Table C-3. Stator Vector Diagram Data

Percent Span from Tip at Leading Edge	V_{1e}	V_{mle}	$V_{\theta 1e}$	β_{mle}	V_{te}	V_{mte}	$V_{\theta te}$	β_{mte}	M_{1e}	$\Delta\beta$	D_f	ϵ_{1e}	ϵ_{te}
Design Point													
90	696.5	559.2	416.2	36.7	593.9	591.9	43.2	4.1	0.620	32.6	0.362	14.6	6.8
70	661.3	551.5	370.0	33.8	571.9	571.0	26.8	2.6	0.587	31.2	0.350	8.5	3.8
50	634.9	541.2	332.5	31.5	561.0	560.5	19.2	1.8	0.561	29.7	0.335	3.7	1.5
30	617.2	530.0	315.5	30.8	559.7	559.7	18.3	1.8	0.542	29.0	0.319	0.1	0.0
10	604.5	516.5	312.7	31.2	565.9	564.9	20.7	2.1	0.528	28.6	0.298	3.4	-1.6
Off-Design													
90	445.5	298.5	330.0	47.7	313.8	274.0	153.1	29.2	0.400	18.5	0.455	15.5	7.5
70	437.4	294.3	324.5	47.8	333.1	295.1	153.0	27.5	0.392	20.3	0.400	10.6	5.4
50	435.0	297.5	318.1	46.9	351.5	314.1	157.3	26.7	0.388	20.2	0.358	9.8	3.2
30	435.1	301.8	314.5	46.2	370.3	331.8	164.1	26.4	0.388	19.8	0.311	1.4	1.0
10	539.5	303.8	317.4	46.2	392.4	351.5	174.1	26.4	0.389	19.8	0.268	-3.2	1.3

Table C-4. Inlet Guide Vane Geometry

Airfoil Series: 63
No. of Vanes: 20
Thickness Ratio: 0.09

Diameter, ID: 18.70 in. (Leading Edge)
Diameter, OD: 43.20 in. (Leading Edge)

Basic Airfoil*

Percent Span (from Tip)	κ_1	κ_2	ϕ	γ^o	c	σ	δ^o
90	-19.9(-20.2)**	23.7(25.0)	43.6(45.2)	14.1(13.5)	4.52	1.412	1.4
70	-20.0(-20.2)	22.5(23.3)	42.5(43.5)	13.2(12.6)	4.52	1.245	2.1
50	-20.2(-20.2)	21.2(21.5)	41.4(41.7)	12.2(12.1)	4.52	1.080	2.8
30	-20.4(-20.2)	19.9(19.9)	40.3(40.1)	11.2(11.5)	4.52	0.913	3.5
10	-20.6(-20.2)	18.6(18.0)	39.2(38.2)	10.2(10.5)	4.52	0.748	4.2
Design Point							
90	-20.2	5.4	NA*	1.2	4.55	1.412	NA*
70	-20.2	3.7	NA	0.5	4.55	1.245	NA
50	-20.2	1.9	NA	-0.2	4.55	1.080	NA
30	-20.2	0.3	NA	-0.9	4.55	0.913	NA
10	-20.2	-1.6	NA	-1.6	4.55	0.748	NA
Off-Design							
90	-20.2	36.0	56.2	21.1	4.47	1.412	2.2
70	-20.2	34.3	54.5	20.5	4.47	1.245	3.2
50	-20.2	32.5	52.7	19.9	4.47	1.080	4.3
30	-20.2	30.9	50.9	19.2	4.47	0.913	5.9
10	-20.2	29.0	49.2	18.5	4.47	0.748	7.1

*See text, Section II on "Variable Geometry Inlet Guide Vane and Stator Blading."
**Numbers in parentheses refer to modified basic airfoil.

Table C-5. Rotor Geometry and Performance

Airfoil Series: Circular Arc
No. of Blades: 34
Diameter, ID: 21.20 in. (Leading Edge)
Diameter, OD: 43.05 in. (Leading Edge)

Design Point

Percent Span (from Tip)	κ_1	κ_2	ϕ	γ^o	c	σ	i_m	δ^o	$\bar{\omega}'$
90	48.6	18.8	29.8	31.2	3.24	1.42	1.4	6.1	0.024
70	52.5	32.5	20.0	41.2	3.43	1.30	1.4	4.3	0.024
50	56.1	42.1	14.0	48.2	3.63	1.20	1.2	3.8	0.033
30	59.6	48.6	11.0	53.6	3.82	1.12	0.4	3.3	0.058
10	63.2	52.9	10.3	57.9	4.01	1.06	0.0	3.8	0.097

Off-Design

90	48.6	18.8	29.8	31.2	3.24	1.42	-1.7	6.2	0.030
70	52.5	32.5	20.0	41.2	3.43	1.30	2.3	4.3	0.018
50	56.1	42.1	14.0	48.2	3.63	1.20	4.3	2.9	0.030
30	59.6	48.6	11.0	53.6	3.82	1.12	4.9	2.3	0.064
10	63.2	52.9	10.3	57.9	4.01	1.06	4.5	2.5	0.125

Table C-6. Stator Geometry and Performance

Airfoil Series: 65
No. of Vanes: 40

Diameter, ID: 24.19 in. (Leading Edge)
Diameter, OD: 42.25 in. (Leading Edge)

Design Point
(Both Stators)

Percent Span (from Tip)	κ_1	κ_2	ϕ	γ^o	c	σ	i_m	δ^o	$\bar{\omega}'$
90	40.9	-8.7	49.6	16.0	2.75	1.28	-4.2	12.8	0.026
70	37.1	-7.5	44.6	14.5	2.88	1.19	-3.3	10.1	0.025
50	34.7	-7.5	42.2	13.5	3.00	1.12	-3.2	9.3	0.026
30	34.0	-8.0	42.0	13.2	3.13	1.07	-3.2	9.8	0.029
10	36.0	-8.9	44.9	13.5	3.27	1.02	-4.8	11.0	0.032
Off-Design (Stator A)									
90	40.9	17.3	-	-	-	1.28	6.8	11.9	0.040*
70	37.1	18.5	-	-	-	1.19	10.7	9.0	0.038
50	34.7	18.5	-	-	-	1.12	12.2	8.2	0.030
30	34.0	18.0	-	-	-	1.07	12.2	8.4	0.024
10	36.0	17.1	-	-	-	1.02	10.2	9.3	0.027
Off-Design (Stator B)									
90	49.9	17.3	-	-	-	1.28	-2.2	11.9	0.040
70	46.1	18.5	-	-	-	1.19	1.7	9.0	0.038
50	43.7	18.5	-	-	-	1.12	3.2	8.2	0.030
30	43.0	18.0	-	-	-	1.07	3.2	8.4	0.024
10	45.0	17.1	-	-	-	1.02	1.2	9.3	0.027

*No loss allowance was made for the effect of high incidence operation on loss coefficient of the single-flap stator.

Table C-7. General Design Performance Data

Design Point

Rotor Pressure Ratio, P_2/P_1	1.351
Stage Pressure Ratio, P_{2A}/P_o	1.321
Rotor Efficiency, η_{ad} - %	92.2
Stage Efficiency, η_{ad} - %	85.1
Corrected Rotor Speed, $N/\sqrt{\theta}$ - rpm	6050.0
Corrected Weight Flow, $W\sqrt{\theta}/\delta$ - lb/sec	265.0
Corrected Specific Weight Flow, $\frac{W\sqrt{\theta}}{\delta A_A}$ - lb/sec-ft^2	32.0

Off-Design

Rotor Pressure Ratio, P_2/P_1	1.137
Stage Pressure Ratio, P_{2A}/P_o	1.132
Rotor Efficiency, η_{ad} - %	93.5
Stage Efficiency, η_{ad} - %	90.2
Corrected Rotor Speed, $N/\sqrt{\theta}$ - rpm	4235.0
Corrected Weight Flow, $W\sqrt{\theta}/\delta$ - lb/sec	143.3
Corrected Specific Weight Flow, $\frac{W\sqrt{\theta}}{\delta A_A}$ - lb/sec-ft^2	17.28

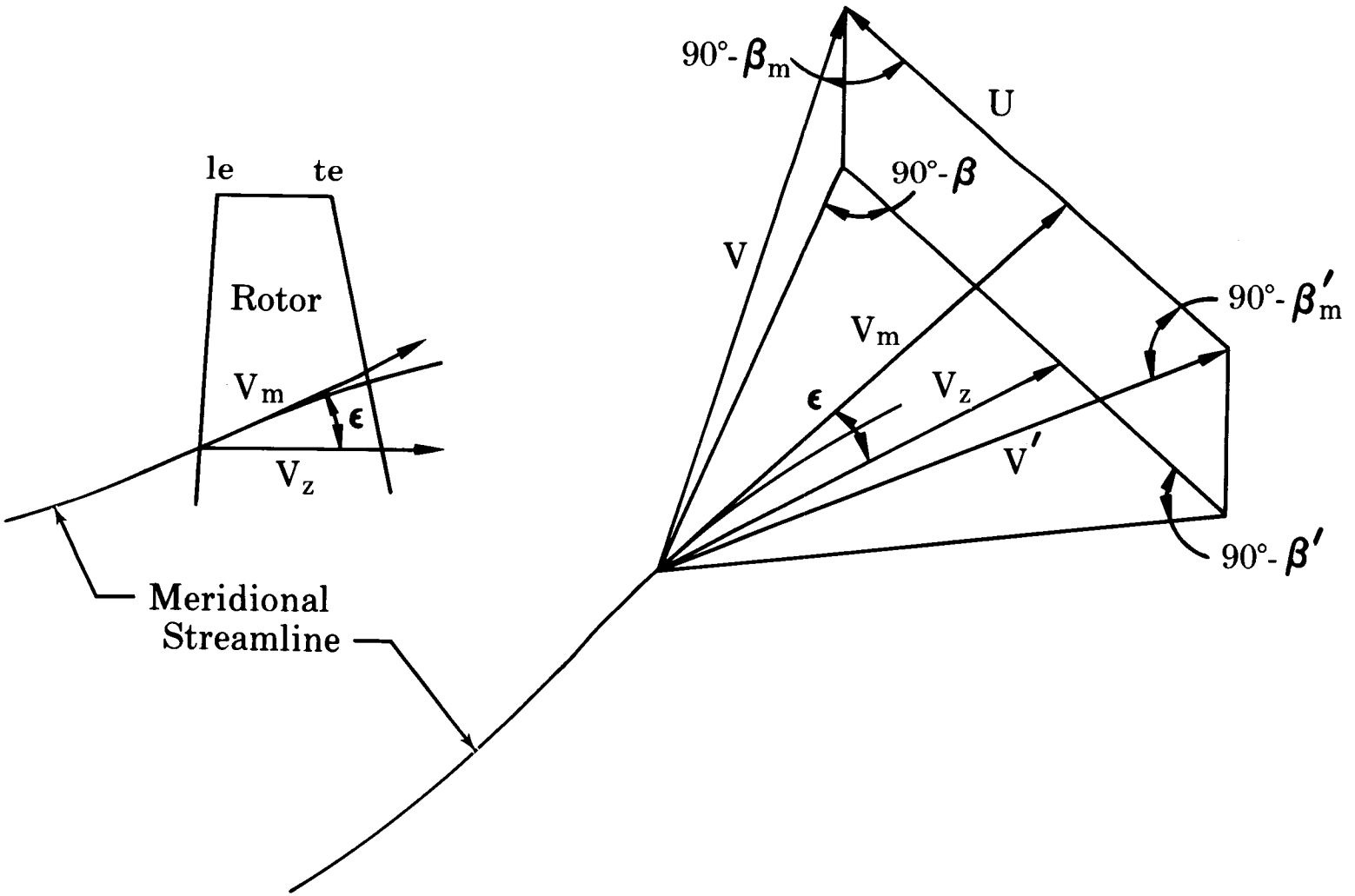

Figure C-1. Description of Velocity Diagram

12. Pratt & Whitney Aircraft
Florida Research and Development Center
P. O. Box 2691
West Palm Beach, Florida 33402
Attention:

W. H. Brown	1
R. A. Schmidtke	1
J. M. Silk	1
B. A. Jones	1
R. W. Rockenbach	1
B. S. Savin	1
W. R. Alley	1
H. D. Stetson	1

13. Pratt & Whitney Aircraft
400 Main Street
East Hartford, Connecticut
Attention:

J. A. Fligg	1
A. W. Stubner	1
W. D. Harshbarger	1
P. Tramm	1
M. J. Keenan	1
B. B. Smyth	1

14. Allison Division, GMC
Department 8894, Plant 8
P. O. Box 894
Indianapolis, Indiana 46206
Attention:

J. N. Barney	1
R. H. Carmody	1
G. E. Holbrook	1
B. A. Hopkins	1
M. L. Miller	1
Library	1

15. Northern Research and Engineering
219 Vassar Street
Cambridge 39, Massachusetts
Attention:

R. A. Novak	1
K. Ginwala	1

16. General Electric Company
Flight Propulsion Division
Cincinnati 15, Ohio
Attention:

J. W. Blanton J-19	1
W. G. Cornell K-49	1
J. R. Erwin J-162	1
E. E. Hood/J. C. Pirtle J-165	1
J. F. Klapproth H-42	1
J. W. McBride H-44	1
L. H. Smith H-50	1
S. N. Suciu H-32	1
J. B. Taylor J-168	1
Technical Information Center N-32	1

17. General Electric Company
1000 Western Avenue
West Lynn, Massachusetts
Attention:

D. P. Edkins - Bldg. 2-40	1
F. F. Ehrich - Bldg. 2-40	1
L. H. King - Bldg. 2-40	1
R. E. Neitzel - Bldg. 2-40	1
Dr. C. W. Smith Library - Bldg. 2-40M	1

18. Curtiss-Wright Corporation
Wright Aeronautical
Woodridge, New Jersey
Attention:

S. Lombardo	1
G. Provenzale	1
J. Wiggins	1

19. Air Research Manufacturing Company
402 South 36th Street
Phoenix, Arizona 85034
Attention:

Robert O. Bullock	1
John H. Daman	1

20. AiResearch Manufacturing Company
8951 Sepulveda Boulevard
Los Angeles, California 90009
Attention:

Linwood C. Wright	1

NAS3-7604
REPORTS DISTRIBUTION LIST

1. NASA-Lewis Research Center
21000 Brookpark Road
Cleveland, Ohio 44135
Attention:

Report Control Office	MS 5-5	1
Technical Utilization Office	MS 3-19	1
Library	MS 60-3	2
Fluid Systems Component Division	MS 5-3	1
Pump & Compressor Branch	MS 5-9	6
A. Ginsburg	MS 5-3	1
M. J. Hartmann	MS 5-9	1
W. A. Benser	MS 5-9	1
D. M. Sandercock	MS 5-9	1
L. J. Herrig	MS 5-9	1
T. F. Gelder	MS 5-9	1
C. L. Ball	MS 5-9	1
L. Reid	MS 5-9	1
J. H. De Ford	MS 60-5	2
C. L. Meyer	MS 60-6	1
J. H. Povolny	MS 60-6	1
A. W. Goldstein	MS 7-1	1
J. J. Kramer	MS 7-1	1
W. L. Beede	MS 60-6	6
J. J. Watt	MS 60-6	1
C. H. Voit	MS 5-3	1

2. NASA Scientific and Technical Information Facility
P. O. Box 33
College Park, Maryland 20740
Attention:
NASA Representative 6

3. FAA Headquarters
800 Independence Ave., S. W.
Washington, D. C. 20553
Attention:
Brig. General J. C. Maxwell 1
F. B. Howard 1

4. NASA Headquarters
Washington, D. C. 20546
Attention:
N. F. Rekos (RAP) 1

5. U. S. Army Aviation Material Laboratory
   Fort Eustis , Virginia
   Attention:
   John White 1

6. Headquarters
   Wright Patterson AFB, Ohio 45433
   Attention:
   J. L. Wilkins, SESOS 1
   S. Kobelak, APTP 1
   R. P. Carmichael, SESSP 1

7. Department of Navy
   Bureau of Weapons
   Washington, D. C. 20525
   Attention:
   Robert Brown, RAPP14 1

8. Department of Navy
   Bureau of Ships
   Washington, D. C. 20360
   Attention:
   G. L. Graves 1

9. NASA-Langley Research Center
   Technical Library
   Hampton, Virginia 23365
   Attention:
   Mark R. Nichols 1
   John V. Becker 1

10. The Boeing Company
    Commercial Airplane Division
    P. O. Box 3991
    Seattle, Washington 98124
    Attention:
    G. J. Schott MS 80-66 1

11. Douglas Aircraft Company
    3855 Lakewood Boulevard
    Long Beach, California 90801
    Attention:
    J. E. Merriman 1
    Technical Information Center C1-250

21. Avco Corporation
Lycoming Division
550 South Main Street
Stratford, Connecticut
Attention:
Clause W. Bolton — 1

22. Continental Aviation & Engineering Corp.
12700 Kercheval
Detroit, Michigan 48215
Attention:
Eli H. Benstein — 1
Howard C. Walch — 1

23. Solar
San Diego, California 92112
Attention:
P. A. Pitt — 1
Mrs. L. Walper — 1

24. Goodyear Atomic Corporation
Box 628
Piketon, Ohio
Attention:
C. O. Langebrake — 2

25. Iowa State University of Science and Technology
Ames, Iowa 50010
Attention:
Professor George K. Serovy — 1
Department of Mechanical Engineering

26. Hamilton Standard Division of
United Aircraft Corporation
Windsor Locks, Connecticut
Attention:
Mr. Carl Rohrbach — 1
Head of Aerodynamics and Hydrodynamics

27. J. Richard Joy
Supervisor, Analytical Section
Williams Research Corporation
P. O. Box 95
Walled Lake, Michigan — 1

28. Raymond S. Poppe
Building 541, Dept. 80-91
Lockheed Missile and Space Company
P. O. Box 879
Mountain View, California 94040 — 1

29. Elliott Company
Jeannette, Pennsylvania 15644
Attention:
J. Rodger Shields
Director-Engineering — 1

30. Chrysler Corporation
Research Office - Dept. 9000
P. O. Box 1118
Detroit, Michigan 48231
Attention:
James Furlong — 1